KU LEUVEN

FACULTEIT INDUSTRIËLE INGENIEURSWETENSCHAPPEN

CAMPUS DE NAYER SINT-KATELIJNE-WAVER

Iris mechanism with heat exchanger

Design, manufacturing, numerical and experimental analysis of a heat exchanger coupled iris mechanism

Pieter Peeraer[1]

Tom Sluyts[2]

Promotor: Prof. dr. ir. D. Moens
Co-Promotor: Prof. dr. ir. N. Ozalp
Ing. C. Ophoff

Masterproef ingediend tot het behalen van de graad van master of Science in de industriële wetenschappen: Elektromechanica:

Automotive[1]
Energy[2]

Academiejaar 2017-2018

Preface

The energy supply of modern day industry, transportation and residential sectors mainly rely on combustion of fossil fuels. However, fossil fuel combustion is responsible for environmentally hazardous emissions and they are not sustainable. Therefore, an alternative energy source that can diverse fossil fuel use with the eventual goal of completely replacing them is needed for clean and sustainable energy future. Renewable energy sources have great potential to serve for this purpose with the solar energy being the most promising. However, despite of the advantages of solar energy, the transient nature of solar energy makes it a challenge to maintain semi-constant temperatures during energy conversion processes that can run on solar energy driven endothermic heat. As new generation engineers, we are excited to take this challenge and find a solution to tackle the transient energy supply of the sun by designing an innovative machinery that can adopt itself to the fluctuations of the solar flux. We are privileged to have the opportunity to work on this subject in the STTL-group and hope to make a difference in this promising and pioneering field.

We would like to thank a few people who supported us during our master's thesis. First, we are very grateful to our promotors Prof. Nesrin Ozalp and Prof. David Moens who gave us the opportunity to work on this field in the STTL research group. We also would like to thank them for their constructive feedback and supervision. With the help of our promotors, we have learned a lot on technical level and project organizational standpoint of view while we had full experience in sharpening our independent problem solution skills.

Secondly, we would like to thank Mr. Cédric Ophoff for his supervision, feedback, advice and continuous follow-up on our thesis. His knowledge in this field really contributed to the successful completion of this thesis.

We would also like to express a lot of gratitude for the long and hard work that Mr. Witse Volders who conducted the manufacturing of the mechanism and for providing us with technical advice during the design evolution to make it manufacturable.

We would like to thank the members of the Solar Thermal Technology Laboratory (STTL) for sharing their knowledge and allow us to take place in their laboratory and use their equipment. We thank them for the experience to work in an international collaboration and the dynamic spirit.

Finally, we would like to give our thanks to our families who supported us during the whole period of studying and more specifically to help finishing this thesis.

We feel privileged to work on this field and hope you will enjoy reading this thesis!

Brief Summary (NL)

De fluctuaties in de hoeveelheid zonne-energie maakt het een uitdaging om een constante temperatuur te verkrijgen in een zonnereactor. Een oplossing hiervoor is een mechanische variabele opening, gebaseerd op het menselijke oog. Zo'n variabele opening heeft als grootste nadeel dat een deel van de flux wordt geblokkeerd door de bladen van het mechanisme. Deze geblokkeerde energie zorgt voor een energieverlies dat wordt omgezet in een temperatuurstijging van de blades van het mechanisme. Het doel van deze thesis is om een variabele opening te ontwerpen, die de geblokkeerde hoeveelheid energie terug kan omzetten in een bruikbare vorm van energie.

Eerst werd een studie uitgevoerd naar alle relevante voorafgaande mechanismen met variabele opening en naar verschillende manieren waarmee de geblokkeerde energie kan teruggewonnen worden. Aan de hand van deze kennis en de specifieke ontwerpvereisten werd een volledig nieuw ontwerp gecreëerd in een CAD-software. Dit nieuwe ontwerp werd met een eindig-elementenpakket geoptimaliseerd op thermo- en vloeistofdynamisch vlak. Het ontwerp van de bladen inclusief de interne waterkoeling maakt dat dit mechanisme een innovatief en technische hoogstaand ontwerp is. Algebraïsche en geometrische analyses werden uitgevoerd om de inwerkende krachten te identificeren en om een correlatie te vinden tussen de rotatie van de stappenmotor en enerzijds de oppervlakte van de variabele opening en anderzijds de hoeveelheid geblokkeerde energie.

Nadat het mechanisme was vervaardigd en geassembleerd, werd het getest op de variabele opening, lekdichtheid en de hoeveelheid energie dat het mechanisme recupereert. De experimentele waarden werden vergeleken met de theoretisch berekende waarden. Aan het einde van deze thesis werd een conclusie geformuleerd over de resultaten en het afgelegde traject.

Abstract

Design, manufacturing, numerical and experimental analysis of a heat exchanger coupled iris mechanism

One of the biggest challenges of the Millennial engineers is to develop new technologies to reduce emission of greenhouse gasses. Given the fact that fossil fuels combustion is the main source of greenhouse emissions, an alternative energy source is needed for industrial processes, manufacturing, and residential use. Such alternative source also must be sustainable so that the pending shortage of fossil fuels would not be a major threat to industry. For example, solar energy would be a sustainable alternative. Power generation via use of solar energy is a mature technology especially by photovoltaic panels. Similarly, power can be generated via solar thermally as well, which is an equally mature technology. However, in order to go beyond power generation, solar thermochemical process technology is emerging with many opportunities to produce fuels and commodities just like fossil fuel driven technologies. Solar thermochemical technology is applicable to high temperature endothermic processes such as methane cracking, water splitting, production of limestone etc. Reaching such high temperatures with solar radiation is achieved via concentrating the incident sun rays. However, the major drawback, or as we like to call it 'challenge', involved with this technology is that the thermochemical processes needs to be housed at a constant reactor temperature. The transient nature of the sun possess difficulty in maintaining constant temperature. Therefore, an innovative solution must be invented to make utmost use of available solar energy.

There have been several design concepts which have experimentally demonstrated the performance of variable aperture mechanism in regulating solar energy entry into solar reactor as an effective solution. Variable aperture mechanism reduces the solar flux entry area when the solar irradiance increases to reduce losses via irradiation. Although this helps in maintaining the temperature, it blocks the available energy. Therefore, a new idea needs to be developed to capture that spilled energy. The mechanism described in this thesis targets solving this problem.

During this thesis we developed a variable aperture mechanism coupled with blades embedded heat exchanger to capture excess heat while maintaining semi-constant temperatures inside the solar reactor. This new design with the heat exchanger coupled blades can not only recover the lost energy but it can also enhance blades lifetime. The optimum geometry of the blades were developed via CFD models where we iteratively improved the design.

Keywords: Iris mechanism, Solar reactor, Variable aperture, Heat exchanger, Design

Abstract (NL)

Ontwerpen, produceren, numerieke en experimentele analyse van een iris mechanisme met een gekoppelde warmtewisselaar

Eén van de grootste uitdagingen voor ingenieurs is het ontwerpen van nieuwe technologieën om het aandeel aan broeikasgassen te verminderen. Wetende dat de verbranding van fossiele brandstoffen de voornaamste bron is van deze broeikasgassen, is er nood aan een alternatieve energiebron voor industriële processen, fabricage en residentieel gebruik. Zo'n alternatieve bron van energie moet ook duurzaam zijn zodat het huidige tekort aan fossiele brandstoffen geen gevaar betekent voor de industrie. Zonne-energie zou bijvoorbeeld gebruikt kunnen worden als duurzame energiebron. Energieopwekking via het gebruik van zonne-energie is een welgekende technologie en dan voornamelijk door het gebruik van fotovoltaïsche panelen. Op een gelijkaardige manier kan ook energie opgewekt worden op een thermische wijze met behulp van de zon. Zonne-energie kan echter verder gaan dan de rechtstreekse energieopwekking. Zonne-thermochemische procestechnologieën bevat namelijk de mogelijkheid om brandstoffen en grondstoffen te produceren. Deze technologie kan gebruikt worden bij endothermische processen die een hoge temperatuur vereisen zoals het kraken van methaan, splitsen van water, productie van kalksteen, …. Zo'n hoge temperaturen kunnen bereikt worden door het concentreren van invallende zonnestralen. Het grote nadeel, of zoals wij het liever noemen 'uitdaging', dat hiermee gepaard gaat is dat de thermochemische processen moeten plaatsvinden bij een constante reactor temperatuur. De fluctuaties in de hoeveelheid zonne-energie maken het echter moeilijk om deze constante temperatuur te onderhouden. Daarom dient er een innovatieve oplossing uitgevonden worden om zoveel mogelijk van de beschikbare zonne-energie gebruik te maken.

Er bestaan reeds een aantal designs die experimenteel hebben aangetoond dat het gebruik van een mechanisme met een variabele opening om de hoeveelheid zonne-energie die de reactor binnentreedt te regelen een effectieve oplossing zou kunnen zijn. Zo'n mechanisme reduceert de oppervlakte van de hoeveelheid flux die de reactor zal binnentreden indien de zonnestraling toeneemt. Ook al helpt dit om een constante temperatuur in de reactor te behouden, het mechanisme blokkeert ook veel beschikbare energie. Daarom is er nood aan een nieuw idee om deze verspilde energie terug op te vangen. Het mechanisme dat wordt beschreven in deze thesis zal dit probleem trachten op te lossen.

Gedurende dit eindwerk hebben wij een mechanisme met een variabele opening en inclusief een warmtewisselaar binnenin de bladen ontworpen om op deze manier het overschot aan energie op te vangen met als doel een constante temperatuur in de reactor te bekomen. Dit nieuw ontwerp met ingebouwde warmtewisselaar zal niet enkel de geblokkeerde energie recupereren, maar het zal ook de levensduur van de bladen verbeteren. De optimale geometrie van de bladen werden ontwikkeld met behulp van CFD-modellen waarbij op een iteratieve wijze het ontwerp werd geoptimaliseerd.

Sleutelwoorden: Iris mechanisme, zonnereactor; variabele opening, warmtewisselaar

Table of contents

Symbol list

a	Distance between origin point *A* and the center of the reactor	[mm]
b	Roller width of a chain	[mm]
c	Number of times a certain event occurs	-
d	Diameter	[mm]
e	Distance between the center of the sprockets	[mm]
f	Darcy friction factor	-
f_{out}	Probability distribution function	-
g	Depth	[mm]
h	Convection heat transfer coefficient	[W/m²K]
i	Gear ratio	-
k	Thermal conductivity	[W/m.K]
l	Length	[mm]
$\dot{m}$	Mass flow rate	[kg/s]
n	Rotational speed	[RPM]
p	Pitch	[mm]
p_e	Probability that an event occurs	[-]
q	Heat flux	[W/m²]
r_{slot}	Radius slot 3	[mm]
t	Time	[s]
u, v, w	Velocity components in x, y, z direction	[m/s]
x_i	Input variables for a function	-
x, y, z	Coordinates	-
A	Origin point	-
A_{CAD}	Aperture surface based on CAD-measurements	[mm²]
A_{Circle}	Aperture surface based on aperture of a circle	[mm²]
A_{eq}	Aperture surface based on established equation	[mm²]
A_s	Heat transfer surface area	[m²]
C	Volume	[m³]
C_p	Specific heat capacity	[J/kg.K]
D	Reference diameter	[m]
E_t	Total energy	[J]
F	Force	[N]
$I_{in,out}$	Irradiance	[W/m²]

K	Length outer hub	[mm]
L	Characteristic length	[m]
$L_{in,out}$	Radiance	[W/sr.m²]
L_e	Emission function	[W/m²]
M	Moment	[N.m]
N	Number of times a certain mathematical procedure is repeated	-
Nu	Nusselt number	-
P	Pressure	[Pa]
Pr	Prandtl number	-
Q	Heat transfer rate	[W]
R^2	Coefficient of determination	-
Re	Reynolds number	-
S	Smallest margin	[mm]
T	Temperature	[°C]
V	Velocity of water flow	[m/s]
Z	Number of teeth	-
X	Chain links	-
β	Maximum rotation angle of the actuator	[°]
Γ	Reflection coefficient	-
ε	Emissivity	-
θ	Zenith angle	[°]
θ_{motor}	Angle of the motor shaft	[°]
$\theta_{Actuator}$	Angle of the actuator	[°]
v	Kinematic viscosity	[Pa.s]
μ_s	Static coefficient of friction	-
ρ	Density	[kg/m³]
σ	Stefan Boltzmann constant = $5.6703*10^{-8}$	[W/m².K⁴]
τ	Stress	[Pa]
τ_p	Pitch angle	[°]
ϕ	Azimuth angle	[°]
φ, ψ, ω, θ	Auxiliary variables for angles in the force analysis	[°]
$\vec{\omega}_{in}$	Vector representing incoming light	-
$\vec{\omega}_{out}$	Vector representing reflected light	-

List of abbreviations

TOE	Tonne of oil equivalent
STTL	Solar Thermal Technology Laboratory
DNI	Direct Normal Irradiance
CFD	Computational Fluid Dynamics
BRDF	Bidirectional reflectance distribution function
PDF	Probability Density Function
BRDF	Bidirectional Reflectance Distribution Function
EDM	Electrical Discharge Machining

List of figures

List of tables

1 INTRODUCTION

Present industry heavily relies on combustion of fossil fuels for power generation, manufacturing, transportation and residential use. During these combustion processes, large amount of CO_2 is emitted into the atmosphere, which is a fundamental cause of the greenhouse effect. Solar energy offers an alternative to fossil fuel combustion because it can provide high temperature process heat just like combustion processes. Contrary to combustion processes, solar thermal processes have significantly reduced emission footprint compared to fossil fuel combustion processes. Furthermore, solar energy is sustainable whereas fossil fuels have limited resources. As seen in Figure 1-1, the energy consumption will increase significantly over next decades. Since fossil fuels are exhaustible, a new technology that is dependent on sustainable sources needs to be developed in order to cope with the increasing energy demand. Solar thermochemical processes would be a good alternative and is a promising solution to diverse the pending fossil fuels shortage. It is possible to produce power, fuels and commodities via solar thermal technology.

In Figure 1-1, the energy consumption is expressed in billion TOE. 1 Billion TOE is equivalent to the amount of energy released by burning one billion tonnes of crude oil [1].

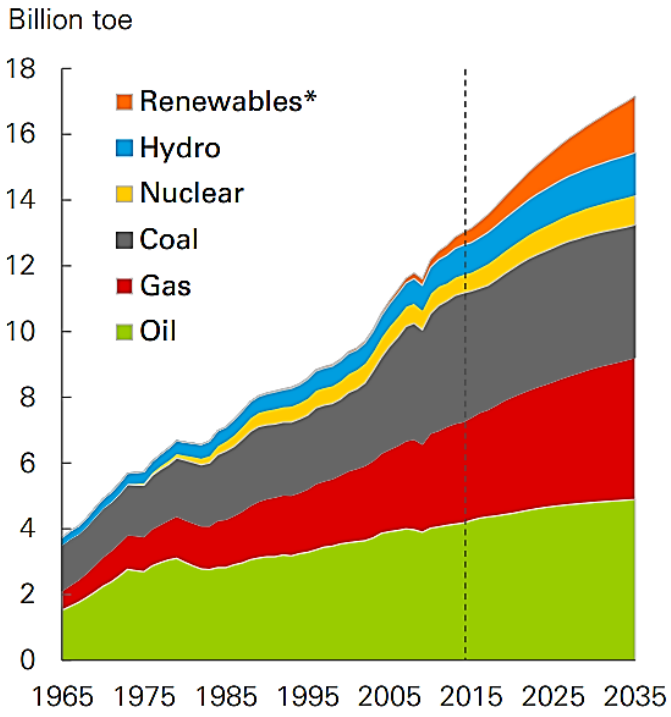

**Renewables includes solar, wind, geothermal, biomass and biofuels*

Figure 1-1 Primary energy consumptions per type [2]

It should be noted that solar thermochemical processes such as solar methane cracking, water splitting, and production of limestone are highly endothermic requiring high temperatures at above 1000 K. To achieve such high temperatures with solar energy, solar radiation must be concentrated. For example, at CNRS-PROMES in France, there is a solar concentrator mirror to focus the incoming solar radiation towards solar reactor where such reactions take place to produce fuels and commodities. Similar experimental setup is also used at the Solar Thermal Technology Laboratory (STTL) in Sint-Katelijne-Waver, but a solar simulator is used instead of the sun as energy source. The solar simulator is at STTL is a Xenoluxe lamp house from

Proyecson which consists of a mirror shaped reflector in the form of a truncated ellipse and a 7 kW Phillips Xenon short arc lamp positioned at the focal point A as seen in Figure 1-2. This solar simulator emits concentrated radiation from the lamp reflected by the ellipsoidal mirror towards focal point B where the aperture of the solar reactor is placed as illustrated in Figure 1-2. The Xenoluxe lamp mimics the radiation derived from the sun and consists wavelengths between 0.3 µm and 3 µm.

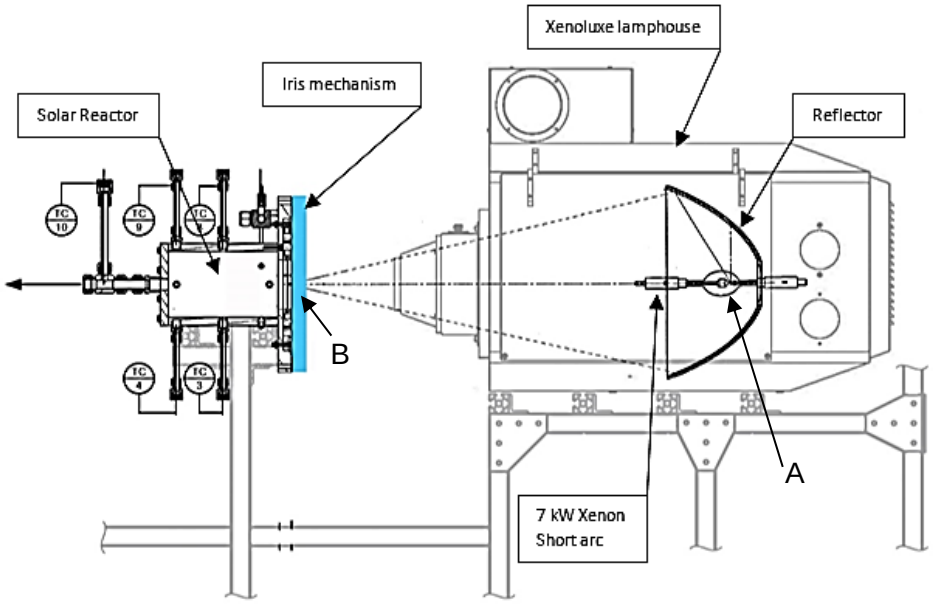

Figure 1-2 Overview of the solar reactor and solar simulator setup at STTL

In spite of resourcefulness and environmentally benign nature, solar energy is transient due to fluctuations from sunrise to sunset and weather conditions. This natural behaviour delivers fluctuating amount of energy which yields unstable temperatures inside any solar energy driven vessel. Therefore, maintenance of semi-constant temperatures inside a solar receiver is a problem that needs technically and economically feasible solution. This thesis focuses on addressing temperature stabilization problem via optimum use of solar energy by capturing the excess heat by a novel design. As demonstrated by Ozalp and Najafabadi (2017), fluctuations in solar radiation can be compensated by either using a variable aperture or by adjusting the gas flow rate. Since the use of a variable aperture is more effective than changing the gas flow rate, this thesis is studying the first option. One of the main issues with variable aperture mechanisms -or iris mechanisms- is that the blades of the aperture are directly exposed to very high temperatures. In this thesis, an iris mechanism is developed to cope with this problem via water cooling the blades where the spilled radiation is captured in water while the blades are cooled. While cooling the blades and capturing the spilled radiation, the mechanism is also capable of maintaining the solar receiver temperature semi-constant by changing the aperture size in accordance to the incoming radiation. This multi-purpose mechanism is a novel approach which provides an opportunity to collect unused solar energy when the iris size shrinks to reduce irradiation losses. In previous iris designs, excess exposure to solar radiation especially when the iris diameter becomes smaller was not addressed. The new approach presented in this thesis involves heat exchanger integration into the iris blades to capture the solar heat via the water as working fluid, which was blocked and absorbed by the blades in other iris mechanisms.

2 LITERATURE STUDY

2.1 Transient nature of solar radiation

The final objective is to use the sun as an energy source for a solar thermal process instead of a solar simulator. Therefore, it is important to know the characteristics of solar radiation. The sun is an inexhaustible source of energy. The disadvantage however is that the flux striking the earth fluctuates. These fluctuations are caused by the changing position of the sun throughout the day, climatological changes and the time of the year. The average amount of radiation throughout the day for every month for a place in Turkey is given in Figure 2-1. To obtain an efficient solar reactor, the temperature in the reactor should be constant. This can only be achieved if the incoming flux is constant. As it is seen in Figure 2-1, the incoming solar flux is not constant. Such fluctuations in incoming solar energy can be compensated by using a variable aperture. The main work principle of variable aperture can be described as follows: when the amount of incoming radiation increases, the aperture area shrinks whereas when the incoming radiation decreases, the aperture area enlargers. This principle creates a balance between the amount of radiation lost and the radiation captured which in return results with semi-constant temperature in the reactor.

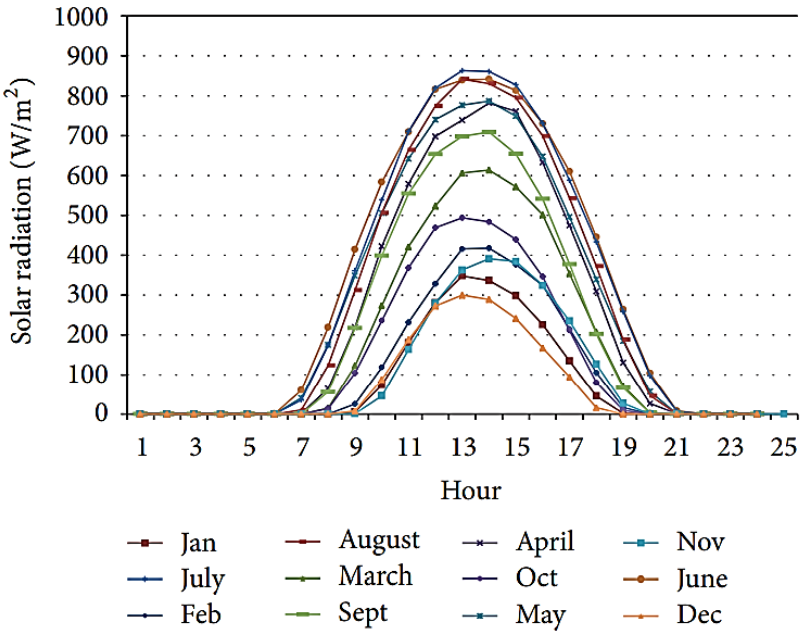

Figure 2-1 Hourly average of solar radiation data for 12 months of the year [3]

The average amount of solar radiation striking the earth on a surface perpendicular to the radiation (DNI = Direct Normal Irradiance) is given in Table 2-1 for six different places. As it is seen, the solar flux is not high enough to provide high temperatures required for thermochemical processes. Even when the flux is at its highest during the day (i.e. noon), it is not sufficient. However, if the solar radiation over a certain surface is concentrated to a much smaller area, then it is possible to reach high temperatures. Concentration ratios can be set per solar thermochemical process temperature requirements. An example high concentration ratio solar energy facility is CNRS-PROMES, where temperatures of up to 3500 K can be achieved [4].

Table 2-1 Average solar DNI for 6 locations [5]

City (Country)	Latitude	Longitude	Average DNI [W/m^2]
Auckland (New Zealand)	36°52' S	174°45' E	435
Birmingham (England)	52°25' N	1°55' W	482
Santiago (Chile)	33° 28' S	70° 45' W	315
New Delhi (India)	28°35' N	77°12' E	333
Los Angeles (USA)	33°56' N	118°24' W	480
Yellowknife (Canada)	62°28' N	114°27' W	621

2.2 Recovery of the lost energy

As aforementioned, variable aperture mechanisms employ blades that are in motion to create various circular opening areas for solar radiation entry. During the course of opening area change, blades are constantly exposed to high flux which keeps the temperature of the blades very high. In particular, once the blades form smaller circular area, they become extremely exposed and possess risk of melt down. Furthermore, continuous exposure to high flux adversely affect the motion mechanism due to disorientation of the metal connections because of thermal expansion and contractions. Lastly, when the solar radiation is at its peak, the variable aperture shrinks the opening area to the smallest circular in order to avoid re-radiation losses. When this occurs, the available flux is lost because of not entering into the reactor. To recover this loss of energy, a heat exchanger can be mounted inside the iris blades. Because of high specific heat capacity, water flowing through the heat exchanger would absorb the excess heat that would be lost otherwise. This would also serve as cooling mechanism for the blades which would eliminate the problems associated with thermal expansion and exposure to high flux. Therefore, especially during the peak times, the high flux absorbed by the variable aperture blades can be used as recovered energy source for relatively lower temperature applications. Below, there are three possible methods discussed as possible ideas to recover the energy loss on aperture blades with their pros and cons.

2.2.1 Thermoelectric generator

A thermoelectric generator is a solid-state device that produces voltage when there is temperature difference between two sides of the device. The temperature difference can only be maintained if the cold side is being cooled down, while the hot side is being heated by the concentrated solar radiation. Since it produces electric power directly, there is no need for a generator. Therefore, the overall construction can be made very compact. The operating temperature of the generator depends on the materials used. In general, there are three kinds of thermoelectric generators: Bismuth telluride alloys, Lead telluride alloys, and Silicon Germanium alloys. Their operating temperatures are 450 K, 1000 K, and 1300 K, respectively [6].

The biggest disadvantage of this technology is that this is a rather unknown technology which requires a lot of research, and it has not yet been commercialized. If the iris mechanism of this thesis is made out of a thermoelectric material that meets the requirements in terms of shape, temperature difference, etc. then it would be very expensive.

2.2.2 Preheat gas

If the heat intercepted by the aperture during peak flux can be captured by the blades, it can be used to preheat feedstock entering the solar reactor. When this method is used, the feedstock flow rate can be higher since the feedstock would take less time to heat up to dissociation temperature inside the reactor. This method is similar to the changing of the gas flow rate. As mentioned above changing the gas flow rate is not as efficient as using an iris mechanism without preheating the gas. With this technique, a constant output flow of fuels or any other reactants can not be obtained.

2.2.3 Steam turbine

If the heat intercepted by the aperture during peak flux can be captured by the water flowing through tubings mounted inside the blades, then this would be an additional good use of spilled solar energy. A major advantage of using water is that it not only recovers the lost energy, but it also cools the blades. Previous designs without a cooling like Ophoff's showed damage at the center because of overheating [7]. With this new design, such problem can be prevented. If this method is used, the blades have to be carved to accommodate internal tubing. The best shape and size of such design are discussed in later sections of this thesis.

It is possible to flow pressurized water through the internal tubings of the iris to achieve steam that is at temperatures higher than 100 degrees Celsius. High temperature-high pressure steam can be used in a steam turbine to produce electricity. Power plants featuring such technology are called 'Rankine Cycle'. The main principle of Rankine Cycle is presented in Figure 2-2. The steps of power generation in Rankine Cycles by using high temperature-high pressure steam in steam turbines are as follows:

1-2: A pump is used to pressurize water.

2-3: The boiler turns pressurized water into steam. In our case, concentrated sunlight would heat up the water flowing through the tubings inside the iris mechanism.

3-4: Pressurized steam enters the turbine and it rotates the generator's shaft to produce electricity.

4-1: A condenser is used to cool the low temperature-low pressure mixture.

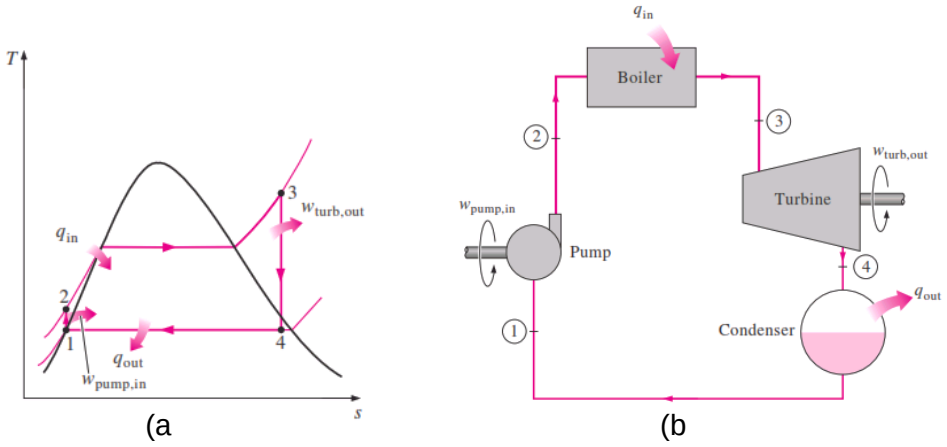

Figure 2-2 Rankine Cycle: (a) T-s diagram, and (b) Overall scheme [8]

The flux from the sun (or the solar simulator) would be transferred into the water by means of three heat transfer mechanisms. First, the heat is transported by radiation from the sun to the front of the iris mechanism (see eq. 2-1). Second, heat is conducted through the material of the

iris mechanism to the inner tubbing (see eq. 2-2). Last, heat is transported from the tubes to the fluid inside these tubes by convection (see eq.2-3) [8].

$$Q_{Cond} = -kA_s \frac{dT}{dx} \quad (2\text{-}1)$$

$$Q_{Conv} = hA_s(T_s - T_{amb}) \quad (2\text{-}2)$$

$$Q_{Emit} = \varepsilon\sigma A_s(T_s^4 - T_{amb}^4) \quad (2\text{-}3)$$

Q	Heat transfer (W)
k	Thermal conductivity (W/m.K)
A_s	Heat transfer surface area (m^2)
dT/dx	Temperature gradient in x-direction (K/m)
h	Convection heat transfer coefficient ($W/m^2.K$)
T_s	Surface temperature (K)
T_{amb}	Ambient temperature (K)
σ	Stefan-Boltzmann constant = 5.6703 x 10^{-8} W/m^2K^4
ε	Emissivity

2.3 Variable aperture mechanisms

As aforementioned, a variable aperture will be used to achieve semi-constant temperatures inside the reactor. There have been a lot of research done on this topic by our research group led by Prof. Ozalp which are summarized in next sections and discussed for potential improvement. The main goal of variable aperture used for a solar reactor should be approximately a circle to capture the available solar energy. The reason for this is that the idealized incident radiation has a circular Gaussian distribution as seen in Figure 2-3.

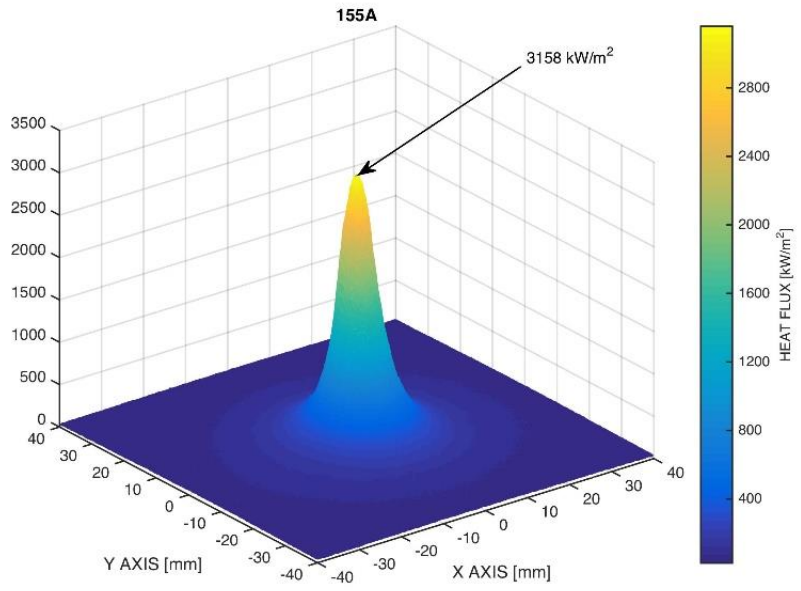

Figure 2-3 Flux map 155 A [9]

Figure 2-3 shows the flux map of the radiation coming from the simulator at its highest power, which corresponds to a current of 155 A. For calculation purposes, it is preferable to have a circular aperture since this simplifies the overall complexity. For example, the amount of solar radiation blocked by the iris blades during closed position can be easily identified by calculating the volume underneath the heat flux map if the aperture has a circular shape. Below, previously designed variable aperture mechanisms are discussed.

2.3.1 Camera-like aperture

Such designs are usually used in photography. Such variable aperture is also called as an iris mechanism. An iris mechanism consists of moving blades which can close or open a circular aperture area. This movement of the blades can be divided in two groups: (1) Blades rotating around an axis perpendicular to its surface and (2) Blades translating in the direction of an axis. How well this aperture approaches to a circle depends on the amount and shape of the blades. Figure 2-4 shows the working principle of an iris mechanism, where the blades rotate while being used in a camera. A stepper motor rotates the outer ring. This rotational motion moves the blades around their pins which results in opening or closing of the aperture.

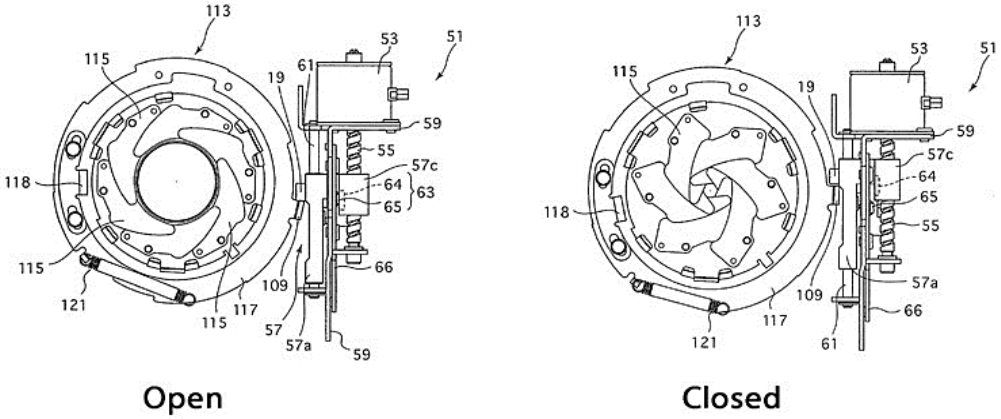

Figure 2-4 Camera-like aperture mechanism [7]

This mechanism is made to operate at room temperature. When used at high temperature environment, the motor should be located farther away from the center, and the blades need to be thicker to withstand these temperatures. In Ref. [10], CFD simulations of solar reactor showing the temperature distribution, and the TracePro simulations are given to show the ray tracing for the solar reactor with camera-like aperture.

2.3.2 Sliding Iris mechanism – Al Hamidi et al.

A rather simple but effective design is a sliding iris mechanism as described in Ref. [11]. It consists of two shutter blades which can translate using a gear and rack. The disadvantage of using only two blades is that the aperture is never as close to a circular shape as other mechanisms with more than two blades. This iris mechanism is therefore only used as a prototype which makes the preliminary calculations simplified. However, by using only two blades, the blades can be made thicker without making the overall mechanism too thick. Since thicker blades are necesarry to place tubings, this design has potential for improvement into heat exchanger embedding iris concept.

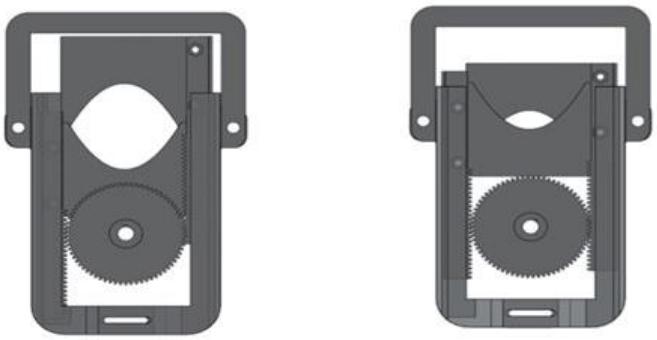

Figure 2-5 Sliding iris mechanism [11]

2.3.3 Translational iris mechanism - Ophoff

Ophoff's design [7] created in 2015 is made of 8 two-edge blades with a raindrop-shaped opening. Since the design features many blades with well-optimized geometry, the mechanism approaches to circular opening. In particular, the opening transforms from a circle to an octagon then to a hexagon, and then back to an octagon. This rather complicated geometry has a drawback that it is hard to control compared to the sliding iris mechanism. A chain drive is used to rotate an actuator. The actuator is provided with slots and the blades with pins. This pin-slot mechanism transfers the rotational movement of the actuator into a translational movement of the blades. This is in contrary to the principle of a camera-like aperture. As seen in Figure 2-6 (b), the blades are very thin. This could lead to damage when the iris mechanism remains closed for a long time during peak flux times due to exposure to high amount of flux. As for the possibility of embedding tubings inside the blades of this mechanism, because the thickness is already large, it would make the overall thickness larger. Therefore, this iris mechanism is not preferable candidate to implement heat exchanger on the blades.

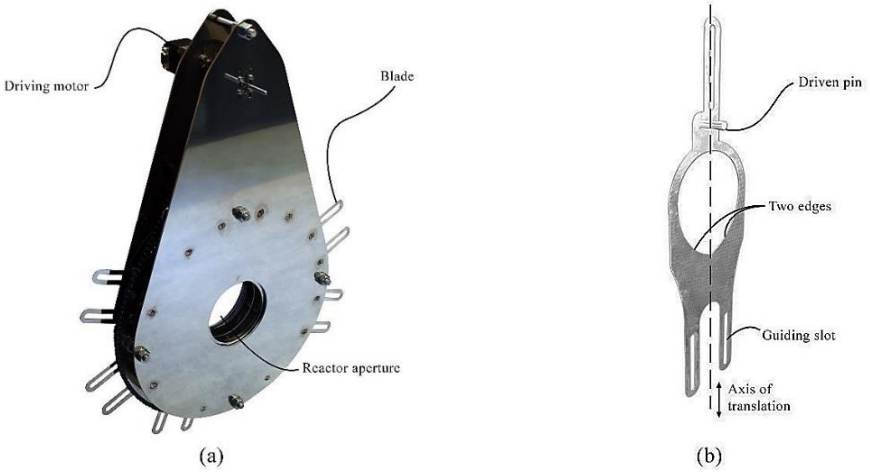

Figure 2-6 (a) The overview of the translational iris mechanism, and (b) The geometry of a single blade [5]

2.3.4 Flower mechanism - Bogaerts

Bogaerts' design [12] made in 2016 is based on the flower Iris Latifolia. A total of 4 small DC-servomotors are used to rotate 4 blades. What makes this design so unique is motion of the blades, geometry of the blades, and minimal lost space for reflections. This mechanism was the first step towards implementation of water channels inside the blades. However, although the

aperture approaches a circular shape, it is not as precise as Ophoff's design and has more complex parts to initiate motion.

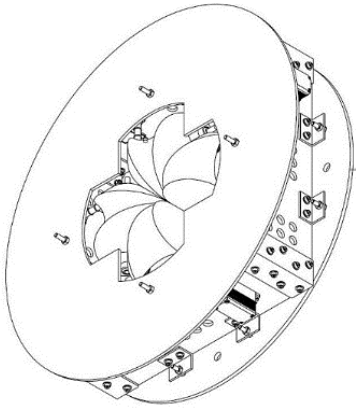

Figure 2-7 Flower mechanism [12]

2.3.5 PEDOT based variable aperture

PEDOT (poly 3.4 ethylene-dioxythiophene) is an Electrochromic (EC) material. These kinds of materials are capable of changing their absorption and transmission characteristics when a small voltage is applied [13,14]. What makes this material so special is the fact that it is possible to make any laterally structured aperture. It is sufficient to apply a certain electrical potential for short period of time. This results in a low-energy variable aperture. However, the melting point of PEDOT is between 98 °C and 100 °C [14]. Above these temperatures, it will loses conductivity and therefore also its capability to vary its aperture. In Figure 2-8, the current density and amount of light going through the aperture is plotted in function of the voltage applied. As shown in Figure 2-8, the characteristics can be changed slightly by using other layers like d-sorbitol.

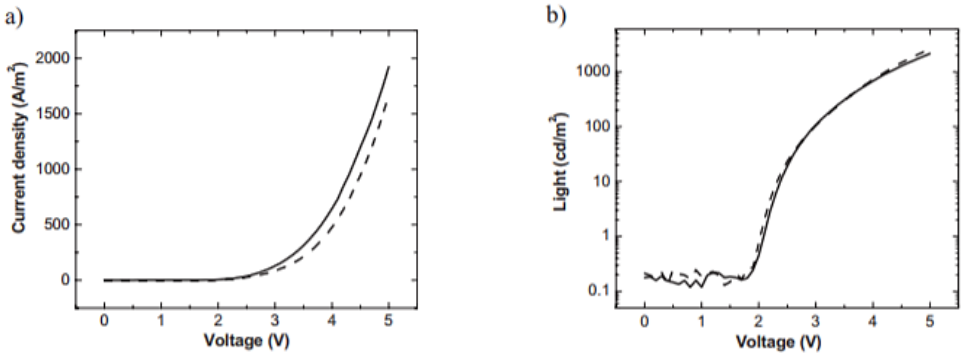

.

Figure 2-8 (a) Current-Voltage, and (b) Light-Voltage curves of glass/ITO/PEDOT:PSS/MEH-PPV/CA/Al (solid line), and glass/ITO/PEDOT:PSS/d-sobitol /MEH-PPV/CA/Al (dashed line) [14]

2.3.6 Other uses for iris mechanisms

2.3.6.1 Valves

Iris valves are designed to handle gasses, fluids or dry bulk solids. They can control the flow rate very precisely. Although the temperature range of the materials is limited, there are a lot of applications of iris valves in the industry. Below is the discussion on two types of iris valves.

An iris mechanism for dry bulk solids can be seen in Figure 2-9 (a). This mechanism is designed for free-flowing materials in gravity discharge. The mechanism includes a flexible cylindrical sleeve strained on to a control ring and a cylindrical clamp. Rotation of the control ring twists the

flexible sleeve in an iris pattern and changes the aperture of the valve. Figure 2-9 (b) shows an iris valve for fluids and gasses. The design of this mechanism is similar to the iris mechanism discussed in Section 2.3.1, where the blades rotate around an axis. The main difference between these two mechanisms is the more annular shape of the aperture.

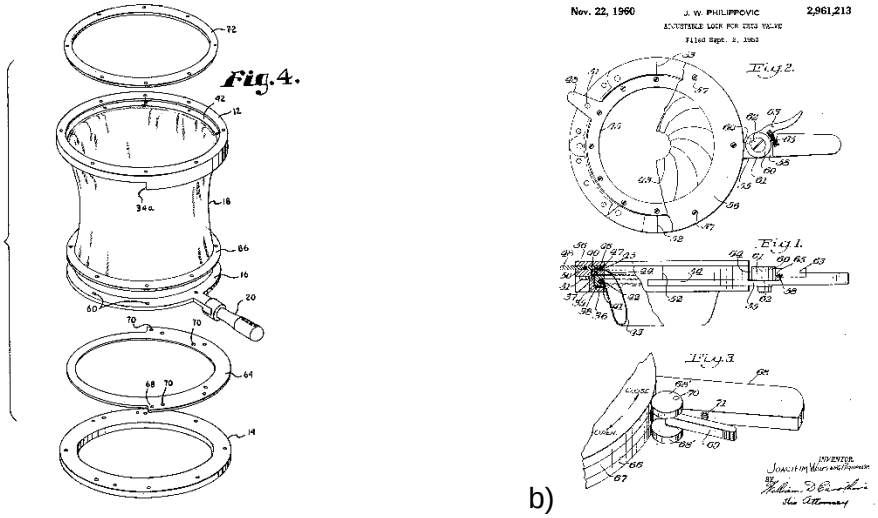

a) b)

Figure 2-9 (a) Iris valve for control of bulk solids US Patent US 7021604 B1 (2006), and (b) Adjustable lock for iris valve US Patent US 2961213 A (1960)

2.3.7 Variable nozzle

A nozzle is a device to control the direction and characteristics of a flow of a gas or fluid. By decreasing the area, output fluid reaches higher velocity. In variable nozzles, the diameter of the outlet can be controlled. The most common application of variable nozzles can be found at the exhausts of jet engines. Type of nozzles used in jet engines can be categorized in two groups. The nozzles that are shaped as iris blades as seen in Figure 2-10 (a), and the nozzles that are shaped per movable flaps as seen in Figure 2-10 (b).

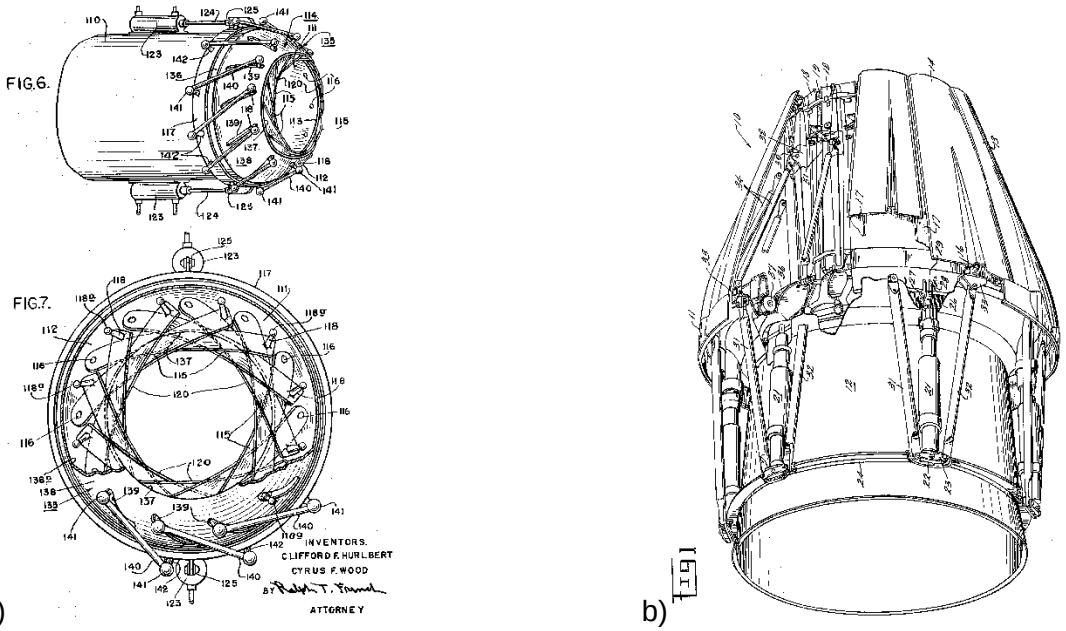

a) b)

Figure 2-10 (a) Variable area propulsion nozzle US Patent US 2934892 A (1960), and (b) Exhaust nozzle flap US Patent US 4128208 A (1978)

The main difference between the previous iris mechanisms and the variable nozzles seen in Figure 2-10 is the position of the blades. All of the iris blades are positioned on the same plane of the aperture. In the variable nozzles, the blades are not positioned on the plane of the aperture but are cone-shaped and their overall thickness is larger.

2.3.8 Timeline

Figure 2-11 gives an overview of relevant iris mechanisms designed in chronological order. Table 2-2, Table 2-3, and Table 2-4 give a comparison of relevant iris mechanisms.

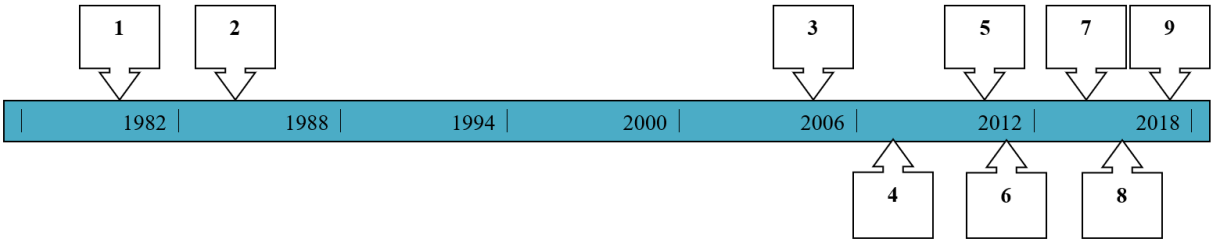

Figure 2-11 Timeline of iris mechanisms developed

Table 2-2 Overview of relevant iris mechanisms

Year	1980	1984	2005
Number	1	2	3
Name	Solar heat aperture control apparatus	Energy beam collimator	Iris light intensity adjusting device
Author	Jubb A.	Ronald A. Hill	Canon K. Kaisha
Motion	Translation	Translation	Rotation
Blades	8	4	6
Shape	Rectangular	Rectangular	Hexagonal
Diameter Range	NA	NA	NA
Thickness	NA	NA	NA
Patent/Reference	US Patent: US 4222367 A	US Patent: US 4450578 A	US Patent: US 6867932 B2
Figure of the concept	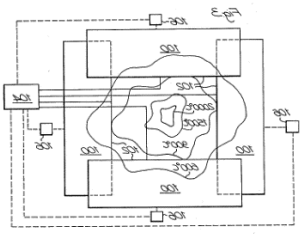	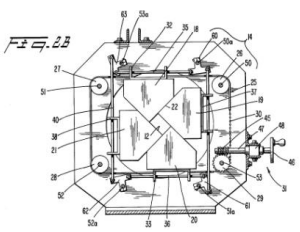	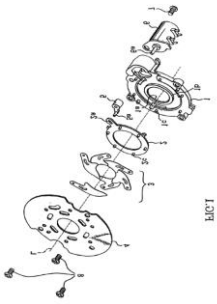

Table 2-3 Overview of relevant iris mechanisms (continued)

Year	2008	2011	2011
Number	4	5	6
Name	Solar energy control	Parabolic shaped iris mechanism	Camera like aperture mechanism
Author	Tuchelt M.	Ozalp N.	Ozalp N.
Motion	Translation	Translation	Rotation
Blades	6	2	8
Shape	Hexagonal	Elliptical	Octagonal
Diameter Range	NA	0-80 mm	NA
Thickness	NA	NA	NA
Patent/Reference	US Patent: US 20080060636 A1	[11]	[15]
Figure of the concept	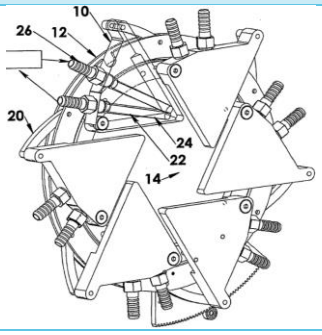	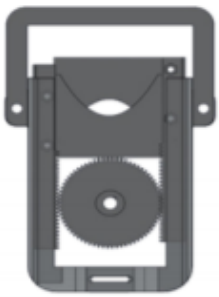	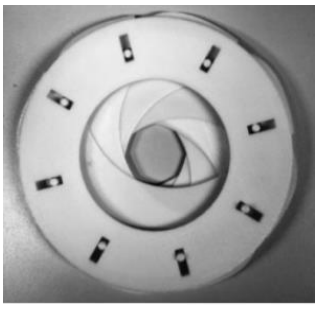

Table 2-4 Overview of relevant iris mechanisms (continued)

Year	2015	2016	2017
Number	7	8	9
Name	Human eye inspired iris mechanism	Flower shaped iris mechanism	Rotary aperture
Author	Ophoff C.	Bogaerts J.	Ozalp N.; Ophoff C.
Motion	Translation	Rotation	Rotation
Blades	8	4	1
Shape	Octagonal	Circular	Circular
Diameter Range	0 – 100 mm	0 – 100mm	20 – 100 mm
Thickness	75 mm	85 mm	3 mm
Patent/Reference	[7]	[12]	[5]
Figure of the concept		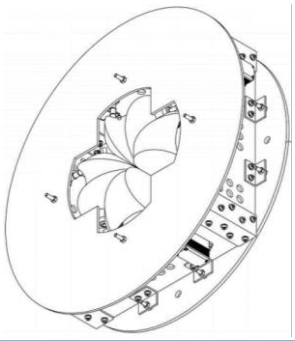	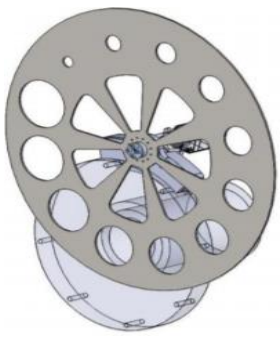

3 METHODOLOGY

This chapter covers the methodology implemented in designing an iris mechanism with heat exchanger. The overall design can be divided into two main sections: (1) Mechanical design, and (2) Thermodynamic design. These two parts are carried out simultaneously in this thesis because of their mutual dependence.

3.1 Design requirements

It is very important to define the design criterion as the first step. Iterative design and optimizations can be done in accordance to this check list by keeping the target goals as the achievement of semi-temperatures and capturing the spilled solar energy while cooling the blades. Below list shows the design criterion for heat exchanger coupled iris mechanism studied in this thesis:

- Cooled blades
- Circular aperture
- Minimum 20 mm opening
- Maximum 120 mm opening
- Minimal overall thickness
- Minimal blade thickness
- High temperature resistant material
- Low economic cost
- Manufacturable
- Mountable on the solar reactor
- Driven by a stepper motor
- Precise control of the aperture surface
- Water sealed blades
- Minimal overall size of the mechanism
- Tubing connections should not interfere each other during motion of the blades
- Tubing connections should not be on the pathway of the light beam
- Blades motion should not be lammed, minimal friction between the moving parts

3.2 Creation of the design

The design of the iris mechanism for this thesis is inspired per previous designs found in literature. For example, transmission-principle of the ‘Translational iris mechanism’ is chosen for the motion where the rotational movement is converted into translation of the blades. Since the blades are connected with tubes, it is preferable to have only one translation. Otherwise, the tubes would interfere with the transmission and/or the force from the tubes acting on the blades would be significantly higher. As for the geometry of the blades, a new concept is developed by meeting the aforementioned design requirements. Relying on previous designed variable aperture mechanism is not possible, because these are either made out of too many blades or the aperture does not approach a circular shape. The main challenge is to create a mechanism with as few

blades as possible while maintaining a circular aperture which is discussed in detail at first part of Chapter 3.3. As for the design of tubings for water flow, technical details are given in Section 3.5 Thermofluidic analysis.

3.3 Mechanical design

In this section, the outer shape of the blades and the transmission is discussed in detail. During this design process, it is important to bear in mind that the blades must withstand a high amount of flux and high temperatures.

3.3.1 Blades

The first step of the design process is the creation of an overall shape for the blades because the blades are the most important parts because they determine the variable aperture of the iris mechanism. Since the incoming solar radiation has a Gaussian distribution as it is seen in Figure 2-3, it is preferable to have a circular aperture geometry as the blades open and close. This way it is easier to control the aperture in function of the intensity of the incoming radiation, to achieve a constant temperature inside the reactor. To meet the requirement of a minimum overall thickness, the number of blades should be limited because every blade is embedded with an internal heat exchanger tubing carved in blade. Given that reason and to minimize the complexity during motion, only four blades are used in this design. As for the blade geometry, past research designs in literature have been inspirational, but the design of the blades described in this thesis is completely new. Based on these, a preliminary design was made which was optimized for improvement and form the final design as shown in Figure 3-1.

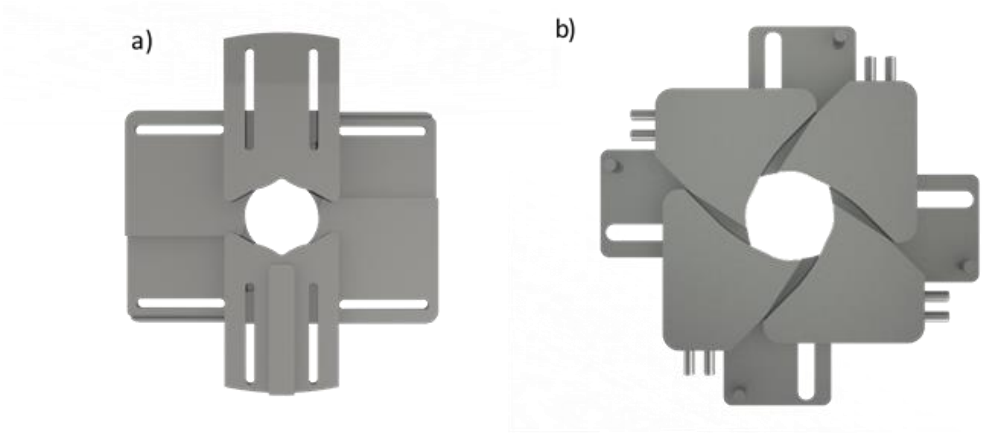

Figure 3-1 (a) Preliminary design (thickness = 40 mm), and (b) Final design (thickness blade = 14.5 mm)

The preliminary design seen in Figure 3-1 (a) has two types of blades: horizontally placed and vertically placed. The horizontally placed blades are shaped in a way to achieve the circular opening at a larger aperture. On the other hand, the vertically placed blades come closer to each other at a small aperture in comparison to the horizontal blades. Therefore, these blades are made to achieve the circular opening at a smaller aperture. The problem with this first design is that with an overall thickness of 40 mm (without any transmission) the requirement of a minimum overall thickness is not achieved.

After thorough optimization, the last design seen in Figure 3-1 (b) is developed which has only one type of blade. The blades in this design can glide over each other limiting the overall blade thickness to 14.5 mm. Figure 3-2 illustrates how the (blue) curve, which determines the aperture shape, is designed. Over 20 different types of curves were considered before achieving this particular shape. Knowing that a perfect circular aperture is not feasible in an iris mechanism and that it is harder to approach a circle as fewer blades are used, it was a challenge to design a curve which results in an acceptable circular shaped aperture at any given aperture. As it is seen in Figure 3-2, the aperture is a perfect circle when using four blades with an aperture that has diameter of 50 mm. For larger apertures, an interpolation between these circles has been done. When modelling this blade in 3D, slight modification has been done (e.g. fillets).

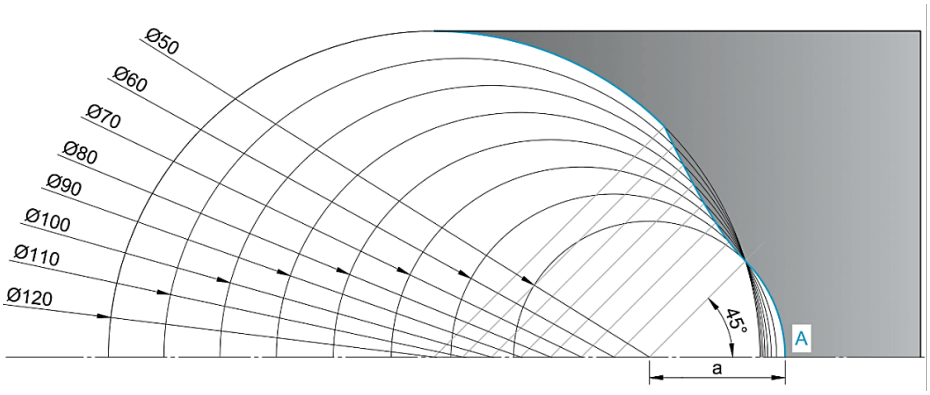

Figure 3-2 Design process curve for optimization

Point *A* in Figure 3-2 is defined the origin point of the blade throughout this thesis and *a* is the distance between the origin point *A* and the center of the solar reactor. This distance changes as a function of the aperture. In Figure 3-2, distance *a* is given for an aperture equivalent to a circular aperture with a diameter of 50 mm.

Throughout the thesis, a certain nomenclature to define pin-slot mechanisms is used. The letter S is always referred to a slot and the letter P referred to a pin. The pin slot mechanism is given a number. For example, in Figure 3-3, P3 refers to the pin of the pin-slot mechanism 3. The corresponding slot S3 is shown in Figure 3-5.

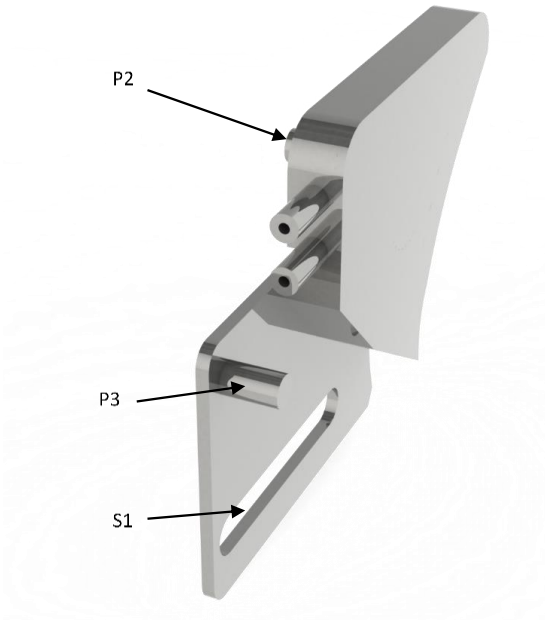

Figure 3-3 Pin-slots mechanisms of the blade

Optimization of the blades

After the completing the force analysis per Figure 3-3 and inspecting the 3D-printed prototype, a new problem is being realized: when applying a force on pin P3, the blades tend to rotate. This rotation can be explained by a small gap between the pin and slot of pin slot mechanisms 1 and 2. Even a small tolerance between the pin and slot causes instability of the blade. The solution to this problem is to add a fourth pin slot mechanism to the blade, which disallows the rotation of the blade. This modification can be seen in Figure 3-4.

When inspecting all of the acting forces on the blade, it can be noticed that the friction force of the pin slot mechanism 3 is preferably kept low. Therefore, a needle roller bearing HK 0608 is placed over pin 3, which results in a friction force of almost 0 N.

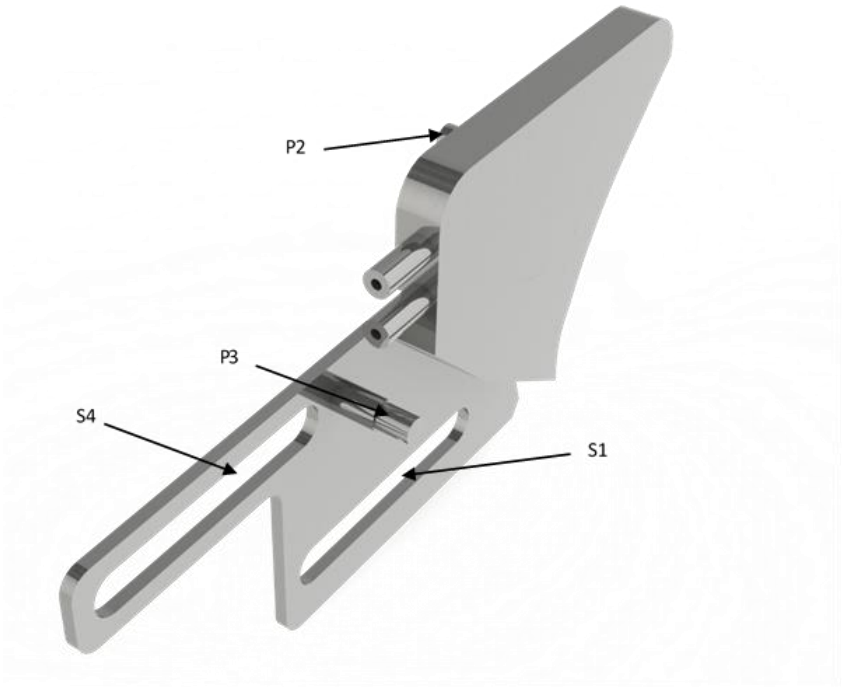

Figure 3-4 Pin slot mechanism modification of the blade

3.3.2 Actuator

To convert rotational movement of a stepper motor into a translation of the blades, an actuator is designed. Figure 3-5 gives the design of the actuator with corresponding slots of S3 and S5. The slots S3 are shaped in a way that if the actuator rotates 6.25°, the radial distance from pin P3 changes by 5 mm. This distance is referred to by r_{slot}. The transmission of the motor to the actuator cannot have slip for accurate positioning of the blades. The transmission also needs to be temperature resistant or needs to be placed far from the focus point of the solar simulator. As a result of these requirements, a chain transmission is chosen over other kinds of transmission, e.g. a belt transmission. A roller chain ISO 05B is available in the lab. Therefore, this chain will be used if it is able of transferring the necessary torque to the actuator. The properties of the chain-connection are calculated in Section 3.3.3.

A flower shaped hole is cut in the actuator as it can be seen in Figure 3-5. This has the advantage of decreasing the overall mass of the iris mechanism. The distance between the blades and the actuator is determined by the selected tubes for the water connected to the blades.

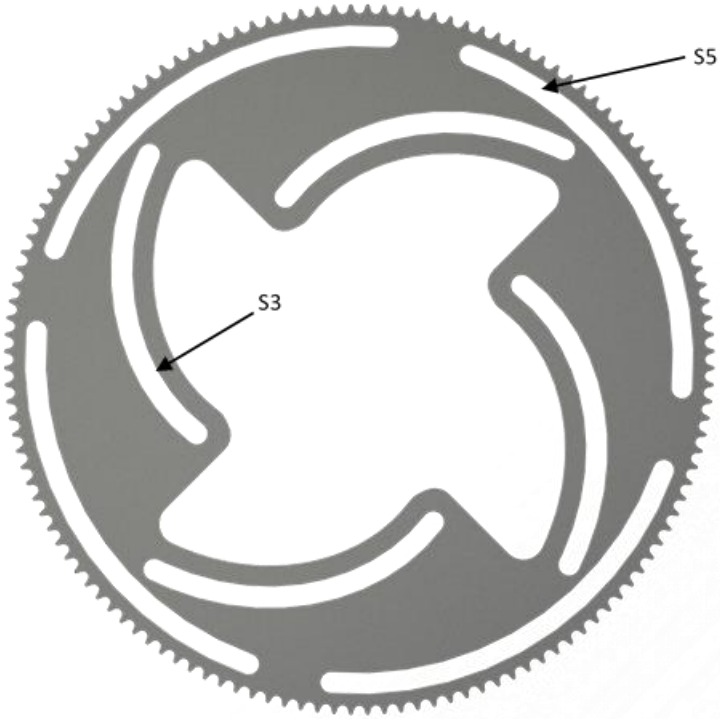

Figure 3-5 Actuator

3.3.3 Chain transmission

An ISO 05B chain is used for the transmission between the stepper motor and the actuator. Table 3-1 gives the properties of an ISO 05B chain. All of the parameters are depicted in Figure 3-6.

Table 3-1 Properties of a 05B chain [16]

Pitch [mm]	*Roller width inner plates [mm]*	*Roller width outer plates [mm]*	*Roller diameter [mm]*	*Pin diameter [mm]*	*Pin length [mm]*	*Plate depth [mm]*	*Length outer hub [mm]*
p	b_1	b_2	d_1	d_2	l_1	g	K
5	*3*	*4.77*	*5*	*2.31*	*8.6*	*7.1*	*3.1*

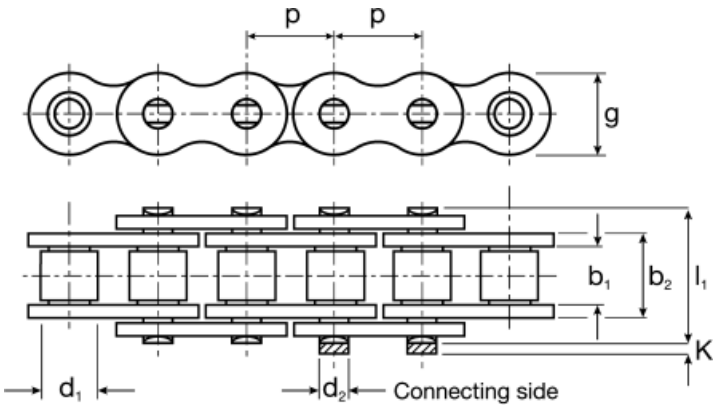

Figure 3-6 Properties of a 05B chain [16]

The dimensions of the driving and driven sprocket can be calculated using Equations 3-1 through 3-6 [16].

$$i = \frac{n_1}{n_2} = \frac{Z_2}{Z_1} \tag{3-1}$$

$$\tau_p = \frac{360^\circ}{z} \tag{3-2}$$

$$d = \frac{p}{\sin\left(\frac{\tau_p}{2}\right)} = \frac{p}{\sin\left(\frac{180^\circ}{Z}\right)} \tag{3-3}$$

$$d_f = d - d_1 \tag{3-4}$$

$$d_a \approx d * \cos\left(\frac{\tau_p}{2}\right) + 0.8\, d_1 \tag{3-5}$$

$$d_s \approx d - 2S \tag{3-6}$$

i	Gear ratio (-)
n_1	Rotational speed driving sprocket wheel (rpm)
n_2	Rotational speed driven sprocket wheel (rpm)
Z_1	Number of teeth driving sprocket wheel (teeth)
Z_2	Number of teeth driven sprocket wheel (teeth)
S	Smallest margin (= 5 mm)

All gear-parameters are depicted in Figure 3-7 where τ_p is the pitch angle of the sprocket wheel with *p* the corresponding pitch and *d* the pitch diameter. d_f, d_1, d_a, are respectively the minor, roller and major diameter. d_s is the smallest inner diameter that is necessary to assure that there is no collision between the chain an any other part. This diameter is determined by the margin *S* which is equal to 5 mm for the given chain.

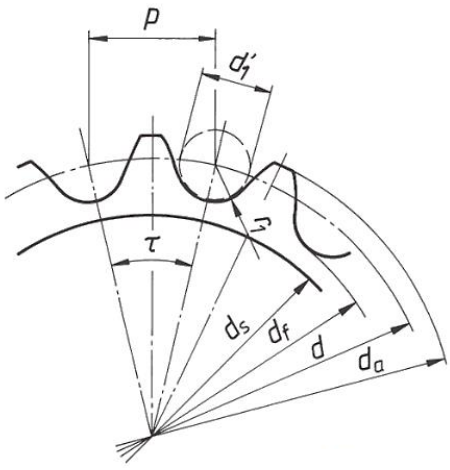

Figure 3-7 Dimension of a sprocket [16]

One of the requirements of the iris mechanism is limitation of the overall size. The actuator or driven sprocket is one of the largest parts of the mechanism and therefore determining the overall size. The outer diameter must be chosen as small as possible. The proposed pitch diameter of the driven sprocket wheel d_{driven} is 335 mm. Via Equation 3-3, the number of teeth Z_{driven} can be calculated.

$$d_{driven} = 335 = \frac{8}{\sin\left(\frac{180°}{Z_{driven}}\right)} \leftrightarrow Z_{driven} = 131.54\ teeth$$

A total of 132 teeth is used for the actuator. Further, it is recommended that the gear ratio is as high as possible. This results in smaller and therefore lighter, cheaper driving sprocket wheel. The actuator can also be positioned more accurately if a greater gear ratio is applied. A gear ratio of *i = 8.25* is chosen, resulting in a total amount of 16 teeth of the driving sprocket wheel. In Table 3-2, an overview of the sprocket wheels dimensions is given for the given chain. These dimensions are calculated per Equations 3-1 to 3-6.

Table 3-2 Dimensions of the sprocket wheels

	Pitch angle τ_p [°]	Pitch diameter d [mm]	Minor diameter d_f [mm]	Major diameter d_a [mm]	Safety diameter d_s [mm]
Driven	*2.73*	*336.17*	*331.17*	*340.07*	*315.98*
Driving	*22.5*	*41.01*	*36.01*	*44.22*	*31.01*

Equation 3-7 gives the amount of links X_0 needed in the chain to complete the transmission. A distance between two centers of the sprocket wheels e_0 of 350 mm results in 169.26 links needed. It is obvious that the amount of links needs to be an integer. A total of 170 links are used. Equation 3-8 is used to calculate the actual distance between the centers of the sprockets wheels *e* in function of the exact amount of links *X*. This results in distance *e* of 353.11 mm. The backplate is provided with a sliding mechanism which allows manual adjustment of the distance e. This ensures that the chain is always under tension.

$$X_0 = \frac{2*e_0}{p} + \frac{Z_1+Z_2}{2} + \left(\frac{Z_2-Z_1}{2\pi}\right)^2 * \frac{p}{e_0} \qquad (3\text{-}7)$$

$$e = \frac{p}{4} * \left[\left(X - \frac{Z_2-Z_1}{2}\right) + \sqrt{\left(X - \frac{Z_2-Z_1}{2}\right)^2 - 2\left(\frac{Z_2-Z_1}{\pi}\right)^2} \right] \qquad (3\text{-}8)$$

3.3.4 Backplate

One of the requirements is that the iris mechanism is mountable on the existing solar reactor in the STTL. Since the blades can not be mounted directly on the solar reactor, a backplate will be manufactured. This plate is the backbone of the mechanism as it will support the blades, the transmission mechanism and the motor without interfering with the translation of the blades.

The backplate is mounted with 8 M8 bolts and nuts on the reactor. To minimize the surface where heat can be exchanged from the reactor to the mechanism and vice versa, washers are placed between the iris mechanism and the reactor's flange. As it is seen in Figure 3-8, three pin-slots mechanisms (P1-S1, S2-P2 and P4-S4) assist the translational movement of the blades when the actuator rotates. The pins P1 and P4 are M6 bolts welded on the backplate. These pins are provided with a screw thread, so a nut can be used to attach the blade to the backplate. To prevent the thread from damaging the slot on the blade, a small bushing is placed on the bolt. The other pin-slot mechanism consists of a slot (S2) welded on the backplate and a pin (P2) attached to the blade. To assure that all of the pins and slots welded on the backplate are positioned with a high accuracy, their shape is first cut out of the backplate.

The backplate supports the actuator by using 4 M6 bolts (P5), welded on to the backplate. Also for these bolts, bushings are used and their position are first cut out of the backplate. The bushing and nut determine the distance between the backplate and the actuator.

In order to optimize the topology of the backplate, surfaces that do not have a structural function in the backplate are cut out to reduce the overall mass of the iris mechanism. The final design of the backplate is seen in Figure 3-8.

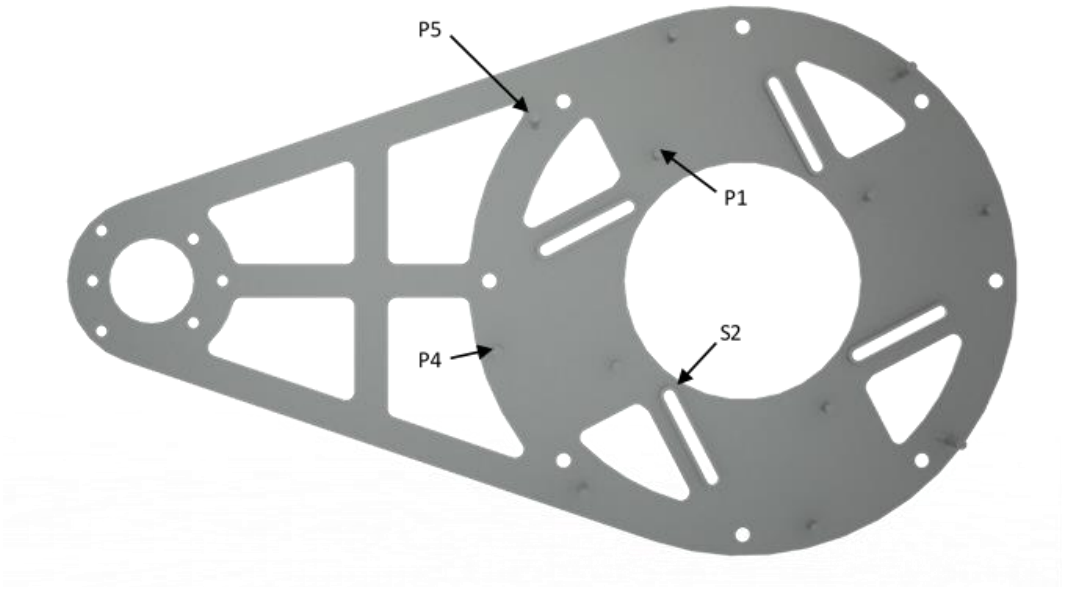

Figure 3-8 Backplate

To attach the stepper motor into the mechanism, a connection is designed between the backplate and the stepper motor. In Section 3.3.3, the exact distance between the centers of the sprockets is calculated. However, to be sure that the chain is always under tension, especially when it has plasticly deformed, another pin-slot mechanism is designed. That way, the distance between the two centers is adjustable. This can be seen in Figure 3-9.

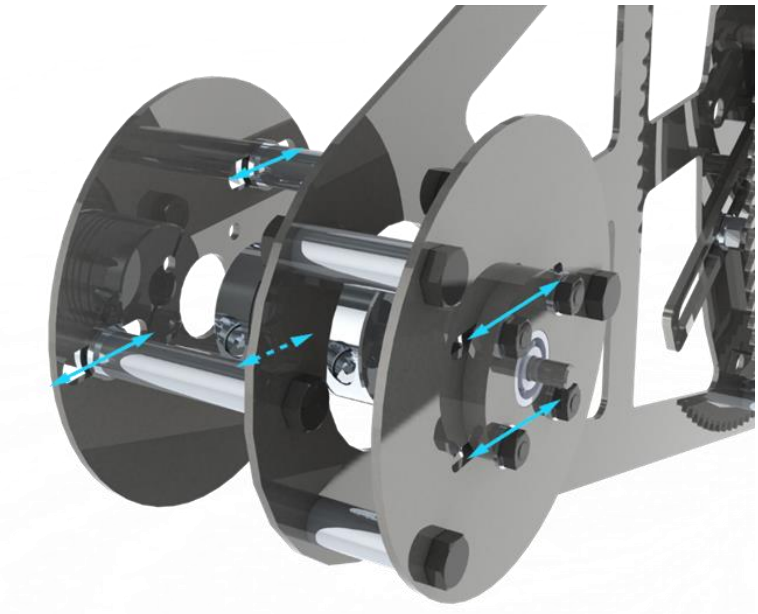

Figure 3-9 Connection motor

3.4 Algebraic modelling

This section in the methodology covers the algebraic modelling of the created mechanism. Four main analyses will be discussed:

1. **The aperture surface -** To form an equation which gives the aperture surface as function of the rotation of the stepper motor.
2. **The force analysis -** To investigate which torque the stepper motor must provide to translate the four blades.
3. **TracePro analysis -** On the one hand to determine the flux maps going through the variable aperture and on the other hand to model the flux absorbed by the blades.
4. **Blocked radiation -** To identify the total amount of blocked radiation and compare this with the absorbed radiation from the TracePro analysis

3.4.1 Aperture surface

The key feature of the iris mechanism is the variable surface of the opening. The value of this aperture determines the amount of incoming flux. The main goal of this section is to draft an equation where the aperture surface is calculated in function of the angle of the stepper motor, so the aperture can be settled. At the end of this section, a comparison with CAD measurements is made.

An angle of 0° of the motor shaft θ_{motor} corresponds to a minimal aperture, which has an equivalent reference diameter of 20 mm. In Section 3.3.3, a gear ratio *i* of 8.25 is chosen. The relation between the rotation angle of the motor shaft θ_{motor} and the rotation angle of the actuator $\theta_{actuator}$ can be expressed with this gear ratio as:

$$\theta_{motor} = 8.25 * \theta_{actuator} \tag{3-9}$$

The relation between the distance *a*, as depicted on Figure 3-2 and Figure 3-10, and the rotation of the actuator and the motor shaft is developed. These equations are established using Figure 3-10 and knowing from Section 3.3.2 that r_{slot}, as depicted on Figure 3-10, increases by 5 mm if the actuator rotates 6.25°. This parameter has a minimal value of 85.4 mm which is represented as $r_{slot,min}$ in the equations.

$$r_{slot}(\theta_{actuator}) = \frac{5}{6.25} * \theta_{actuator} + r_{slot,min} \tag{3-10}$$

$$r_{slot} = \sqrt{30^2 + (70 + a)^2} \tag{3-11}$$

$$a(\theta_{actuator}) = \sqrt{\left(\frac{5}{6.25} * \theta_{actuator} + r_{slot,min}\right)^2 - 30^2} - 70 \tag{3-12}$$

$$a(\theta_{motor}) = \sqrt{\left(\frac{5}{51.56} * \theta_{motor} + r_{slot,min}\right)^2 - 30^2} - 70 \tag{3-13}$$

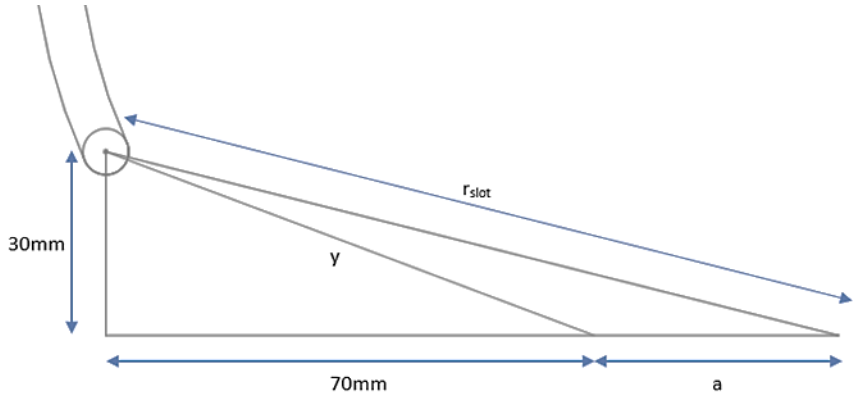

Figure 3-10 Dimensions slot mechanism

Figure 3-11 illustrates the slot mechanism of the actuator, where β = 68.75° corresponds to the maximal angle that the actuator can rotate. $r_{slot,min}$ which is equal to 85.4 mm is the minimal distance between the slot and the center of the solar reactor. Pin P3 on the blade is located in this position when the angle of the actuator is 0°. $r_{slot,max}$ which is equal to 140.4 mm is the maximum distance. Pin P3 on the blade is located in this position if the angle of the actuator is β.

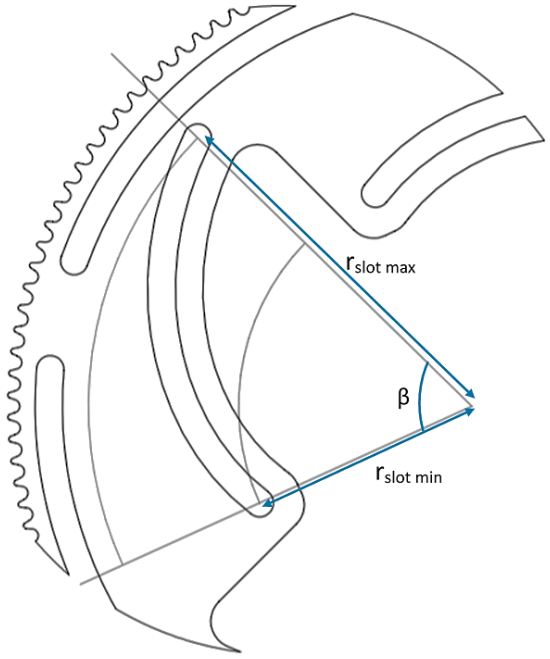

Figure 3-11 Visualisation of the slot mechanism of the actuator

The next step is to define the relation between the translation, expressed as *a*, of the blades and the surface of the aperture. As it is seen in Figure 3-12, the aperture does not have a perfectly circular shape. This means that the aperture must be calculated using another geometrical shape. Figure 3-12 shows an approximation. The aperture can be divided in four sets of two triangles where the angle φ, as depicted on Figure 3-12, slightly changes as the aperture changes. The surface area can best be approximated if this angle φ is equal to 20° and 40° when the iris mechanism is respectively at its maximum and smallest opening. A linear regression between these two extremes is given by eq. 3-14 and determines the evolution of angle φ as function of the rotation of the motor.

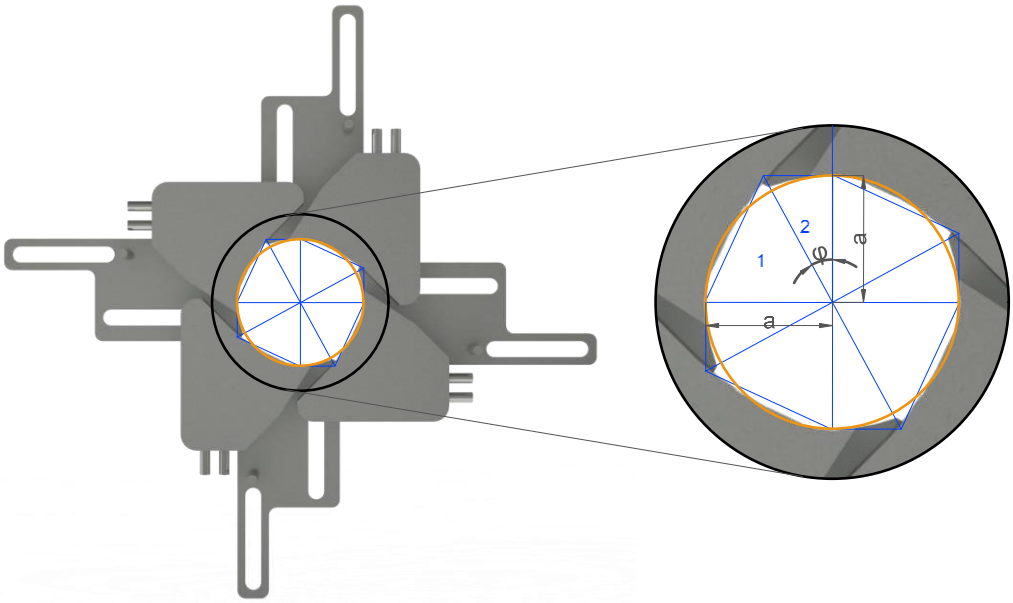

Figure 3-12 Non-circular shape of the aperture

Linear regression of angle φ as function of the rotation of the motor:

$$\varphi = 40 - \frac{20-40}{550-0}\theta_{motor} = 40 - \frac{2}{55}\theta_{motor} \quad (3\text{-}14)$$

The total surface of the eight triangles A_{eq} can be calculated using Equations 3-15 and 3-16:

$$A_1 + A_2 = \frac{a*a}{2} + \frac{a*b}{2} = \frac{a^2}{2} + \frac{a*a*\tan\varphi}{2} = \left(\frac{1}{2} + \frac{\tan\varphi}{2}\right) * a^2 \quad (3\text{-}15)$$

$$A_{eq}(a) = 4 * (A_1 + A_2) = 4 * \left(\frac{1}{2} + \frac{\tan\varphi}{2}\right) * a^2 \quad (3\text{-}16)$$

A_1	Surface area of triangle 1 (mm^2)
A_2	Surface area of triangle 2 (mm^2)

Equations 3-13, 3-14 and 3-16 combined gives the overall relation between the angle of the stepper motor θ_{motor} and the approximation of the aperture surface area A_{eq}.

$$A_{eq}(\theta_{motor}) = (2 + 2 * \tan(40 - \frac{2}{55}\theta_{motor})) * \left(\sqrt{\left(\frac{5}{51.56} * \theta_{motor} + 85{,}4\right)^2 - 30^2} - 70\right)^2 \quad (3\text{-}17)$$

In Figure 3-13, the comparison between the surface area of the aperture calculated based on the reference diameter, Equation 3-17, and CAD measurements is depicted. The absolute percentage errors for all the calculated areas based on the established equation and the circular area relative to the CAD measurements is added as a column chart. Based on this column chart, it can be seen that calculating the aperture surface area with the established Equation 3-17 will result in a higher accuracy for the aperture surface area. If a closed loop control system is ever used to regulate the incoming flux in the reactor, it is necessary to identify the aperture surface based on the actual manufactured mechanism. Therefore, an experiment will be executed to calculate the area as function of motor rotation. This experiment is discussed in section 5.1.

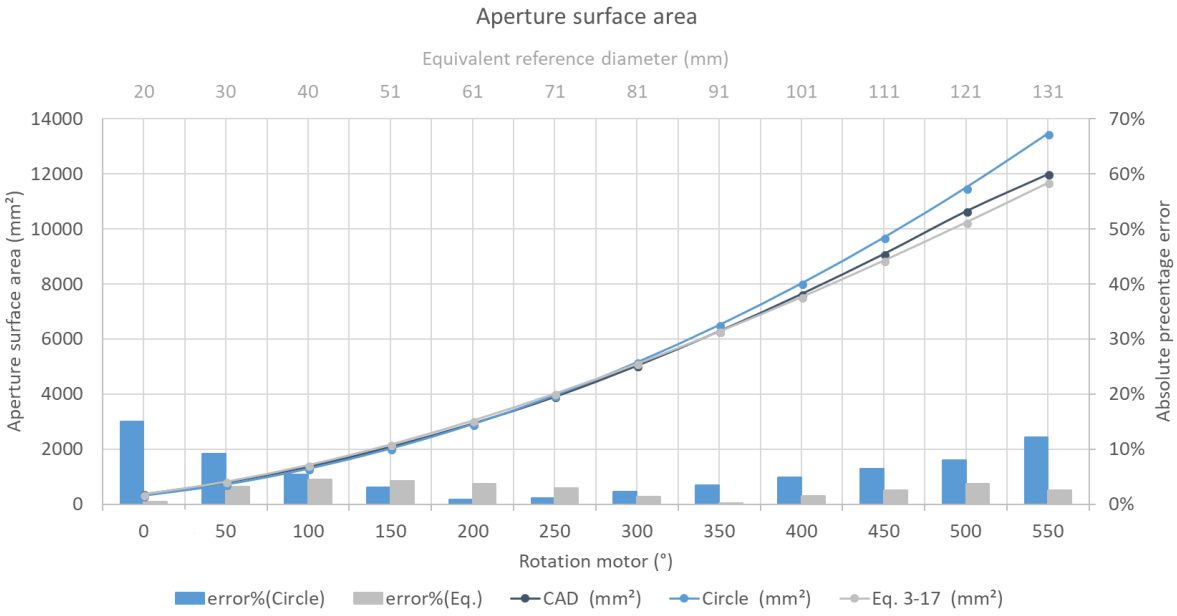

Figure 3-13 Plot of the calculated apertures

3.4.2 Force analysis

The forces and torque needed to translate the blades is analysed in this section. To perform this analytic study, a few assumptions need to be made. First, the blades are not tightened to the backplate, therefore the friction force between the blades and the backplate is negligible. Secondly, because the blades do not touch each other, the friction forces between the blades themselves is assumed equal to zero. Lastly, since the flow rate of the inner cooling system is low, the linear momentum caused by the water can be neglected.

A three-dimensional free body diagram is in equilibrium, if the sum of all the forces and the sum of all of the momentums acting on the body are equal to zero. When these forces and momentums acting on the body are split into the *x*-, *y*- and *z*-direction, six scalars. Equations 3-18 and 3-19 can be used to solve this problem. Since the blades only translate in one direction parallel to the backplate and the sprocket wheels rotate around one axis, only a two-dimensional free body diagram is needed to solve the force analysis.

$$\sum F_x = 0; \quad \sum F_y = 0; \quad \sum F_z = 0; \tag{3-18}$$

$$\sum M_x = 0; \quad \sum M_y = 0; \quad \sum M_z = 0; \tag{3-19}$$

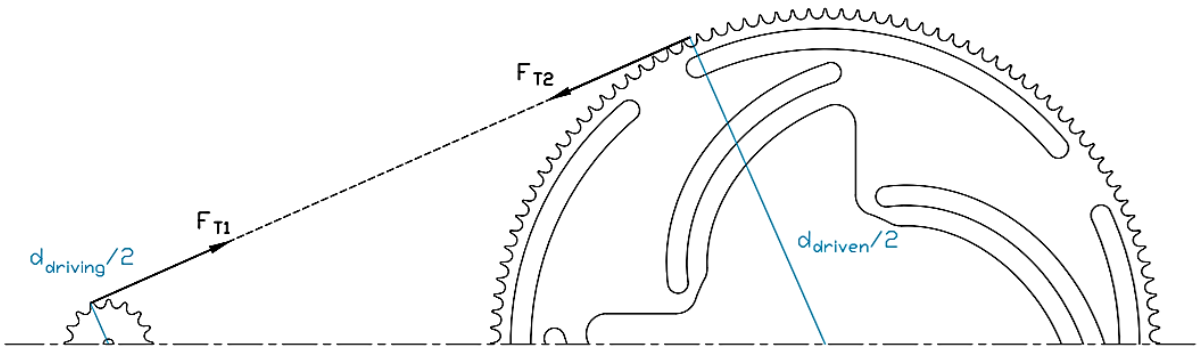

Figure 3-14 Forces acting on the chain

Figure 3-14 illustrates the tension forces F_{T1} and F_{T2}. The force F_{T1} is generated by the stepper motor's torque M_{motor} and can be identified by using the pitch diameter d_{driven} of the driving sprocket wheel as formulated in Equation 3-20. Equation 3-21 gives the relation between the chain force and the torque $M_{actuator}$ acting on the actuator wheel. Knowing that the two tension forces F_{T1} and F_{T2} are equal but in opposite direction, Equation 3-22 is established, with *i* the transmission ratio equal to 8.25.

$$F_{T1} = M_{motor} * \frac{d_{driving}}{2} \quad (3\text{-}20)$$

$$M_{actuator} = F_{T2} * \frac{2}{d_{driven}} \quad (3\text{-}21)$$

$$M_{motor} = M_{actuator} * \frac{1}{i} \quad (3\text{-}22)$$

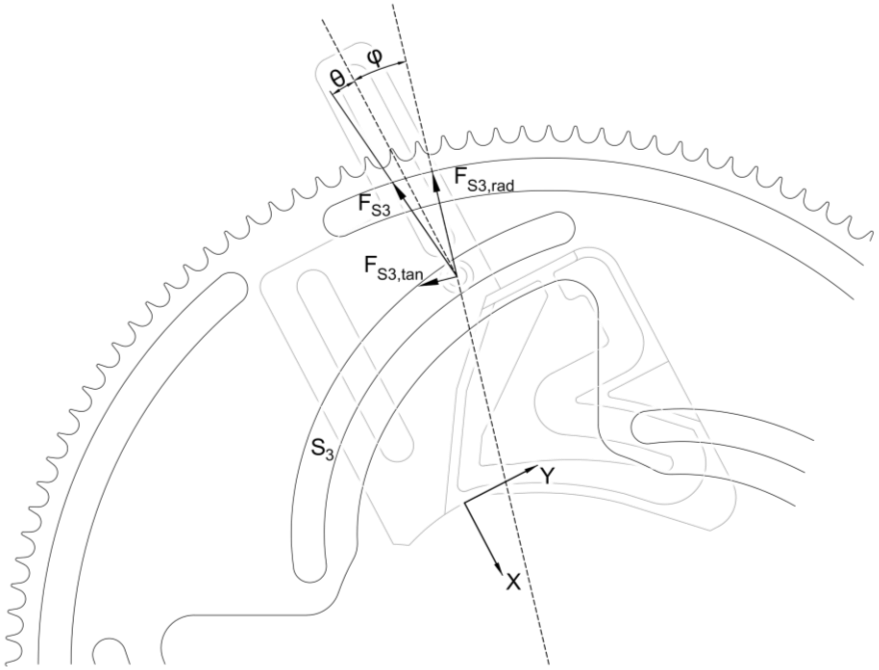

Figure 3-15 Reaction force acting on actuator

To identify the torque $M_{actuator}$, all of the tangential forces acting on the actuator should be known. For this calculation, one extra approximation is made. The friction forces in pin 5 are neglected. This approximation is valid if the neglected friction forces are significantly smaller than the tangential forces $F_{S3,tan}$ acting on slot 3. As it is seen in Figure 3-15, the pins of the blades give a reaction force F_{S3} on the actuator. As mentioned in Section 3.3.1, the friction force induced by F_{S3} is preferably as low as possible. Since a bearing will be used, the friction force in S3 is zero. This results in a reaction force which is always perpendicular to slot 3. F_{S3} can be divided into a tangential component $F_{S3,tan}$ and a radial component $F_{S3,rad}$. Where $F_{S3,tan}$ is used to identify the necessary torque acting on the actuator to translate the blades.

$$F_{S3,tan} = F_{S3} * \sin(\theta + \varphi) \quad (3\text{-}23)$$

$$F_{S3,rad} = F_{S3} * \cos(\theta + \varphi) \quad (3\text{-}24)$$

Where θ is the angle between F_{S3} and the x-axis. φ is the angle between r_{slot} and the *x*-axis of each blade as depicted in Figure 3-15. Both angles are variables in function of r_{slot}. This

dependence is given by Equation 3-25 and 3-26. Where the variable *a* is given in function of r_{slot} by Equation 3-11.

$$\theta = 90° - \psi - \omega \quad (3\text{-}25)$$

$$\varphi = \tan^{-1}\left(\frac{30}{62.5+a}\right) \quad (3\text{-}26)$$

With $$\psi = \sin^{-1}\left(\frac{(r_{slot}-5)*\sin(6.25°)}{c}\right) \quad (3\text{-}27)$$

$$\omega = \sin^{-1}\left(\frac{30}{r_{slot}}\right) \quad (3\text{-}28)$$

$$c = \sqrt{r_{slot}^2 + (r_{slot}-5)^2 - 2 * r_{slot} * (r_{slot}-5) * \cos(6.25°)} \quad (3\text{-}29)$$

The moment $M_{blade,i}$ is the moment that the actuator must provide to one blade to induce a translate motion of this blade. This necessary torque can by calculated using Equation 3-30.

$$M_{blade,i} = r_{slot} * F_{S3,tan,i} \quad (3\text{-}30)$$

The total moment $M_{actuator}$ that the actuator must provide to induce a motion of all the blades is the sum of the moments $M_{blade,i}$ which is given by Equation 3-31.

$$M_{actuator} = \sum_{i=1}^{4} M_{blade,i} = \sum_{i=1}^{4}(r_{slot} * F_{S3,tan,i}) = r_{slot} * \sum_{i=1}^{4}\left(F_{S3,i} * \sin(\theta + \varphi)\right) \quad (3\text{-}31)$$

Equations 3-10, 3-22 and 3-31 combined gives Equation 3-32. This equation gives the relation of the torque needed by the stepper motor in function of the angle θ_{motor} of the stepper motor. Where the values of the variables F_{S3}, θ and φ also depend on the value of the angle θ_{motor}.

$$M_{motor} = \frac{1}{i} * \left(r_{slot\,min} + \frac{5}{50} * \theta_{motor}\right) * \sum_{i=1}^{4}\left(F_{S3,i} * \sin(\theta + \varphi)\right) \quad (3\text{-}32)$$

The only unknown variable in Equation 3-32 is F_{S3} which is the reaction force that the actuator exerts on the blade needed to translate the blade. The calculations to quantify the minimal force F_{S3}, required to translate the blades are given below.

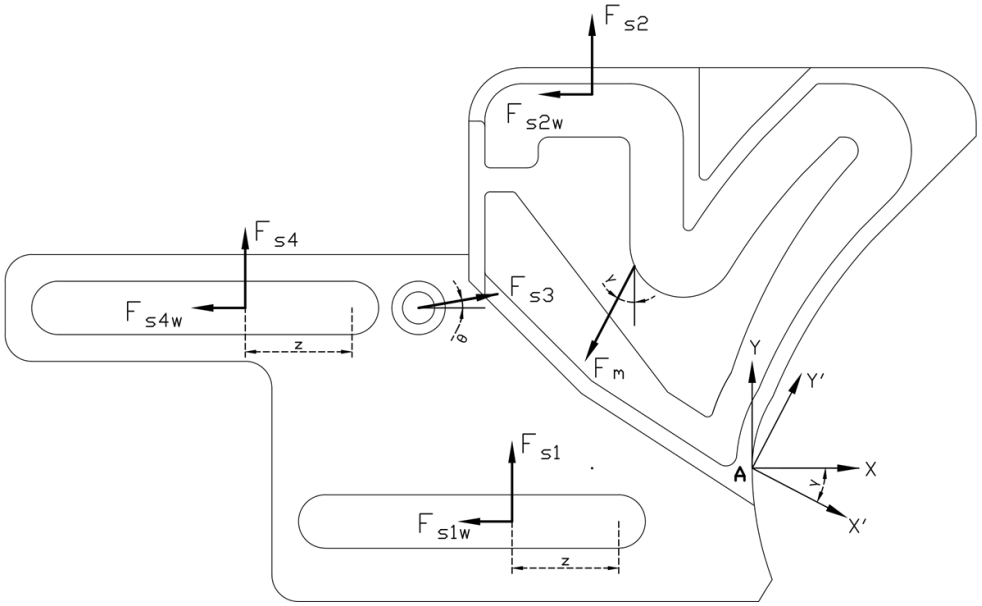

Figure 3-16 Free body diagram of the closing blades (blade A)

In Figure 3-17, a two-dimensional free body diagram of *blade A* is given. All of the forces acting on the blade can be divided into components relative to the coordinate system *x-y*. This coordinate system is constant for the four blades. The *y'*-axis in the coordinate system *x'-y'* has always the same direction as the gravitational force and will therefore change for the four blades. F_{S1} is the normal force on the blade derived from pin slot mechanism 1, F_{S2} is derived from pin slot mechanism 2 and F_{S4} from pin slot mechanism 4. F_{S1W}, F_{S2W} and F_{S4W} are the corresponding friction forces of the normal pin slot forces. The angle γ_i of the gravitational force F_m, which seizes in the center of gravity (x_{tot} , y_{tot}) of the blade, depends on the placement of each blade relative to the backplate as seen in Figure 3-17 . This angle γ_i is given in Table 3-3 for the four blades. The center of gravity, relative to the origin of the blade is calculated via Equations 3-33 and 3-34 and given in Table 3-4.

$$x_{tot} * m_{tot} = \sum_i (x_i * \rho_i * V_i) \tag{3-33}$$

$$y_{tot} * m_{tot} = \sum_i (y_i * \rho_i * V_i) \tag{3-34}$$

Table 3-3 Angle of gravitational force

Blade	γ_i [°]
A	27.5
B	117.5
C	207.5
D	297.5

Table 3-4 Center of gravity

	x_i [mm]	y_i [mm]	ρ_i [kg/m³]	V_i [mm³]	m_i [kg]
Cover	-9.69	45.77	8000	9191.28	0.074
Blade	-24.20	36.43	8000	55188.21	0.442
Water	-12.89	44.71	1000	4693.46	0.005
Total	-22.05	37.83			0.520

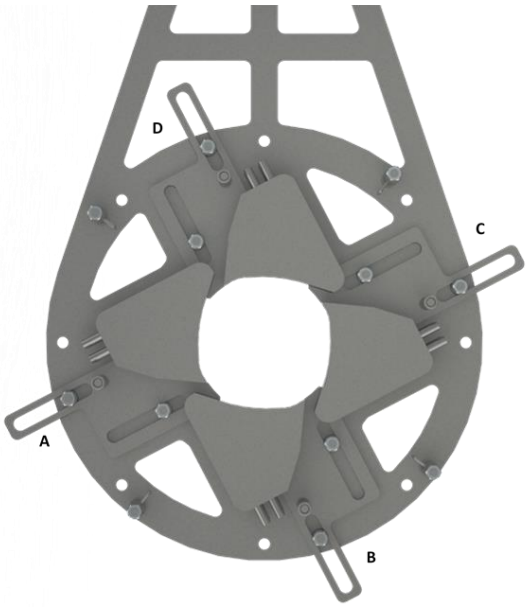

Figure 3-17 Position of the blades

Two systems of equations can be drawn up: one for the opening and one for the closing of the iris mechanism. The main difference between these two systems of equations is the direction of the friction force. The direction of the friction forces must always be opposite to the direction of the translation. In these calculations, the coefficient of friction is always assumed to be maximal, i.e. static friction. This is necessary to identify the critical force F_{S3}. Since this coefficient strongly depends on the finishing of the material, an estimation of 0.5 is made based on values found in literature [17].

Closing blades

$\sum F_x = 0$:

$$-F_{S1w} - F_{S2w} - F_{S4w} - F_m * \sin(\gamma_i) + F_{S3} * \cos(\theta) = 0 \quad (3\text{-}35)$$

$\sum F_y = 0$:

$$F_{S1} + F_{S2} + F_{S4} - F_m * \sin(\gamma_i) + F_{S3} * \cos(\theta) = 0 \quad (3\text{-}36)$$

$\sum M_o = 0$:

$$-(90 - a) * F_{S1} - 30 * F_{S2} - (130 - a) * F_{S4} - 10 * F_{S1w} + 70 * F_{S2w} + 30 * F_{s4w} + (|x_{tot}| * \cos(\gamma_i) + |y_{tot}| * \sin(\gamma_i)) * F_m - (30\cos(\theta) + 65\sin(\theta)) * F_{S3} = 0 \quad (3\text{-}37)$$

With friction force: $F_{Siw} = \mu_i * F_{Si}$ (3-38)

Solving this system of equations gives four reaction forces, one for each blade. Figure 3-18 gives the course of these reaction forces F_{S3i} in function of the aperture opening *a*. $F_{S3,C}$ and $F_{S3,D}$ are equal to zero, this means that these blades do not need a force on pin 3 to close the aperture.

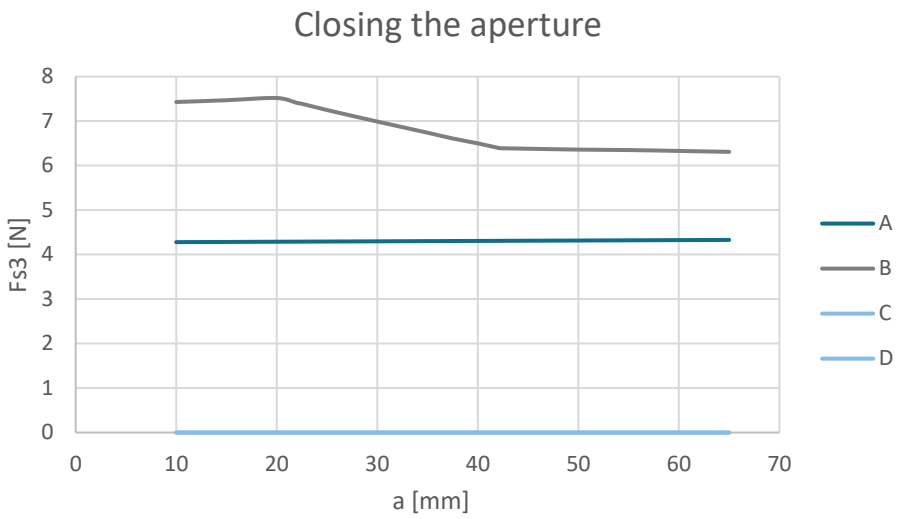

Figure 3-18 F_{S3} as function of the opening

Opening blade

$\sum F_x = 0$:

$$+F_{S1w} + F_{S2w} + F_{S4w} + F_m * \sin(\gamma_i) + F_{S3} * \cos(\theta) = 0 \quad (3\text{-}39)$$

$\sum F_y = 0$:

$$F_{S1} + F_{S2} + F_{S4} - F_m * \sin(\gamma_i) + F_{S3} * \cos(\theta) = 0 \quad (3\text{-}40)$$

$\sum M_o = 0$:

$$-(90 - a) * F_{S1} - 30 * F_{S2} - (130 - a) * F_{S4} - 10 * F_{S1w} + 70 * F_{S2w} + 30 * F_{S4w}$$
$$+(|x_{tot}| * \cos(\gamma_i) + |y_{tot}| * \sin(\gamma_i)) * F_m - (30\cos(\theta) + 65\sin(\theta)) * F_{S3} = 0 \quad (3\text{-}41)$$

With friction force: $F_{Siw} = \mu_i * F_{Si}$ (3-42)

Similar to closing the mechanism, solving this system of equations gives four reaction forces F_{S3i} needed to open the mechanism. Figure 3-20 illustrates these reaction forces F_{S3i} as function of the aperture opening *a*. $F_{S3,A}$ and $F_{S3,B}$ are equal to zero, this means that these blades do not need a force on pin 3 to open the aperture.

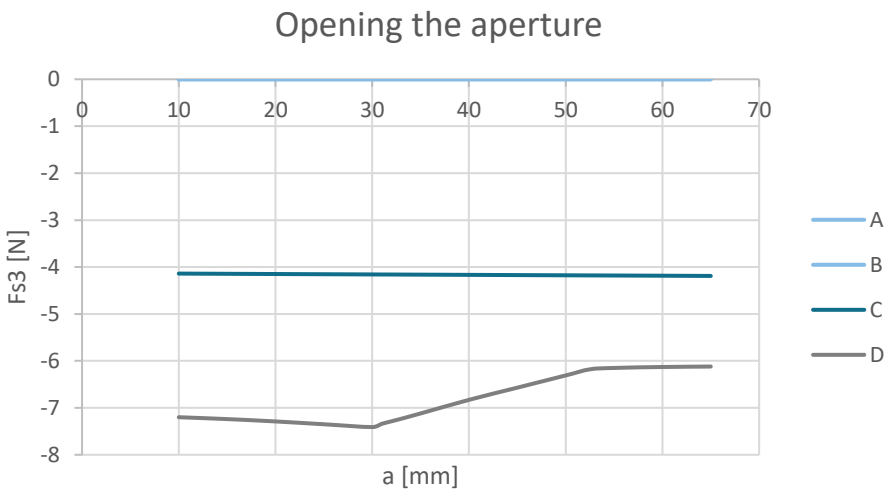

Figure 3-19 Plot reaction force slot 3 on blade for opening

Conclusion:

By using Equation 3-32, the required torque of the motor is calculated. A planetary gearbox with a gear ratio of 4 is placed between the stepper motor and the mechanism. This gear ratio is implemented in the gear ratio *i* used in Equation 3-32 and therefore also in Figure 3-20, which represents the minimum torque the stepper motor must provide to move the blades. Based on these results, it can be stated that the motor inclusive the planetary gearbox which is available in the lab is perfect for this iris mechanism, since this motor can deliver up to 0.3 Nm. The motor that will be used is stepping motor ARM46AK by Orientalmotor and the planetary gearbox is a PLE40 from Neugart.

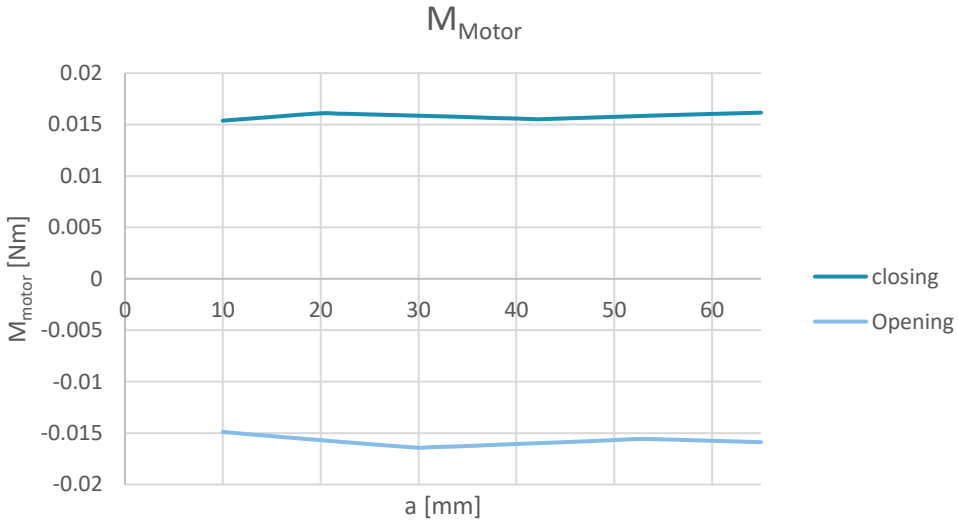

Figure 3-20 Minimum torque delivered by the motor

3.4.3 Optical analysis

TracePro® by the Lambda research corporation is a commercial software used for designing, analyzing and optimizing optical illuminations systems. It combines the Monte Carlo ray-tracing, analysis and optimization methods to simulate illumination systems with imported CAD models.

In this thesis, the TracePro® software is used to determine the flux going through the aperture of the created iris mechanism for different aperture openings. The result of these simulations is a heat flux map which can be used for further calculations for example for the solar reactor temperature or for a closed loop control system for the optimal aperture opening. Secondly the TracePro® analysis is executed to determine the amount of energy absorbed by the blades, for different aperture openings.

3.4.3.1 Monte Carlo ray-tracing method [18,19]

The Monte Carlo method is used in TracePro® to simulate the scattering and diffraction of light, and to sample of the distributions of rays emanating from light sources. Monte Carlo simulations are computational algorithms which uses the repetition of random input values to solve problems that might be deterministic. On a higher mathematical level, this method uses numerical integration to solve higher-dimensional integrals. The general form of such an integral is presented by Equation 3-43. The input variables x_i are N times sampled with a uniformly distribution over a certain domain. The integral of the function f is calculated N times and the number of times a certain event occurs n is counted. After this, a statistic analysis is executed. During this analysis an estimate of the probability p_e that this event happens can be calculated with Equation 3-44. [20,21]

$$\int \dots \int f(x_1, x_2, \dots, x_n)\, dx_1 dx_2 \dots dx_n \tag{3-43}$$

$$p_e = \frac{n}{N} \tag{3-44}$$

A ray tracing analysis is the tracing of the photons send off the light sources in all directions, where each photon has a certain wavelength. When such a photon reaches a surface, some energy is absorbed, some reflected and some transmitted. After the intersection with a couple of surfaces, the energy of the photon will be diminished and this ray can be neglected. If the photon does not intersect on a surface after a certain distance it is also neglected, since this ray will have no influence on the model. There are two main ray tracing methods: the forward ray tracing and the backward ray tracing. The forward ray tracing, also called the eye ray tracing, simulates the photons emitted by the light source and striking the sensor or surfaces in the model space. The photons follow the same direction as the light. The backward ray tracing follows the path of the photons from the sensor or surfaces to the light source. Therefore, the photons move in the opposite direction of the light. Bellow, the algorithm of forward ray tracing using the Monte Carlo algorithm is given. It is assumed that the reflective surfaces never absorb light and the sensor is a perfect absorber.

Basic Monte Carlo Path Tracing Algorithm for **forward** ray tracing:

- ***Step 1:*** *Choose a light source according to the light source power distribution. Generate a ray from that light source according to its intensity distribution. weight = 1*
- ***Step 2:*** *Trace ray to find point of intersection.*
- ***Step 3:*** *Randomly decide whether to absorb or reflect the ray.*
    - ***Step 3A:*** *If scattered,*
        - *weight *= reflectance*
        - *Randomly scatter the ray according to the BRDF (bidirectional reflectance distribution function).*
        - *Go to Step 2.*
    - ***Step 3B:*** *If the ray is absorbed by the camera film:*
        - *Record weight at x, y*
        - *Go to Step 1.*

Another way to use the Monte Carlo ray tracing method is by backward ray tracing. In this algorithm, the ray is traced in the opposite direction of forward ray tracing. The algorithm of backward ray tracing is given bellow.

Basic Monte Carlo Path Tracing Algorithm for **reverse** ray tracing:

- ***Step 1:*** *Choose a ray given starting from the eye or sensor, weight = 1*
- ***Step 2:*** *Trace ray to find point of intersection with the nearest surface.*
- ***Step 3.*** *Randomly decide whether to compute emitted or reflected light.*
    - ***Step 3A:*** *If emitted,*
        - *return weight * L_e (emission function)*
    - ***Step 3B:*** *If reflected,*
        - *weight *= reflectance*
        - *Randomly scatter the ray according to the BRDF PDF (Probability Density Function)*
        - *Go to Step 2.*

Both forward and reverse ray tracing are equivalent due to the fact that the physics of transport of light does not change if the paths are reversed. In this TracePro® analysis, the forward ray tracing algorithm is used. This is the preferred method since rather a lot of rays will be used to achieve accurate results and a heat flux map [20].

The optical illumination problem is solved by using the bidirectional reflectance distribution function (BRDF). This function defines how the light ray is reflected when it reaches an opaque surface. The BRDF is determined by two vectors, one vector for the incoming light ray $\vec{\omega}_{in}$ and one for the reflected light ray $\vec{\omega}_{out}$. Each vector is parameterised in a spherical coordinate system by its zenith angle θ and its azimuth angle ϕ as seen in Figure 3-21 and matrix notation of the two vectors bellow.

$$\vec{\omega}_{in} = \begin{bmatrix} \theta_{in} \\ \phi_{in} \end{bmatrix}$$

$$\vec{\omega}_{out} = \begin{bmatrix} \theta_{out} \\ \phi_{out} \end{bmatrix}$$

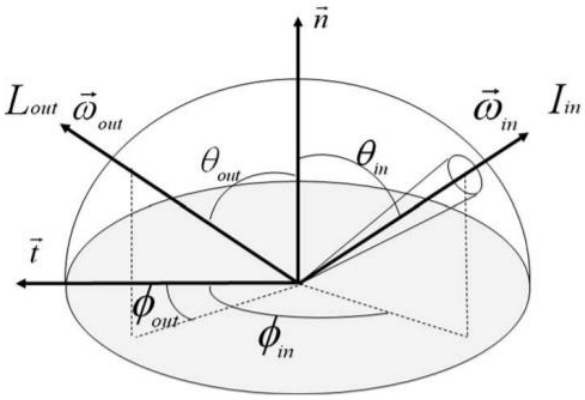

Figure 3-21 Bidirectional reflectance distribution function: surface reflection [22]

The BRDF f_{out} is a probability distribution function that describes the probability that an incoming ray of light is scattered in a random outgoing direction and is defined as the ratio of the outgoing radiance dL_{out} in direction $\vec{\omega}_{out}$ and the incoming irradiance dI_{in} in direction $\vec{\omega}_{in}$ which is seen in Equation 3-45. The differential form of this ratio is taken, so that another irradiating light does not affect the outgoing radiance.

$$f_{out}(\vec{\omega}_{in}, \vec{\omega}_{out}) = \frac{dL_{out}(\vec{\omega}_{out})}{dI_{in}(\vec{\omega}_{in})} = \frac{dL_{out}(\vec{\omega}_{out})}{L_{in}(\vec{\omega}_{in}) * \cos\theta_{in} * d\vec{\omega}_{in}} \quad (3\text{-}45)$$

f_{out}	Probability distribution function
L	Radiance ($\mathrm{W/sr.m^2}$)
I	Irradiance ($\mathrm{W/m^2}$)

3.4.3.2 Model

The model used for the TracePro® analysis is a representation of the experimental setup at the STTL laboratory. Figure 3-22 shows this used and simplified model which consists of four parts: reflector, Xenon 7 kW short arc lamp, target and iris mechanism. To minimize the computing time, the lamphouse of the simulater is omitted. The four parts need to be alligned corectly on the focal axis of the reflector. This is also important during the experimental testing.

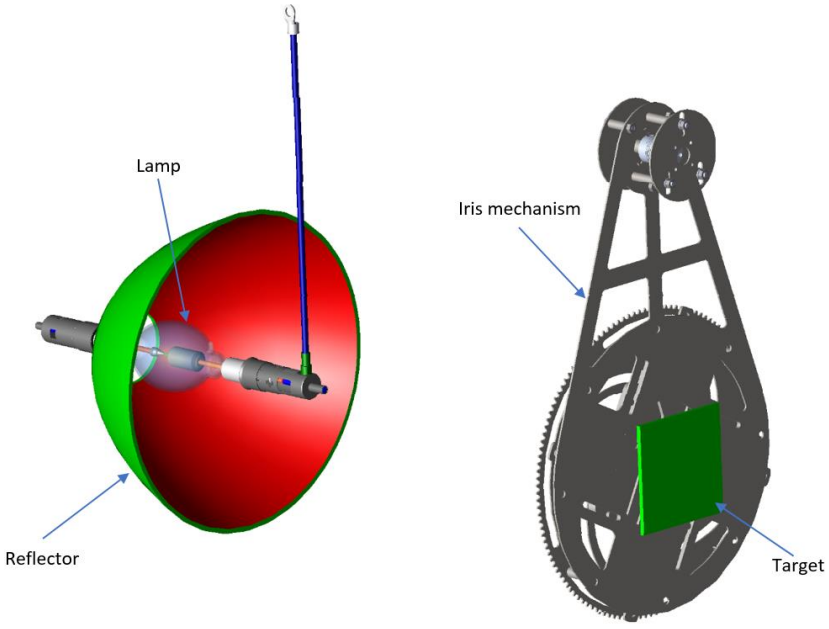

Figure 3-22 TracePro model with mechanism

The reflector has an Aluminum reflective coating on the inside. In TracePro®, this surface will be assumed to be a perfect mirror. Therefore, all of the incident rays are reflected (Γ = 1). The reflector is shaped like an ellipse, truncated at both ends. Figure 3-23 gives the characteristics of the reflector. The reflector has two focal points with an inter-focal length of 770 mm.

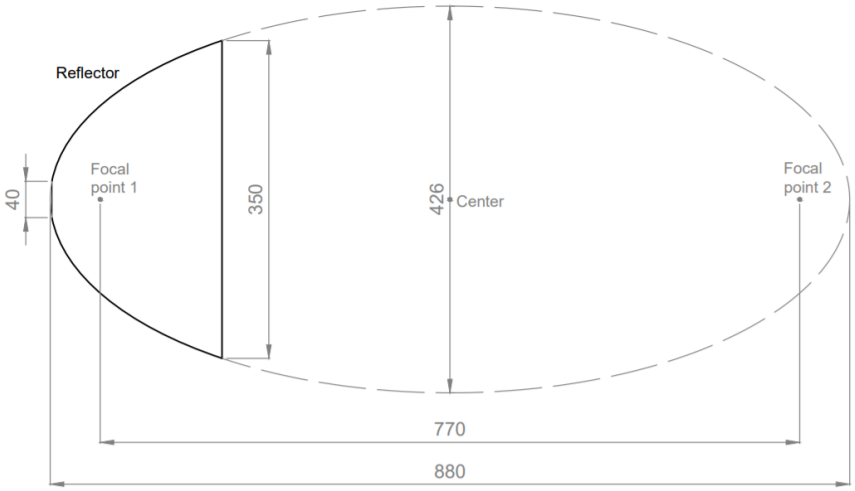

Figure 3-23 Dimensions of the elliptical reflector in mm

The light source, which is placed in the first focal point of the reflector is a 7 kW Xenon short arc lamp of Phillips. The lamp consists of a glass bulb filled with pressurised (8 bar) Xenon gas. Inside this bulb, a cathode and an anode are placed to allow electrons to flow through the gas. These electrons form the plasma arc, which is the light source of the lamp. The plasma arc of the STTL can be approximated per experimental results as a sphere at the tip of the cathode and a cylinder between the anode and cathode. The sphere has a radius of 0.975 mm and the cylinder has a radius and length of respectively 1.125 mm and 9.05 mm [12]. The surfaces of the sphere and cylinder have a Lambertian reflectance. All of the simulations are executed with the highest power level at 155 A of the lamp. To mimic the experimental flux distribution of the lamp corresponding to the chosen power level, the sphere is given a power output of 613.5 W and the cylinder has a power output of 1000 W. The Xenon lamp of the laboratory has a light spectrum close to the light spectrum of the sun. Since the properties of the rays in the simulations do not change due to its wavelength or temperature, a wavelength of 550 nm is chosen.

The target, which replaces the inlet of the solar reactor consists of a plate (140 mm x 140 mm) with the surface of a perfect absorber (Γ = 0) to determine the exact amount of energy entering the reactor. The area of the target was made a little wider than the maximum opening of the aperture of 120 mm to ensure that all the rays, going through the aperture of the mechanism, are absorbed by the target. As can be seen in Figure 3-24, the target is placed in the second focal point at a distance of 825 mm from the first vertex of the reflector. The iris mechanism is placed just in front of the target, at 800 mm.

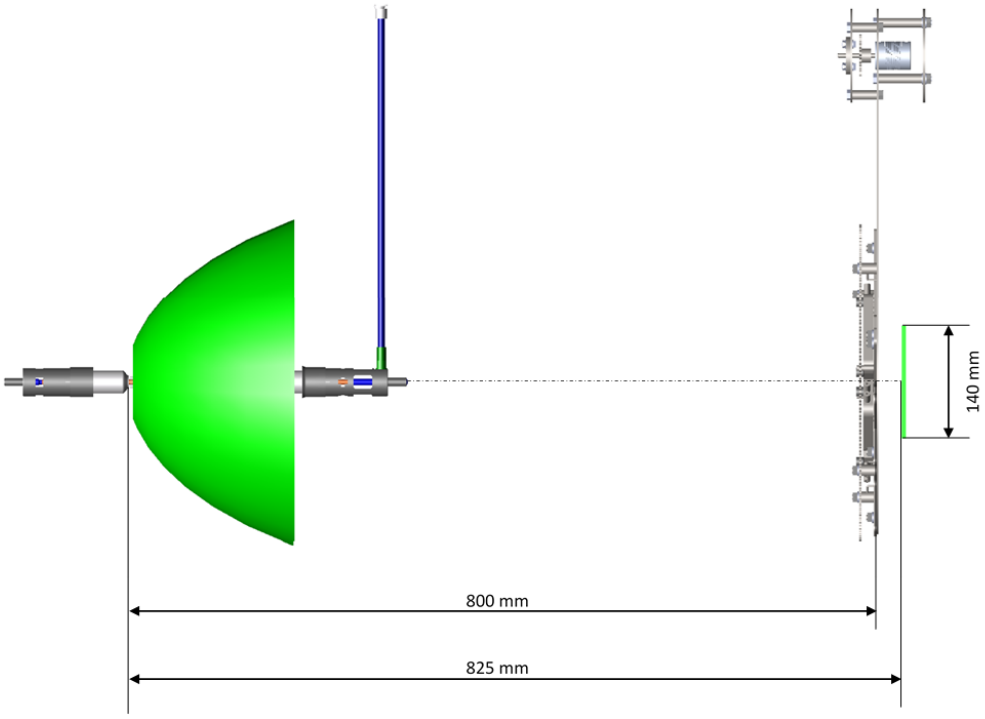

Figure 3-24 Placement of the mechanism in the TracePro® model

3.4.3.3 Simulations

The first simulations were to determine the amount of flux going through the aperture of the iris mechanism to the inside of the reactor as function of different surface reflectivity's of the blades (perfect absorber [$\Gamma = 0$]; $\Gamma = 0.2$; $\Gamma = 0.4$; $\Gamma = 0.6$) and different openings with a reference diameter between 20 mm and 120 mm. The reflection coefficient Γ is an important parameter for any optical analysis. This coefficient however, depends on the material used, surface finish and the temperature. Due to this dependence, it is impossible to find the exact value in the literature for stainless steel 316L. The simulations are executed with different values for the reflection coefficient, so that the effect of this parameter on the heat flux map can be determined. The power going inside the reactor is assumed equal to the power absorbed by the target behind the mechanism. The results of these simulations are given in Table 3-5 and Figure 3-25. From these results it can be deduced that the use of an iris mechanism is very efficient for controlling the incoming power to obtain a constant temperature inside the reactor. When varying the aperture of the iris mechanism, the amount of flux striking the target or going in to the reactor can be settled in a range of 400 W to 1000 W. The larger the aperture, the higher the amount of power striking the target, approaching a maximum value of 1016.5 W. This maximum value is obtained when no variable aperture mechanism is used. It is noticeable that the amount of power absorbed by the target is higher when the reflectivity Γ of the blades increases. Due to the thickness of the mechanism, some rays can be reflected on the inner edges, eventually striking the target. This effect is more pronounced when the reflectivity increases, resulting in a higher power entering the reactor.

Table 3-5 Power absorbed by the target

Total power absorbed by the target (W)				
Aperture (mm)	**Γ = 0**	**Γ = 0.2**	**Γ = 0.4**	**Γ = 0.6**
20	450.81	459.99	474.62	491.68
40	617.47	623.01	629.95	638.14
60	741.04	745.17	750.77	757.39
80	843.80	847.54	851.92	856.58
100	928.44	931.58	934.98	938.48
120	997.97	1000.70	1003.50	1006.50

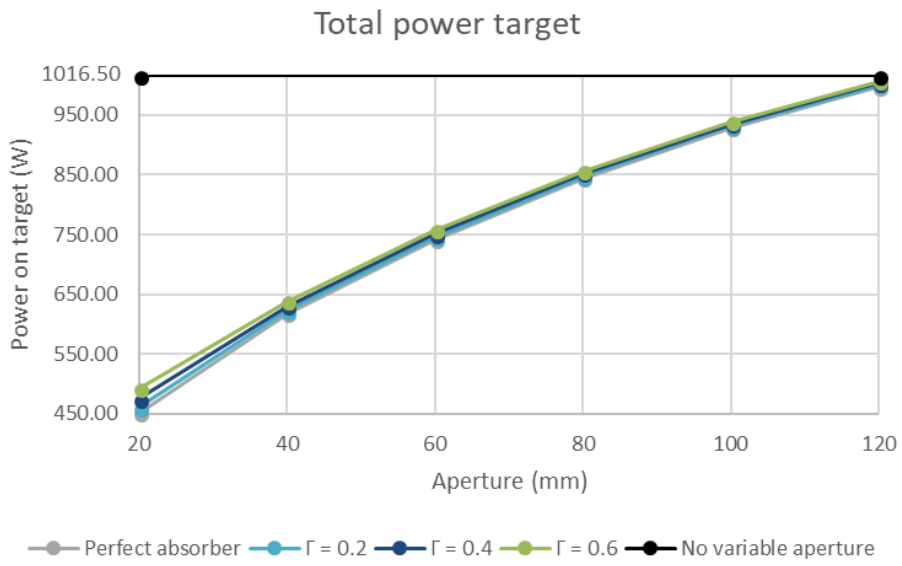

Figure 3-25 Graph of the total absorbed flux by the target

Secondly, the amount of power absorbed by the blade surfaces is also determined as function of different surface reflectivity's of the blades (perfect absorber; $\Gamma = 0.2$; $\Gamma = 0.4$; $\Gamma = 0.6$) and different openings with a reference diameter between 20 mm and 120 mm. As can be seen in Table 3-6 and Figure 3-27, it is logical that the absorbed amount of power is significantly higher when the absorptivity of the blades is closer to a perfect absorber. The absorbed power decreases and almost goes to 0 W, as the aperture becomes bigger.

Table 3-6 Power absorbed by the blades

Total power absorbed by the blades (W)				
Aperture (mm)	**Perfect absorber**	**Γ = 0.2**	**Γ = 0.4**	**Γ = 0.6**
20	602.67	521.21	428.51	315.50
40	432.44	366.41	296.06	213.17
60	321.74	266.10	209.20	146.84
80	233.71	188.98	144.32	98.25
100	162.77	130.66	98.69	66.39
120	104.63	84.00	63.40	42.68

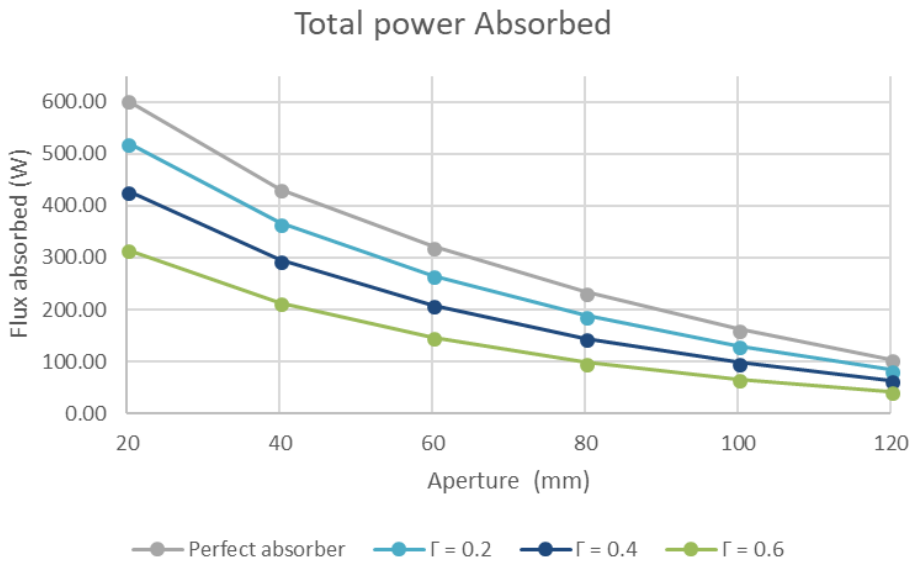

Figure 3-26 Graph of the absorbed power by the blades

The effect of the use of a variable aperture mechanism on the heat flux map entering the reactor can be seen in Figure 3-28. This figure gives a comparison between the top views of the two flux maps of one without a variable aperture mechanism and one with the iris mechanism with an aperture of 20 mm. It can be seen in this figure that a certain amount of radiation is blocked by the mechanism. The circularity of the Gaussian distribution will only slightly differ due to the non-perfect circular shape of the iris mechanism aperture, as seen in Figure 3-27 (b).

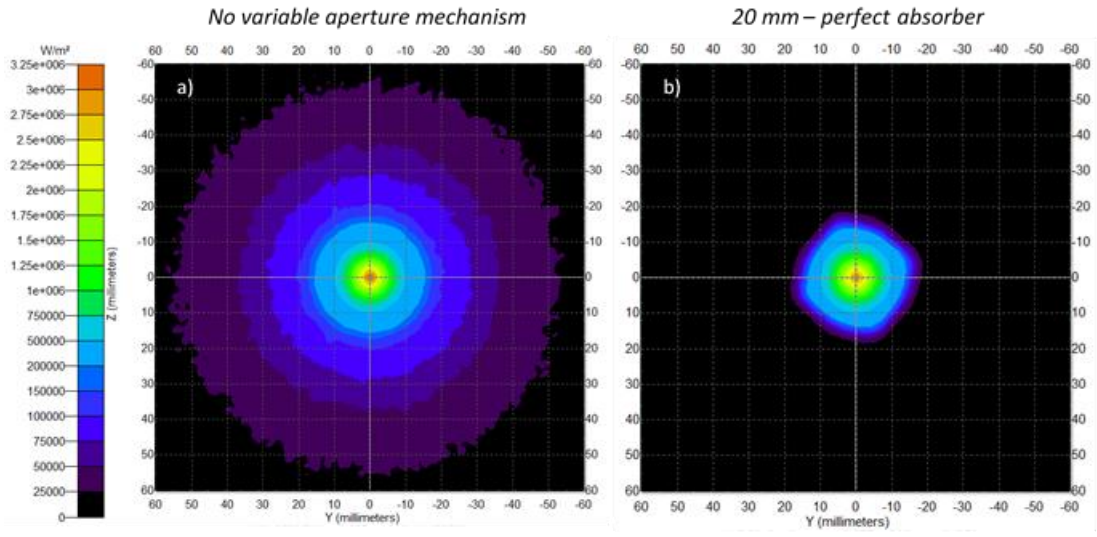

Figure 3-27 Comparison of the flux maps (a) without a variable aperture mechanism and (b) with the iris mechanism with an opening of 20 mm

3.4.3.4 Conclusion

The TracePro® simulations indicate once again that the use of a variable aperture mechanism is very effective to control the incoming power to obtain a constant temperature inside the reactor. The simulations also show that a higher absorption coefficient is preferred, since most of the reflected power on the blades will be lost to the environment instead of absorbed by the blades. Finally, the almost perfect three-dimensional gaussian distribution is only slightly distorted from its original shape without iris mechanism.

3.4.4 Blocked radiation

From section 3.4.3 the amount of absorbed power by the blades as function of the aperture is established. It is however also important to know the total amount of blocked power by the mechanism, since some minor radiation will strike the actuator, surfaces of the blades other than the top surface, etc. During the experiments, the amount of power regenerated by the cooling mechanism will be measured. These measurements will be compared with the amount of radiation blocked by the blades to identify the efficiency of the cooling mechanism. The way in which some radiation rays are blocked by the iris mechanism is depicted in Figure 3-28. In this section, an equation is established that gives the total amount of blocked radiation as a function of the opening. The amount of this blocked radiation corresponds to the volume underneath the flux maps at the position of the blades. This volume can be identified by calculating the area of the circle, having as radius *a* the distance to the center of the reactor, integrated over the range of the flux.

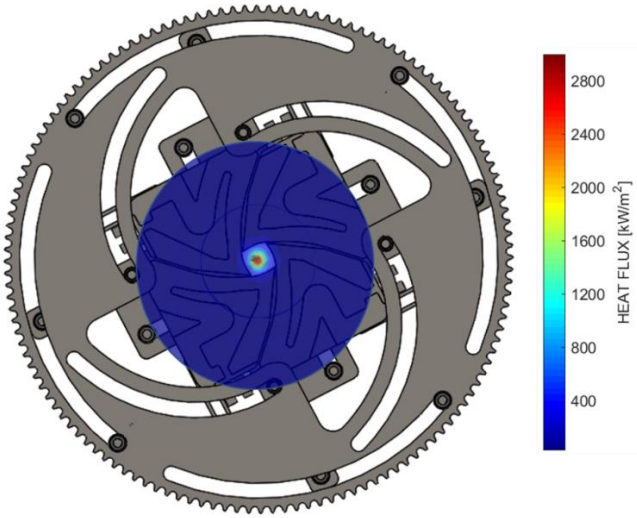

Figure 3-28 Radiation blocked by the blades

Figure 3-29 (a) gives the flux map of the radiation coming from the simulator and this at its highest power, which corresponds to a current of 155 A. Figure 3-29 (b) visualizes the regression of the flux map for a radius of 10 to 100 mm. It also illustrates the parameter *a* which is the distance from the center to the edge of the blade.

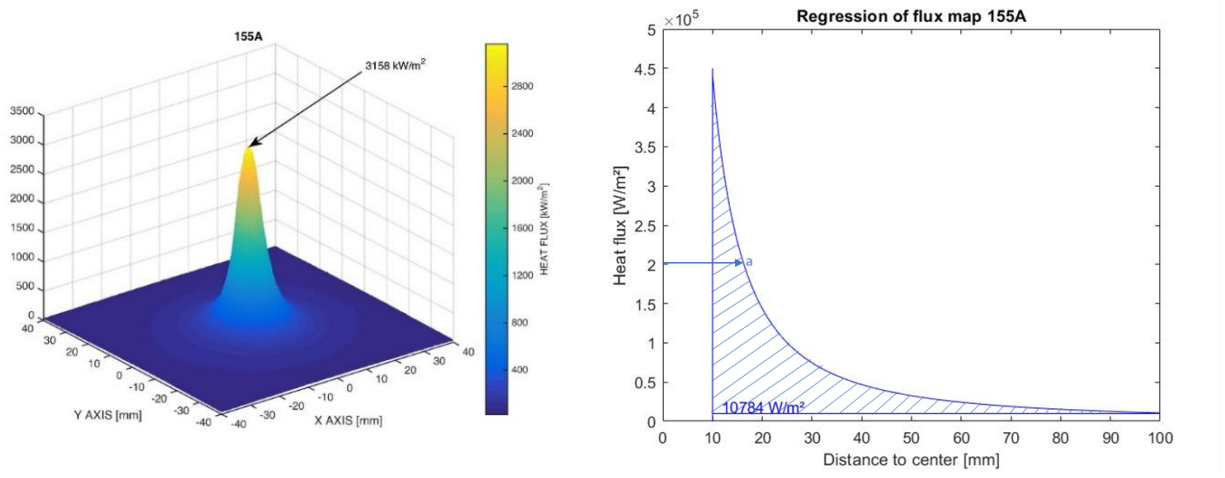

Figure 3-29 (a) 3D plot of heat flux [9], and (b) Simplified plot of heat flux corresponding to maximum power.

The flux as function of the distance to the center *q(a)* has already been measured. The inverse of this function is given by Equation 3-46 and is calculated as follows: $q^{-1}(a) = a(q)$. The area of the circle *S*, having as radius the distance to the center of the reactor *a* is given by Equation 3-47. Integrating Equation 3-47 over the range of the flux gives the volume *V* as function of the flux *q*. This integral is given by Equation 3-48. *q1* is the flux at the maximum radius which is still brought into account. At a radius of 100 mm the amount of blocked flux is negligibly small and from this distance a certain amount of flux will be blocked by the actuator and not by the blades. For these reasons it can be stated that q_1 corresponds to the flux at a radius of 100 mm. With this approximation, the blocked radiation which corresponds to the volume *V* is given by Equation 3-49 as function of the flux q_2 at the reference radius of the aperture. The relation between his flux q_2 and the reference radius *a* is presented by Equation 3-50.

$$a(q) = 30769 * q^{-0.618} \quad with\ a\ \in [10; 100]\ and\ R^2 = 0.997 \tag{3-46}$$

$$S(q) = \pi * a(q)^2 = \pi * 30769^2 * q^{-1.236} \tag{3-47}$$

$$V(q) = \int_{q_1}^{q_2} S(q)dq = \int_{q_1}^{q_2} 10^{-6} * (\pi * 30769^2 * q^{-1.236})dq$$

$$= \frac{-\pi * 30769^2}{0.236} * 10^{-6} * (q_2^{-0.236} - q_1^{-0.236}) \tag{3-48}$$

With q_1 = 10784 W/m²:

$$V(q) = 1408 - 1.26 * 10^4 * q_2^{-0.236} \tag{3-49}$$

$$With\ q_2 = 18.3 * 10^6 * a^{-1.618} \tag{3-50}$$

The amount of blocked radiation for the highest intensity of the solar simulator is calculated and depicted in Figure 3-30. The maximum amount of energy that can be blocked by the mechanism is 820 W. This corresponds to an aperture with a diameter of 20 mm.

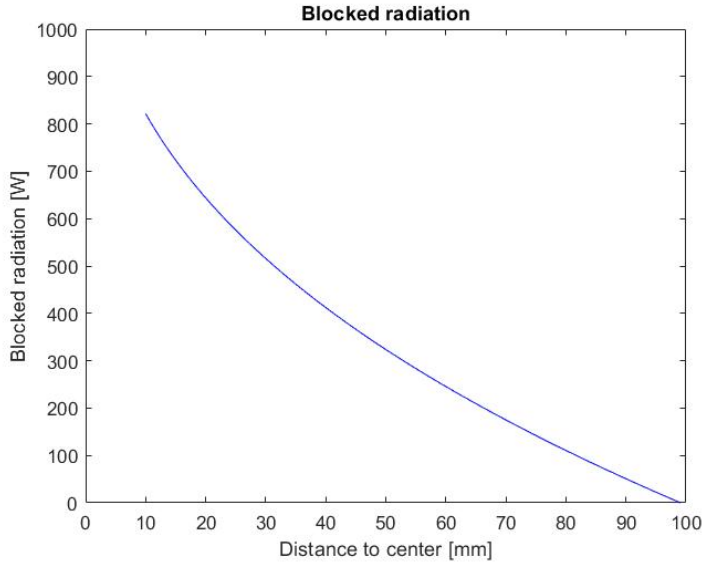

Figure 3-30 Total blocked radiation as a function of the distance to the center

It can be noticed that there is a difference between Figure 3-27 (Graph of the absorbed power by the blades) and Figure 3-31 (Total blocked radiation as a function of the distance to the center). So, not all the blocked radiation will be absorbed by the blades as expected. It should also be mentioned that both figures are based on a different method. The TracePro® simulations are

based on a validated model of the simulator, whereas the equation in this section is based on a function which approximates the results of this validated model within a range of 0 to 100 mm radius from the center of the reactor. So, the results obtained by the simulations will always have a higher accuracy compared to the results in this section.

3.5 Thermofluidic analysis

The goal of the thermofluidic analysis is to design a water channel inside the blade with the best possible cooling and energy recovery. To perform such a study, a CFD analysis is executed using Siemens NX software [23]. This software is used as an optimization tool. It should be noted that any values obtained by the simulations should always be validated with experiments. To get a better understanding of the physics and mathematics behind this CFD software, some user's guides [24, 25] and papers [26–28] were used.

3.5.1 CFD Fundamentals

3.5.1.1 Basic equations

The CFD analysis consists of a flow study and a thermal study. The flow characteristics of the water is identified by using the Navier-Stokes equations, given by Equations 3-51 to 3-55. These equations are nonlinear partial differential equations used to mathematically describe the flow per incompressible Newtonian fluids assumption. The equations describe the relation between the velocity-components u, v, w, the density ρ, the pressure P and the temperature of the fluid. The effect of the temperature of the fluid is incorporated in the term of the total energy E_t. The Navier-Stokes equations can be used for a 3D (x, y, z direction) and time t dependent problem. The remaining variables are the components of the stress tensor τ and the heat flux q in a certain direction. The equations also include the influence of the kinematic viscosity v of the fluid on the flow, contained in the Reynolds number Re and the Prandtl number Pr. The Reynolds number gives the ratio of the inertial forces to the viscous forces and is used to identify laminar or turbulent flow. The Prandtl number gives the ratio of the momentum diffusivity to thermal diffusivity. Equations 3-56 and 3-57 give the relation between the viscosity and respectively the Reynolds number and the Prandtl number. Where the other variables are the velocity V of the fluid, the reference diameter D, the density ρ, the specific heat capacity C_P and the thermal conductivity k [26, 27].

Conservation of mass:

$$\frac{\partial \rho}{\partial t} + \frac{\partial(\rho u)}{\partial x} + \frac{\partial(\rho v)}{\partial y} + \frac{\partial(\rho w)}{\partial z} = 0 \tag{3-51}$$

Conservation of momentum:

$$\frac{\partial(\rho u)}{\partial t} + \frac{\partial(\rho u^2)}{\partial x} + \frac{\partial(\rho uv)}{\partial y} + \frac{\partial(\rho uw)}{\partial z} = -\frac{\partial p}{\partial x} + \frac{1}{Re}\left(\frac{\partial \tau_{xx}}{\partial x} + \frac{\partial \tau_{xy}}{\partial y} + \frac{\partial \tau_{xz}}{\partial z}\right) \tag{3-52}$$

$$\frac{\partial(\rho v)}{\partial t} + \frac{\partial(\rho uv)}{\partial x} + \frac{\partial(\rho v^2)}{\partial y} + \frac{\partial(\rho vw)}{\partial z} = -\frac{\partial p}{\partial y} + \frac{1}{Re}\left(\frac{\partial \tau_{xy}}{\partial x} + \frac{\partial \tau_{yy}}{\partial y} + \frac{\partial \tau_{yz}}{\partial z}\right) \tag{3-53}$$

$$\frac{\partial(\rho w)}{\partial t} + \frac{\partial(\rho uw)}{\partial x} + \frac{\partial(\rho vw)}{\partial y} + \frac{\partial(\rho w^2)}{\partial z} = -\frac{\partial p}{\partial z} + \frac{1}{Re}\left(\frac{\partial \tau_{xz}}{\partial x} + \frac{\partial \tau_{yz}}{\partial y} + \frac{\partial \tau_{zz}}{\partial z}\right) \tag{3-54}$$

Conservation of energy:

$$\frac{\partial(E_t)}{\partial t} + \frac{\partial(uE_t)}{\partial x} + \frac{\partial(vE_t)}{\partial y} + \frac{\partial(wE_t)}{\partial z} = -\frac{\partial(up)}{\partial x} - \frac{\partial(vp)}{\partial y} + \frac{\partial(wp)}{\partial z} - \frac{1}{RePr}\left(\frac{\partial q_x}{\partial x} + \frac{\partial q_y}{\partial y} + \frac{\partial q_z}{\partial z}\right) + \frac{1}{Re}\left(\frac{\partial}{\partial x}\left(u\tau_{xx} + v\tau_{xy} + w\tau_{xz}\right) + \frac{\partial}{\partial y}\left(u\tau_{xy} + v\tau_{yy} + w\tau_{yz}\right) + \frac{\partial}{\partial z}\left(u\tau_{xz} + v\tau_{yz} + w\tau_{zz}\right)\right) \tag{3-55}$$

Influence of the viscosity:

$$Re = \frac{V*D}{\nu} \tag{3-56}$$

$$Pr = \frac{\nu*\rho*C_P}{k} \tag{3-57}$$

Heat generated by the solar simulator is transferred to the water. This transport is established by radiation from the simulator to the blades, by conduction through the blades, and by convection from the blades to the water. Due to this heat transfer, the temperature of the water inside the blades as well as the temperature of the blades themselves increases. Because the temperature of the blades is higher than that of the environment, heat is transferred to the environment via convection and radiation [8]. The heat transfer to the fluid is computed per Equations 2-1 to 2-3 and Equation 3-58.

$$\dot{Q} = \dot{m} C_p \Delta T \tag{3-58}$$

$\dot{Q}$	Absorbed heat (W)
$\dot{m}$	Mass flow rate (kg/s)
C_P	Specific heat capacity (J/kg.K)
ΔT	Change in temperature (K)

3.5.1.2 Mesh convergence and grid independency

Since CFD analysis solves partial differential equations, the computing time can increase extremely when no attention is paid to the mesh distribution. To achieve results with high accuracy and minimum computing time, an optimization of the mesh is executed. A total of four 3D collectors (cover, blade, water internal and water external) is used to fully mesh one blade of the mechanism. These four components are meshed using tetrahedral elements with ten nodes as it is seen in Figure 3-31. These elements are commonly used in the Siemens NX environment to mesh a volume.

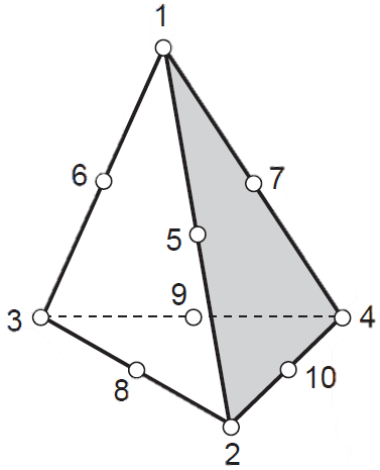

Figure 3-31 Tetrahedral cell with 10 nodes [28]

The mesh elements were refined until the percentage difference of the values of interest (Average velocity of water, average and maximum blade temperature and average convection coefficient) were less than 5%. The plots of these values were also examined to search for any large gradient in the structure. If spotted, this could lead to inaccurate results. This preliminary test results in mesh elements with a size of 1 mm for the blade, water internal and water external, and also 0.75

mm for the cover of the blade. The total mesh distribution for the blade can be seen in Figure 3-32.

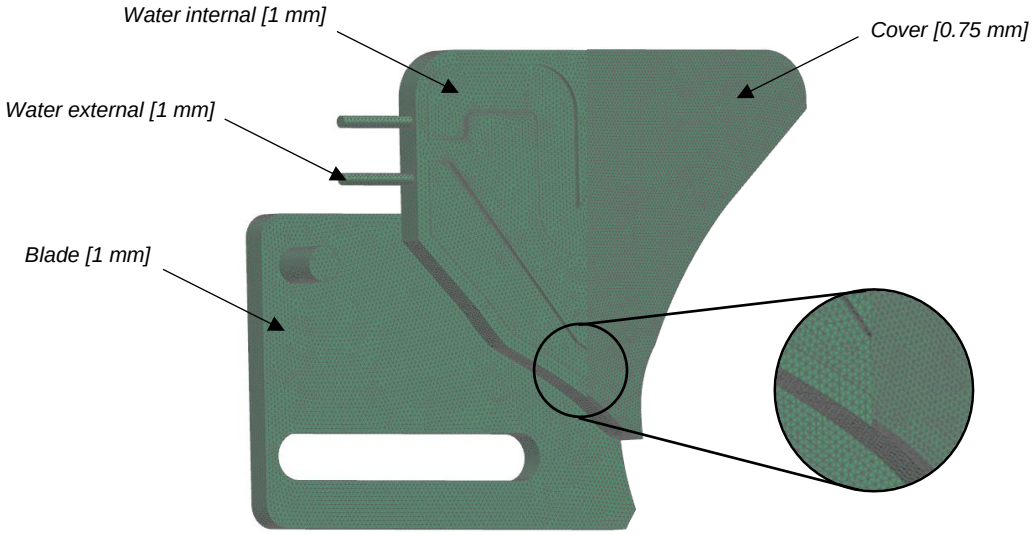

Figure 3-32 Mesh distribution

3.5.1.3 Load

The applied load on the mechanism is the heat flux available in front of the blades. This heat flux is only applied on the cover, since the other parts are mainly covered by another blade. This load is depicted in Figure 3-34. The heat flux has already been measured for the used solar simulator for three different intensities, corresponding to a certain amount of electrical current [9]. A 6th order polynomial curve can be fitted on each heat flux map using the average of the measured values. As it is seen in Figure 3-33 (b) a 6th order polynomial curve is necessary for high accuracy. Since the minimum opening of the mechanism is 20 mm, the values of the heat flux within a 20 mm diameter from the center of the solar reactor are not considered. This approximation results in even higher accuracy. Three equations with their coefficient of determination R^2 are listed in Table 3-7. The parameter *a* represents the reference radius of the aperture as seen in Figure 3-2.

Table 3-7 Heat flux curve fitting

$y(a) = c_1 * a^6 + c_2 * a^5 + c_3 * a^4 + c_4 * a^3 + c_5 * a^2 + c_6 * a + c_7$								
Intensity	***c_1***	***c_2***	***c_3***	***c_4***	***c_5***	***c_6***	***c_7***	***R^2***
115A	*2.707E-07*	*-8.789E-05*	*1.109E-02*	*-6.874E_01*	*2.184E+01*	*-3.380E+02*	*2.074E+03*	*0.985*
135A	*3.657E-07*	*-1.185E-04*	*1.491E-02*	*-9.222E-01*	*2.925E+01*	*-4.523E+02*	*2.770E+03*	*0.981*
155A	*5.166E-08*	*-1.836E-05*	*2.615E-03*	*-1.909E-01*	*7.560E+00*	*-1.567E+02*	*1.415E+03*	*0.998*

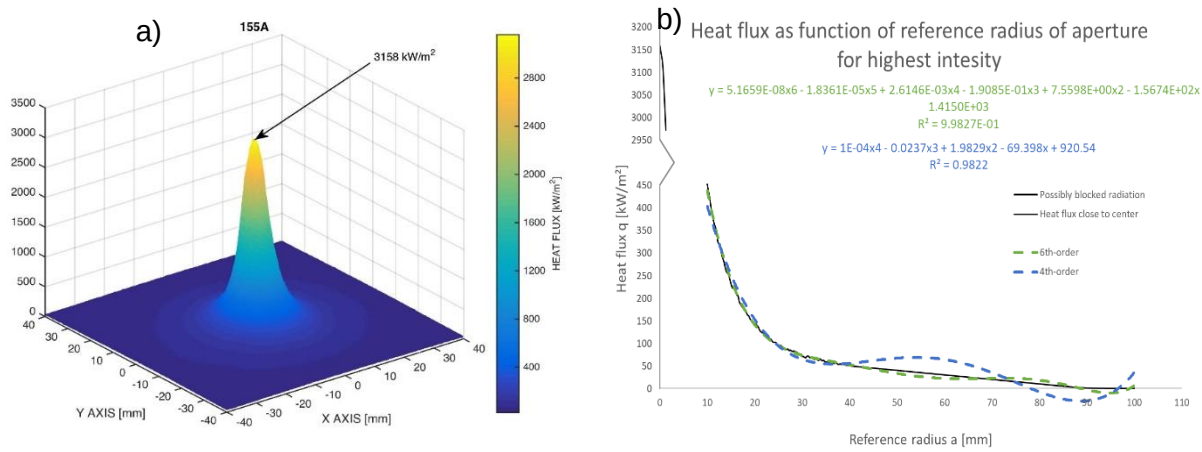

Figure 3-33 (a) Heat flux map for 155A [9], and (b) Numerical approximation

3.5.1.4 Constraints

The constraints for the flow study are the inlet of the water flow at a certain position and with a certain flow rate and the outlet at a certain position. The constraints for the thermal study are the natural convection and radiation from the blade to the environment with certain emissivity (material-parameter) as seen in Figure 3-34. The connection between the cover and the blade is specified as a *perfect connection*, which is valid for a welded connection. This is not visible on Figure 3-34.

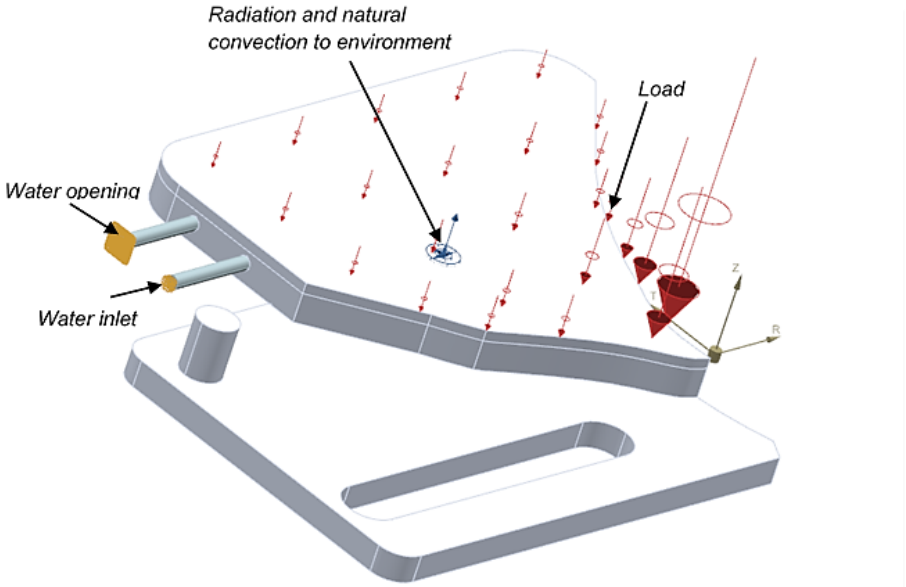

Figure 3-34 Constraints and load on blade

3.5.1.5 Material

Due to the high radiative flux, the material of the blades is exposed to very high temperatures. To make sure that the mechanism will not fail even if the cooling does not work, a material with a high melting point and high creeping temperature point should be selected. For example, Aluminum with melting point of only 993 K will therefore not be used [29]. Other parameters like high heat conductivity, low thermal expansion, the weldability, etc. are the determining factors for the material selection.

Stainless steel 316L meets all the requirements and therefore is used for the whole mechanism. Material properties are given in Appendix C.

3.5.2 Optimization study

Optimization of the design is based on achieving the best possible cooling efficiency, i.e. the largest heat transfer from the solar simulator to the water in the blades, without damaging the blades due to its high temperature. The mechanism should never exceed a temperature of 600 °C. This is the temperature at which 316L starts to show significant creep deformation under the influence of mechanical stresses [30]. During the optimization study, one should bear in mind that a steam turbine will be used to convert the produced steam into electricity.

As it is seen in Equations 2-1, 2-3 and 3-46, there are five variables which will influence this heat transfer to the water (k, h, A_s, C_P, $\mathcal{E}$). Since the conduction coefficient k and the heat capacity C_P are material parameters, these variables will not be influenced by the design of the blade. The optimization study can be seen as optimizing the other three parameters h, A_s and $\mathcal{E}$. All of the simulations in this chapter are executed for smallest aperture of 20 mm and with highest intensity of the solar simulator which corresponds to current of 155 A.

3.5.2.1 General design

First, different designs are made and simulated with Siemens NX. Simulation results can be used to identify the water flow inside the blades. Based on these results some adjustments can be made to the design, so a new and better blade can be designed and simulated. In Figure 3-36, the evolution of this optimization process can be seen. A total of eight different designs are simulated before achieving the preliminary design.

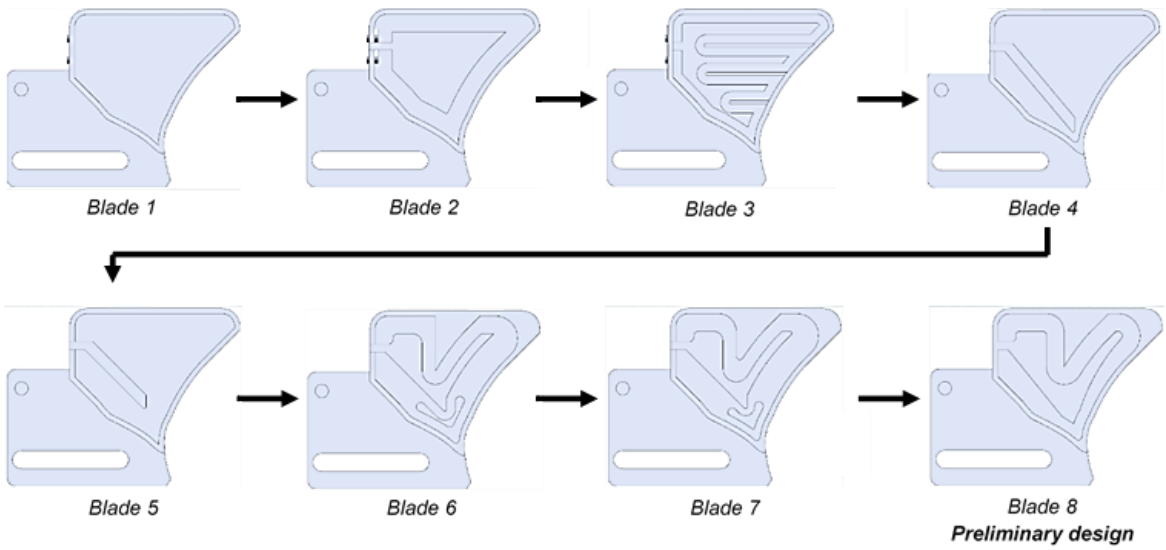

Figure 3-35 Overview of the design evolution

During the optimization study depicted in Figure 3-36, attention was always paid to three factors which influences the heat transfer. First, the heat transfer surface A_S should be as big as possible as seen in Equation 2-2. Secondly, stagnate water must be avoided at any position. When the velocity of the water flow V decreases (and therefore also the Reynolds Number Re), the convection heat transfer coefficient h will decrease. This effect is derived by the Gnielinski equation, given by Equations 3-59 and 3-60 [8]. This equation gives the Nusselt number Nu, which is the ratio of convective to conductive heat transfer, for a turbulent flow in a circular pipe. It will therefore not be used for calculations, but only used to determine the influence of a certain variable on the heat transfer. The reduced convection heat transfer coefficient h, caused by the

stagnate water, will cause an increased temperature of the blade, since less heat is dissipated to the water. This effect can be seen in Figure 3-37. Last, the temperature gradient on the blade should be as low as possible. This results in less thermal stress on the blade. Low temperature gradients can be achieved by cooling the spots which experience higher heat flux more. Material near the center of the solar reactor experiences much higher heat flux as depicted on Figure 3-34 (a). Therefore, the velocity of the water flow *V* in these places should be higher, which results in higher convection coefficient *h*.

$$Nu = \frac{\frac{f}{8}*(Re-1000)*Pr}{1+12.7*\left(\frac{f}{8}\right)^{0.5}*\left(Pr^{\frac{2}{3}}-1\right)} \quad (3\text{-}59)$$

Valid if: $0.5 \leq Pr \leq 2000$

$3 * 10^3 < Re < 5 * 10^6$

$$Nu = \frac{hL}{k} \quad (3\text{-}60)$$

f	Darcy friction factor (-)
L	Characteristic length (m)

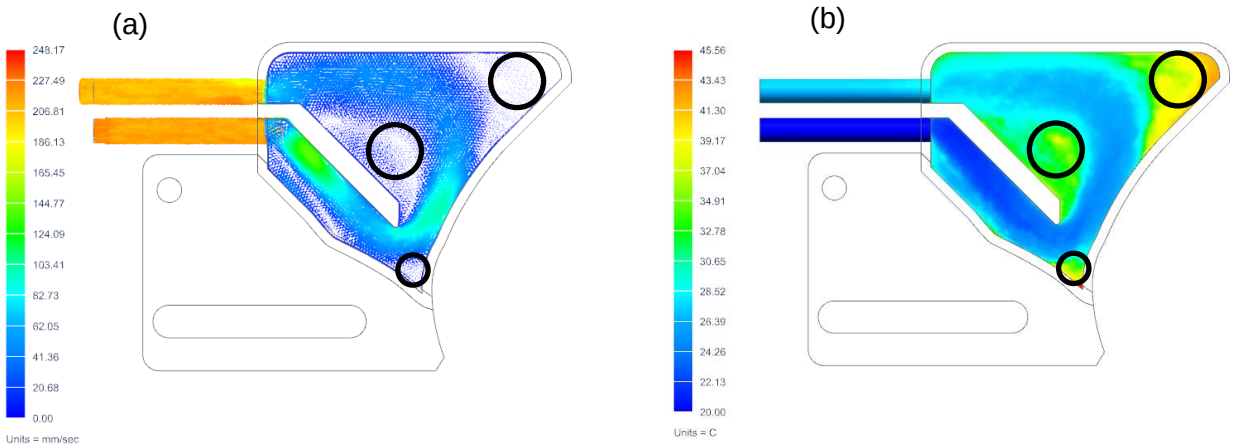

Figure 3-36 Influence of vortex: (a) Velocity of water flow, and (b) Temperature distribution of water

3.5.2.2 Parametric study

Water channel thickness

The preliminary design from Section 3.5.2.1 can be used to identify the optimal thickness for the water flow inside the blades. As mentioned in the predetermined requirements, the overall thickness should be as low as possible. Therefore, it is favourable that the thickness of the water flow is also as low as possible. The effect of the thickness of the water channel on the heat exchanging mechanism can be seen in Table 3-8 and Table 3-9. A smaller thickness results in higher Reynolds number if the water flow is constant. Consequently, the convection coefficient will increase by a decrease in thickness. This can also be concluded by using Equations 3-59 and 3-60. An increase of the convection coefficient means that the heat transfer to the water is more effective and can therefore result in a significant lower blade temperature. Nonetheless, a smaller water channel might also ensure that the outlet temperature slightly drops, due to the increased

speed of the water through the channel. Per the values from Table 3-8 and Table 3-9, it can be concluded that there is almost no difference in outlet temperature between a thickness of 2.5 mm and 5 mm. Water spends less time in the heat exchanging process when a water channel thickness of 2.5 mm is selected, but the convection coefficient increases significantly resulting in quasi the same outlet temperature as a water channel thickness of 5 mm. The outlet temperature can be increased by using water channel thickness of 10 mm. This also increases the max blade temperature significantly. Since the outlet temperature can be easily controlled by changing the water flow rate, a water channel thickness of 2.5 mm is selected resulting in smallest overall thickness of the mechanism.

The parameters used for simulations are always given with caption underneath the table with the simulation results. All of the simulations are performed with the same emissivity coefficient. This emissivity coefficient depends on the material used, surface finish and the temperature. Due to this dependence, it is impossible to find the exact emissivity coefficient in the literature for the mechanism described in this thesis. An emissivity coefficient of 0.7 is assumed, based on the fact that the blades are not polished and that it can reach temperatures of around 250 °C. [31] In thermal equilibrium the emissivity and the absorptivity coefficient are equal. This is derived from the Kirchoff's law. The first simulations are executed without taking any friction between the fluid and the material into account. This is the so-called 'smooth' parameter.

Table 3-8 Influence of the thickness of the water channel at flow rate = 0.01 L/s

	2.5 mm	*5 mm*	*10 mm*
Convection coefficient h (W/m²K)	*4783*	*1015*	*930*
Outlet temperature (°C)	*23.27*	*23.24*	*26.56*
Average blade temperature (°C)	*33.43*	*36.01*	*46.50*
Max blade temperature (°C)	*73.26*	*86.14*	*117.13*

Flow rate = 0.01 L/s; ε = 0.7; smooth

Table 3-9 Influence of the thickness of the water channel at flow rate = 0.05 L/s

	2.5 mm	*5 mm*	*10 mm*
Convection coefficient h (W/m²K)	*8463*	*2186*	*1473*
Outlet temperature (°C)	*20.69*	*20.66*	*21.32*
Average blade temperature (°C)	*28.34*	*30.75*	*38.26*
Max blade temperature (°C)	*68.10*	*77.63*	*105.18*

Flow rate = 0.05 L/s; ε = 0.7; smooth

The influence of flow rate on the outlet temperature for three simulated thicknesses is given in Figure 3-37. As depicted on this figure, the outlet temperature of the water can be easily controlled by adjusting the water flow rate. The curve shows that the outlet temperature of the water changes non-linear as function of the water flow. This is due to the non-linear relation between the convection coefficient and the Reynolds number. This relation can be derived from Equation 3-59, where the friction coefficient also changes non-linear with the Reynolds number.

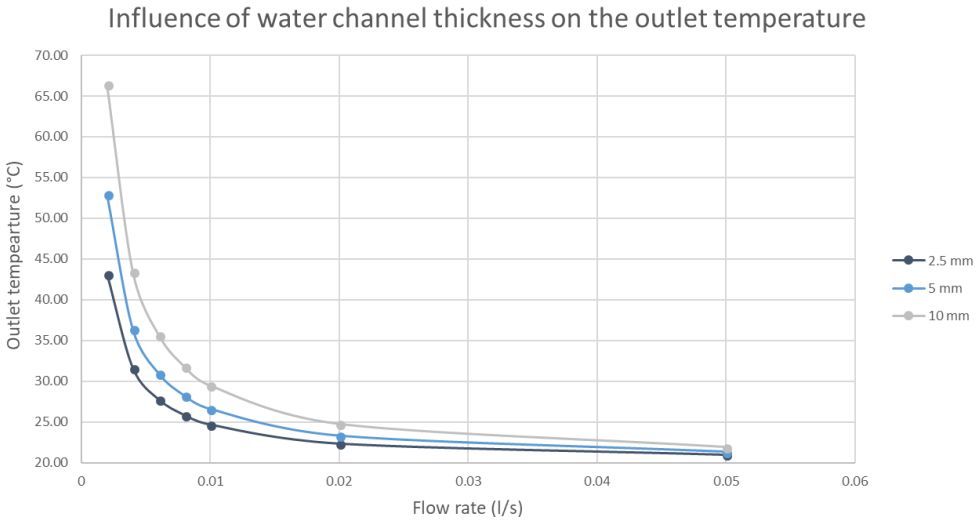

Figure 3-37 Influence of the water flow on the outlet temperature

Increasing heat transfer surface A_S

Heat transfer surface A_S can be increased by adding grooves on the bottom of the cover. A total of 12 % increase in heat transfer surface is achieved with this modification as illustrated in Figure 3-38. In Table 3-10, the influence of these grooves on the simulated parameters is given. With an increase of 27.20% on the convection coefficient *h*, the grooves are very important to achieve the best possible cooling. The grooves ensure that the blade temperature decreases, and that the outlet temperature slightly increases with 1.40%.

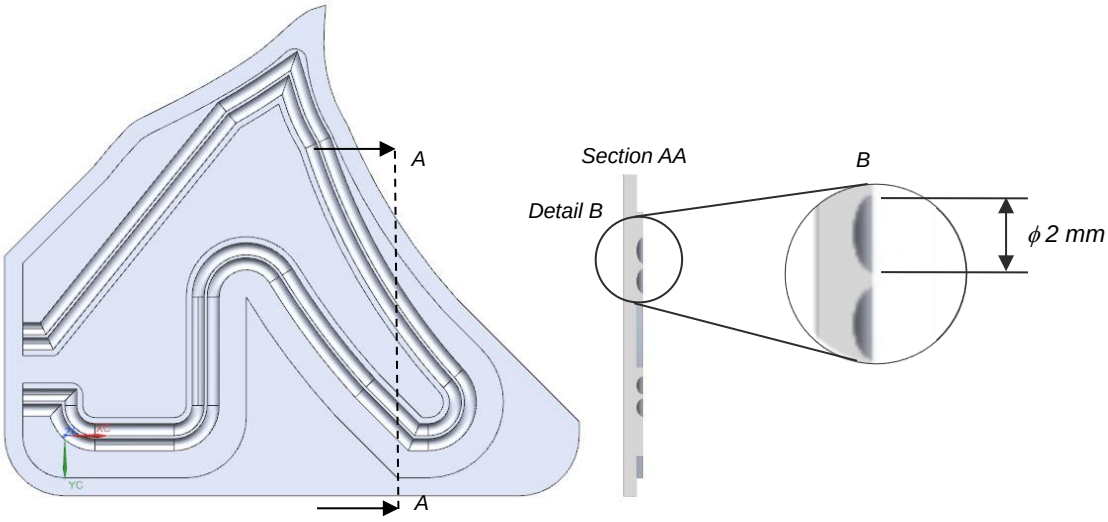

Figure 3-38 Cover with grooves

Table 3-10 Influence of grooves

	Without grooves	*With grooves*	*%Difference*
Convection coefficient h (W/m²K)	*4783*	*6084*	*+ 27.20 %*
Outlet temperature (°C)	*23.27*	*23.60*	*+ 1.40 %*
Average blade temperature (°C)	*33.43*	*31.41*	*- 6.05 %*
Max blade temperature (°C)	*73.26*	*71.66*	*- 2.00 %*

Flow rate = 0.01 l/s; ε = 0.7; thickness = 2.5 mm; smooth

Roughness

The relative roughness ε/d is related to the friction factor f. This relation is represented in a Moody chart. In general, it can be stated that if the relative roughness increases, the friction factor also increases. This has positive influence on the Nusselt number and therefore also on the convection coefficient. This effect can be explained by Equation 3-59.

The maximum roughness ε, that can be achieved in the manufacturing is only 3.2 µm. In Table 3-11 the influence of the roughness on the simulated parameters are presented. As it is seen in Table 3-11, the roughness will only have a small influence on the outlet temperature of the water. This has consequence that no post-processing of the surface would be necessary.

Table 3-11 Influence of the roughness with a flow rate of 0.01 L/s

	Smooth	3.2 µm	6.3 µm	12.5 µm
Convection coefficient h (W/m²K)	4783	4821	4874	4905
Outlet temperature (°C)	23.27	23.27	23.27	23.28
Average blade temperature (°C)	33.43	33.29	33.18	32.67
Max blade temperature (°C)	73.26	73.11	72.18	70.41

Flow rate = 0.01 L/s; ε = 0.7; thickness = 2.5 mm

3.5.3 Conclusion

Previous simulations have shown that the thickness of the water channel should be 2.5 mm. It has also shown that using grooves in the cover will significantly increase the overall transferred heat to the water. Lastly, the roughness should be around 3.2 µm and no post-processing is necessary, due to the small impact of the roughness on the outlet temperature.

In Table 3-12 and Figure 3-39, a comparison is made between a blade without the cooling and a blade with the cooling. The former has the same geometry as the one with cooling, but the inner water channels are filled with stagnate air instead of flowing water. This comparison shows that the cooling mechanism is very effective. The actual average and maximum blade temperature will depend on the selected water flow rate. If higher water temperatures are required, as it is the case for the use of a steam turbine, a lower water flow rate will be used. This also results in an inevitable higher blade temperature.

Table 3-12 Comparison between mechanism with and without cooling

	Without cooling	With cooling
Average blade temperature (°C)	520.49	33.43
Maximum blade temperature (°C)	549.23	73.26

Flow rate = 0.01 L/s; ε = 0.7; thickness = 2.5 mm; ε = 3.2µm; Water channels

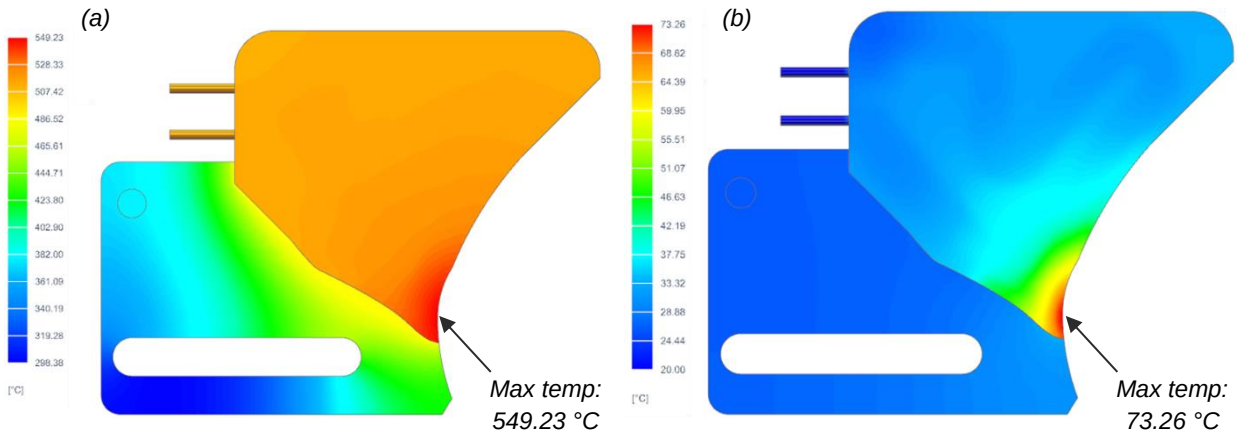

Figure 3-39 Difference in temperature distribution on the blades (a) Without cooling, and (b) With cooling

A steam turbine can be used to convert the heat and pressure of the steam to electricity. For this application, steam under high pressure is essential. Higher temperatures can be achieved if the blades are connected to each other. These connections can be seen in Figure 3-40. The slight disadvantage of this method is that the temperature distribution of every blade will be different. This temperature difference can be seen in Figure 3-41. Since 316L has low thermal expansion coefficient of only 16 µm/mK this difference will have almost no effect. Table 3-13 gives an overview of the important simulated parameters for the design with interconnected blades. To reduce the computing time, the connections are assumed to be perfect insulators.

Table 3-13 Overview with interconnected blades

	Interconnected blades
Outlet temperature (°C)	*39.48*
Average blade temperature (°C)	*56.53*
Max blade temperature (°C)	*132.02*

Interconnected blades, flow rate = 0.01 L/s, ε = 0.7; thickness = 2.5 mm; $\mathcal{E}$ = 3.2 µm

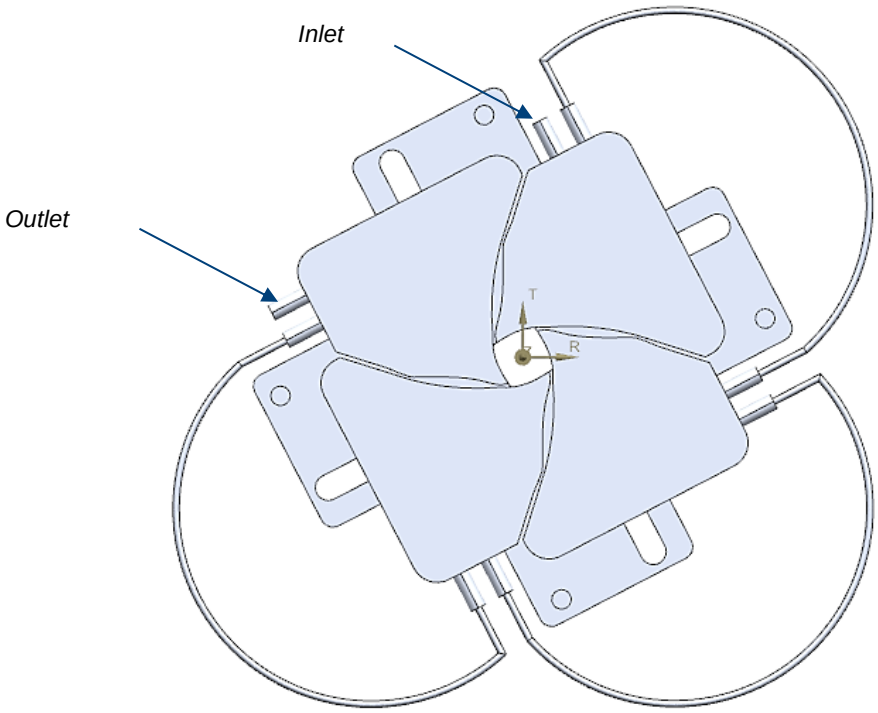

Figure 3-40 Design with interconnected blades

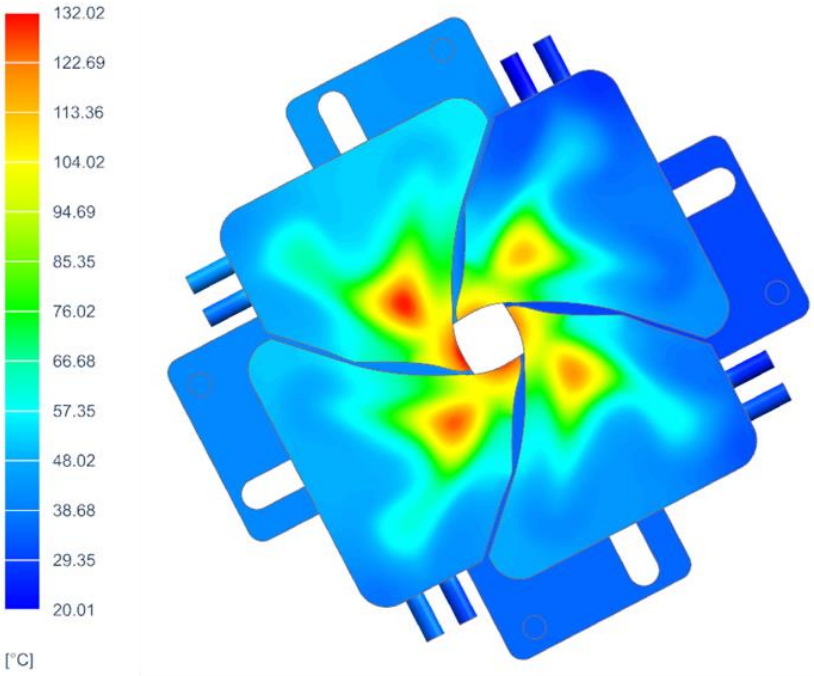

Figure 3-41 Temperature distribution with interconnected blades

As mentioned before, this thermofluidic analysis is used as an optimization tool for the design of the blades. All of the simulated values should always be validated with experiments before any conclusion can be made. Some parameters like the emissivity coefficient, inlet water temperature and the room temperature have been assumed but will have a big impact on the results. Accordingly, a difference between the simulations and the experiments is expected.

3.5.4 Thermocouples

Experiments should be performed to validate the simulations. It is necessary for these experiments that the temperature can be monitored. In order to monitor and record temperature readings, 8 bolt-on ring terminal thermocouples from Watlow with part-number: 70XKSGC048A will be used to monitor the temperature [see Appendix D]. The maximum temperature that these thermocouples can withstand is 480°C. Due to high amount of incoming radiation, the thermocouples need to be placed at the back of the blades. Otherwise the maximum temperature of the thermocouples could be exceeded. The shape of the thermocouple is milled out of the blade. This is needed to hold the thermocouples at their place and to protect the thermocouples from damage caused by friction in the movement of the blades. The milled shape can be seen in Figure 3-42.

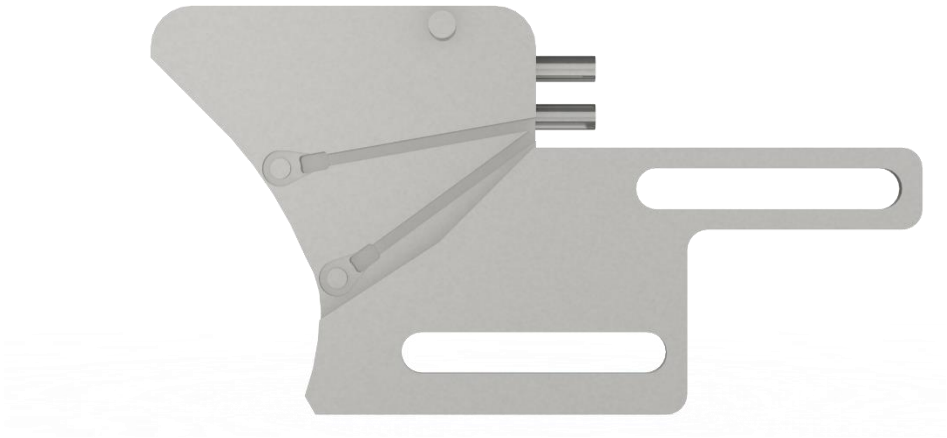

Figure 3-42 Placement of thermocouples

4 MANUFACTURING

After the fulfilment of the force and thermofluidic analysis, the mechanism is ready to be manufactured. All the necessary technical drawings are added in Appendix A. The different manufacturing processes used to produce this the designed mechanism are briefly discussed in this section.

4.1 Plasma cutting

Plasma cutting is a thermal processing technique which differs from the common mechanical processing techniques like milling by the fact that no forces acting on the material are required to obtain the desired shape. A big advantage of this is that these techniques are independent of the mechanical properties of the material. Due to the high wear and abrasion resistance of stainless steel 316L, it is favourable to use a non-mechanical processing technique. A plate of 316L with dimensions of 2000 x 1000 x 2 mm is ordered by the manufacturer 'Testas'. This plate has a thickness of 2 mm which is the desired thickness for the plasma cut parts of the mechanism. The actuator, the two plates of the attachment of the stepper motor, the small sprocket wheel and the backplate are the parts that are plasma cut. These parts are depicted in Figure 4-1. The used plasma cutter is the Swift-Cut pro 2500 which can cut through metals with a thickness up to 25 mm with a very high accuracy. This accuracy is mainly determined by the bevel in the cut face of around 4 degrees. This must always be taken into account when designing fittings in the various components [32].

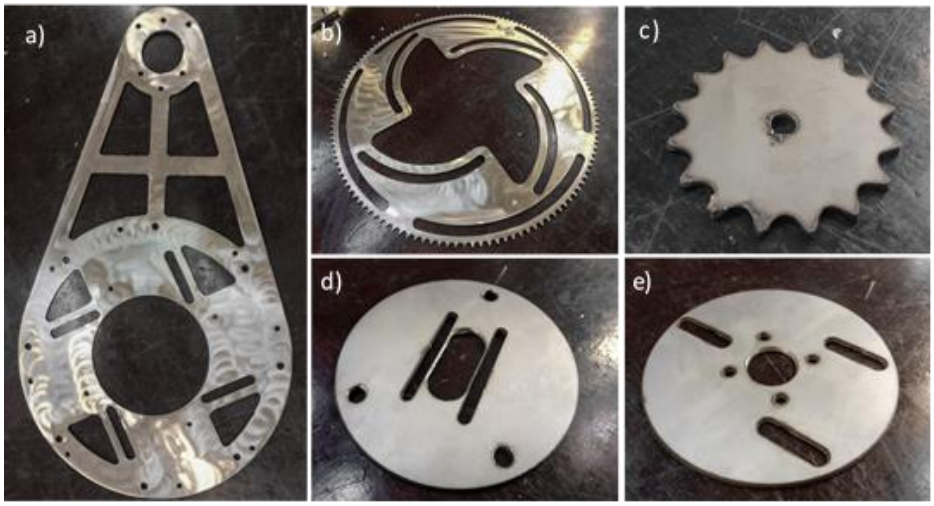

Figure 4-1 Plasma cut of (a) Backplate, (b) Actuator, (c) Small sprocket wheel, (d) Front plate small sprocket wheel, and (e) Connection motor

The inner structure of a plasma torch is depicted in Figure 4-2. When the cutting process starts, an electrical arc is formed between the tungsten electrode and the cupper nozzle. When the gas inside the torch gets in contact with this arc, it will ionize and become electrically conductive. This plasma can conduct to the workpiece which is connected with the ground, resulting in a current path from the electrode to workpiece. A shield gas is used to further constrict the plasma arc, which will lead to an even cleaner and more precise cut. The plasma jet can achieve high temperatures resulting in high cutting speeds and blowing away the molten material [32].

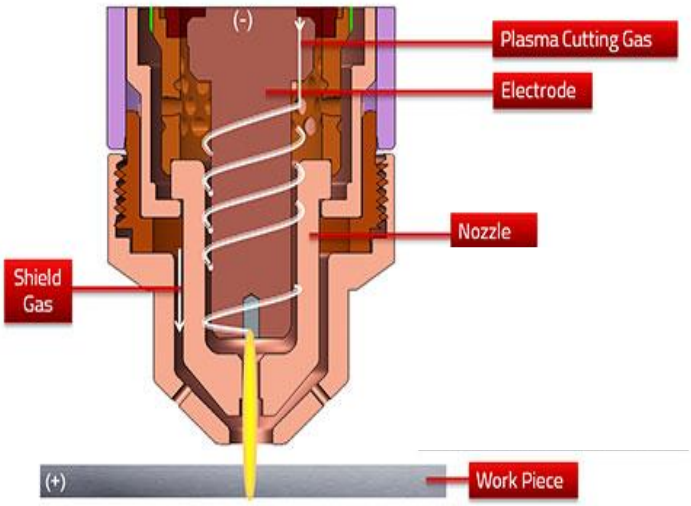

Figure 4-2 Inner structure of a plasma torch [33]

4.2 Milling

The blades and covers have a rather complex geometry with internal graved channels. The only possible way to manufacture these parts is by milling. Milling is a machining process where a rotating cutter is used to remove material from the stationary workpiece and achieve the desired geometry. A lot of problems were encountered during this process. Stainless steel 316L is an austenitic steel with excellent mechanical properties and strong corrosion resistance, but with a low machinability. This is due to the high ductility, high hardness, low heat conductivity and a high built up edge. To ensure a longer operating time of the milling cutters, high temperatures on the cutters should always be avoided. Therefore, a deep cut is favourable, reducing the friction, but a too deep cut will result in a high accumulation of the material due to the high ductility. This material accumulation will induce high tensions in the milling cutter and eventually lead to a mechanical failure. High temperatures can also be avoided by using a coolant. This is very effective for the use of regular end mills. When using roughing end mills to remove large amounts of material at once, a coolant has a negative effect on the life time of the milling cutter. The cooling itself takes place after the cutting process, resulting in a constant heating and cooling of the cutters. This temperature fluctuations could lead to thermal cracks [34]. So, the milling process is a very difficult task and all the different parameters should be selected very carefully.

The original workpiece of the blades is a plate with dimensions of 120 x 25 x 900 mm and for the covers a plate with dimensions of 100 x 8 x 750 mm is used. Both plates are ordered by STAPPERT Noxon B.V. In Figure 4-3 the milling process of the blades is given. First, the rough shape of the upper part of the blade is made, followed by the milling of the internal tubings and the back part of the blade. From Figure 4-3 (d), it can be noticed that the grooves for the thermocouples are missing. Due to the problems encountered during milling, the whole process suffered a big delay. To have adequate time for the experiments, the extra grooves are left out.

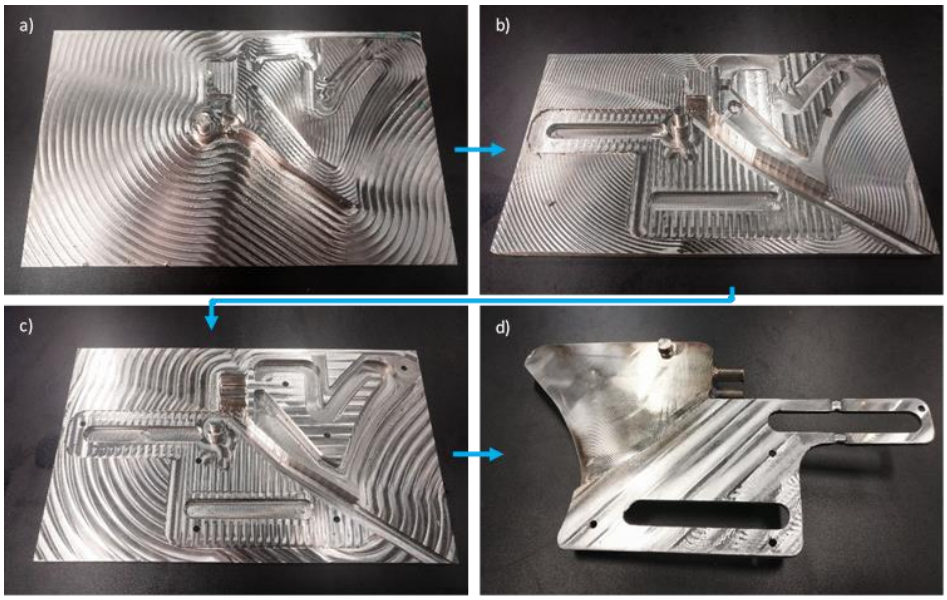

Figure 4-3 Milling process of blade: (a) Rough shape of the upper part, (b) Overall external shape, (c) With internal channels, and (d) Back part of the blade

The result of the milling process of the cover for the blades is given in Figure 4-4. After this milling process, the cover will get its final shape by a wire electrical discharge machining, which is explained in 4.3. It can also be seen in Figure 4-4 that the extra grooves in the cover, as explained in 3.5.2.2, are missing. This is for the same reason why the grooves for the thermocouples are left out as well.

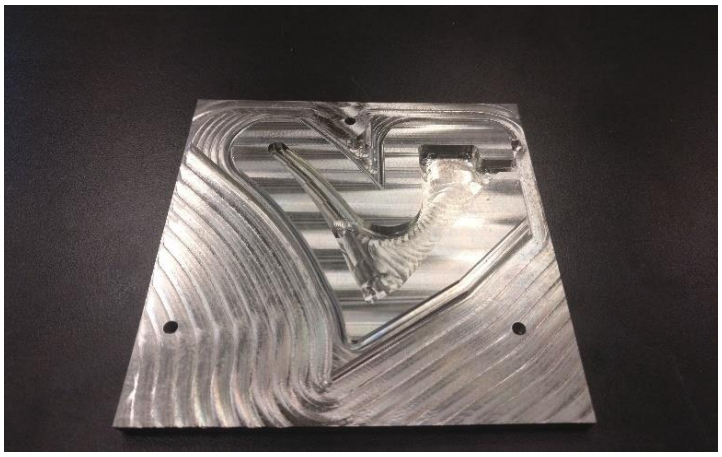

Figure 4-4 Milling process of cover

4.3 Wire electrical discharge machining

Wire electrical discharge machining or wire EDM is an electro-thermal cutting process which uses the material-abrasive function of electrical discharges, also called sparks, across the inter-electrode gap of the two electrodes: the wire and the workpiece. The overall setup for a wire EDM process is depicted in Figure 4-5. The discharge placed between the wire and the work material is a pulsating current derived from a DC power supply. The wire and workpiece are submerged in an isolating dielectrically fluid to improve the electrostatic field between the gap of the wire and the work material. Since the workpiece and the cutting tool do not touch each other, no forces are acting on acting on the workpiece. This means that workpieces of materials with low machinability can be manufactured with high accuracy and a fine surface finish [35].

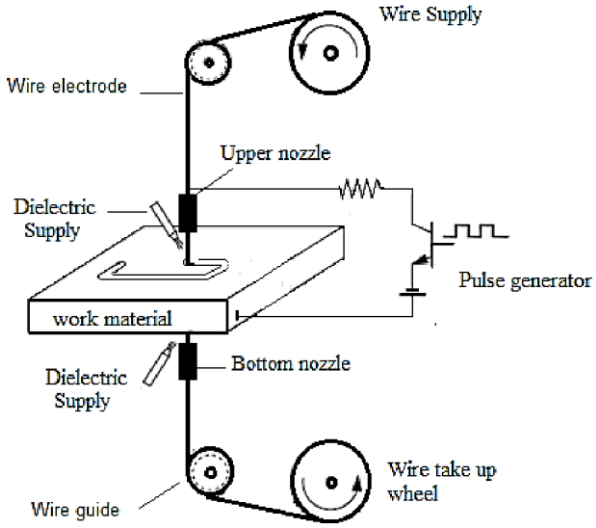

Figure 4-5 Scheme of wire electric discharge machining [35]

Wire EDM is most commonly used for intricated detailed workpieces, which are difficult to manufacture with traditional cutting methods. So, a part made of a hard material, like stainless steel 316L and where fine tolerances are needed it is preferable to use wire EDM as machining process. This process also allows the production of very small workpieces or very small holes. There is a necessity for fine tolerances on the covers for the blades, made from 316L, since they need to fit in the blade and this fitting has to be watertight after a welding process. For this reason, wire EDM is the preferred machining process. The structures of the covers are first milled. This process is followed by wire EDM to achieve the final shape. This final shape can be seen in Figure 4-6.

Figure 4-6 Final shape of the cover

4.4 Turning

Turning is a machining process were a stationary cutter is used remove material from a rotating workpiece. In general, rather simple and rotational symmetrical shapes are obtained by this method like cylinders, cones, etc. The rings for the sprocket wheel and the rings for the blades are manufactured with this process. These parts together with the original workpiece are depicted in Figure 4-7. The original workpiece is a cylinder of 316L with a length of 180 mm and a diameter of 25 mm.

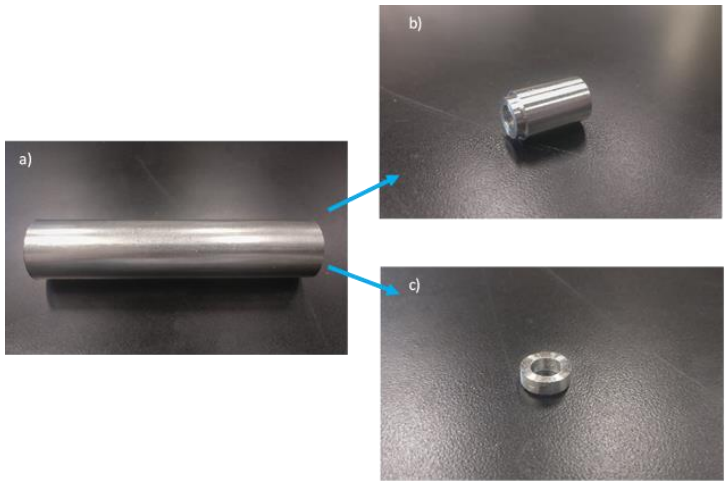

Figure 4-7 (a) Original workpiece for the turning process, (b) The ring for the sprocket wheel, and (c) The ring for the blades

4.5 Threaded rods

The threaded rods, welded on the backplate, need to be cut at the desired length of 13 mm and 28 mm. The cutting method is depicted in Figure 4-8. A total of 5 nuts are mounted on the rod. This has a dual purpose. On the one hand it ensures that the cut is precisely made at the desired length and on the other hand it ensures that the thread is not damaged. Moreover, releasing the nut from the cut rod will restore any deformation in the thread.

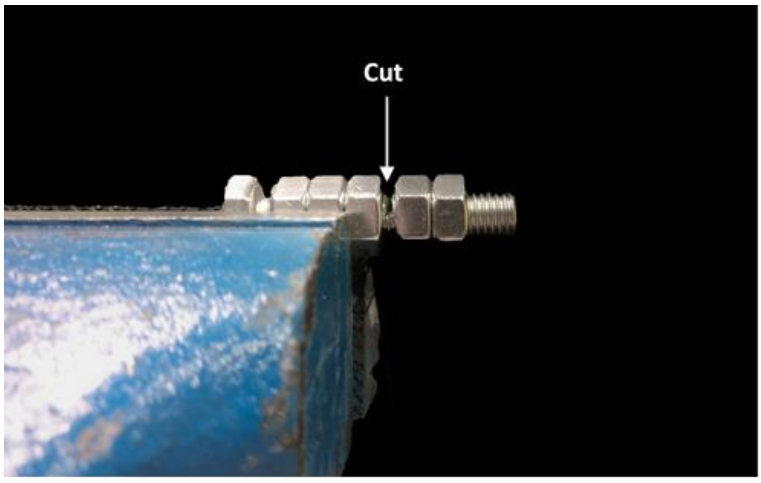

Figure 4-8 Threaded rot cutting method

4.6 Welding

The technical drawings for the welding process can be found in Appendix A. The used welding process is gas tungsten arc welding also known as tungsten inert gas welding (TIG-welding). With this welding process, an electrical arc is formed between the non-consumable tungsten electrode and the workpiece. This arc provides high temperatures which are necessary to join the metals together. If necessary additive material can be added manually. The used shielding gas is an inert gas which protects the weld from oxidation and other contaminations. This welding process is especially suitable for welding small, thin parts as is the case for the necessary welds of the iris mechanism.

Figure 4-9 depicts the final design of the blade. This final design is the joining by welding of the cover as depicted on Figure 4-6 and the blade as depicted on Figure 4-3.

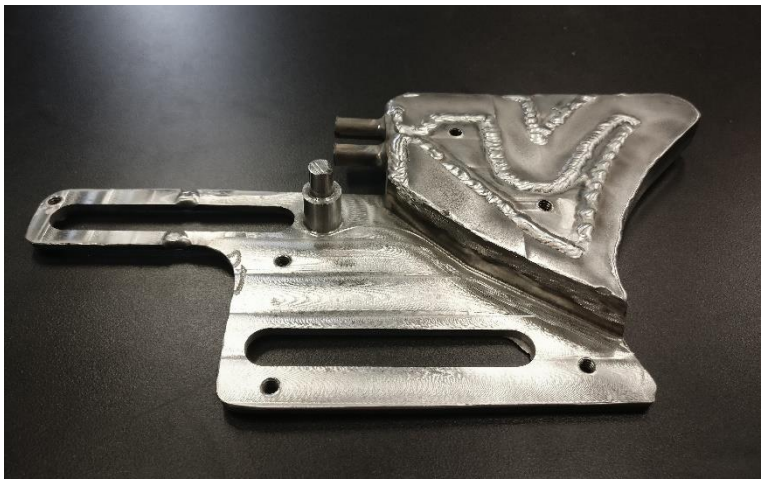

Figure 4-9 Welded blade

Figure 4-10 depicts the backplate with all its welded parts. These welded parts consist of four slots and a total of 12 threaded rods. The slots are made with a milling process and the threaded rods are manufactured as described in Section 4.5 Threaded rods.

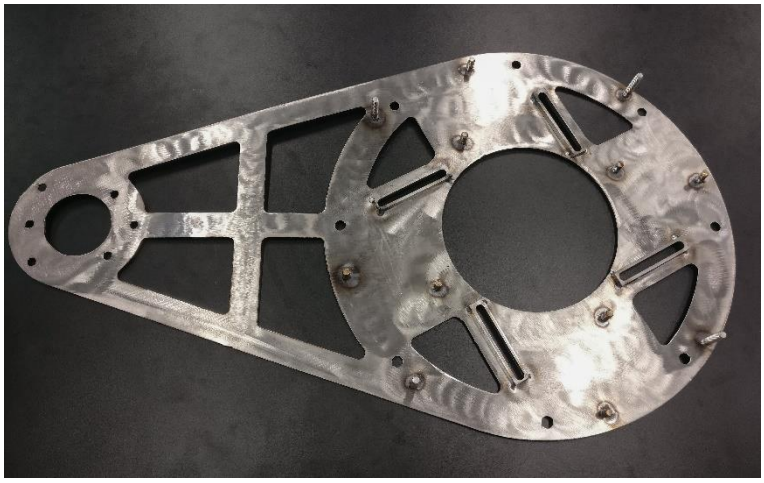

Figure 4-10 Welded backplate

5 EXPERIMENTS

The performance of the iris mechanism will be tested in this section. The following three experiments will be executed on the mechanism:

- Aperture surface area as function of rotation of the stepper motor
- Thermal measurements to examine the influence of the flow rate
- Thermal measurements to examine the influence of the aperture

Using the data resulting from these experiments, conclusions and potential future work will be determined.

5.1 Aperture surface area measurements

The first experiment that will be executed is the determination of the aperture surface area as function of the rotation of the stepper motor. The main goal of this measurement is to verify if the aperture area meets the calculated area from Section 3.4.1.

Figure 5-1 is a picture taken of the experimental setup. A CMOS-camera is aligned with the optical axis of the iris mechanism. The used CMOS-camera is a BC-X104 from the German company Matrix Vision. The datasheet is added in Appendix F. A diffuse light source, positioned behind the iris mechanism, is used to show the contour of the aperture. The camera is connected to a computer where the Matlab® image processing module will be used. The overall principle of this measurement is that a picture will be taken for every 50 degrees of rotation of the stepper motor. A black pixel in this picture corresponds to the iris mechanism and a white pixel to the opening. Matlab® will be used to calculate the number of white pixels in one picture. If the camera is correctly calibrated, the number of white pixels corresponding to 1 mm² is known so that the aperture surface area can be calculated.

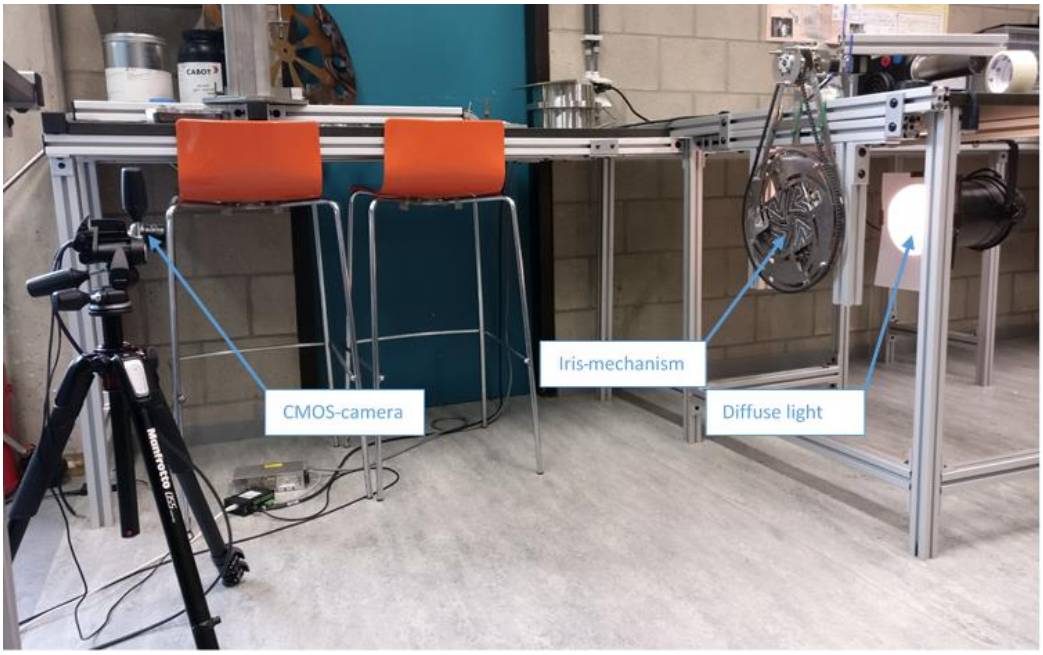

Figure 5-1 Experimental setup of the aperture surface area measurements

5.1.1 Calibration of the CMOS-camera

The camera must first be calibrated before any experiment can be executed. This calibration consists of determining the number of pixels per square mm. For this, a white paper with a 50x50 mm black square is printed and placed at the position of the iris mechanism. The experimental setup for this calibration process is depicted on Figure 5-2. After capturing a picture with the CMOS-camera, the number of black pixels contained in this picture is measured using the Matlab® software. The results show that 25 mm² contains 107606 pixels. From this, it can be identified that the pixel density is 43.042 pixels/mm².

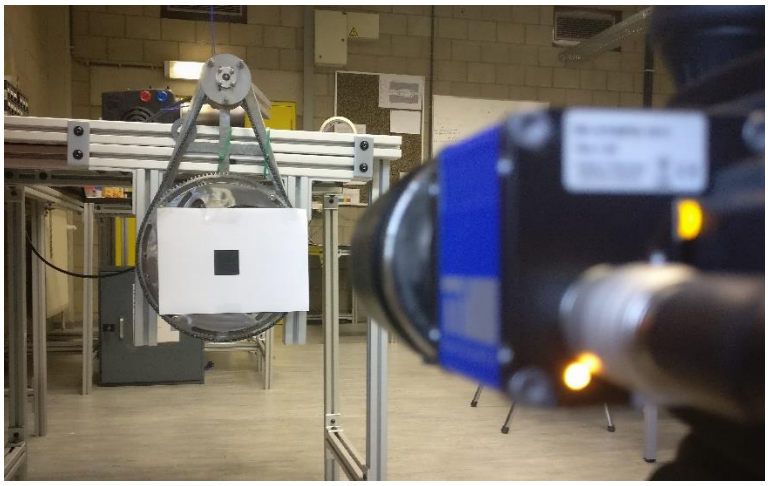

Figure 5-2 setup for calibration of the CMOS-camera

5.1.2 Image processing

The images captured with the CMOS-camera which can be seen in Figure 5-3, are imported in Matlab® as a grayscale bitmap. This format represents every pixel as a value in a two-dimensional array. The value of one pixel is always between 0 and 255 where 0 is a black pixel (no illumination) and 255 is a white pixel. To achieve a greater contrast in the picture a f-number, which is the ratio of the camera's focal length to the diameter of the camera's aperture, of 1.4 and a low exposure time of 290 µs is selected. This higher contrast results in less average values of 127.

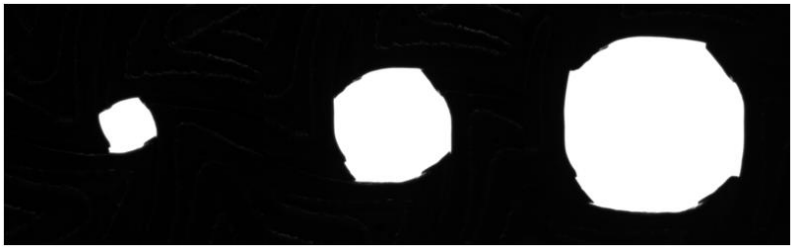

Figure 5-3 Captured images CMOS-camera (motor angles: 0°; 150°; 300°)

The number of pixels in the aperture surface can be calculated by measuring the number of cells in the bitmap with a value above 100. Once this number is known, the actual area can be calculated by dividing this number by 43.042 pixels/mm². The function established in Matlab® to calculate this aperture area is given below.

Matlab® function to determine the aperture surface area:

```
function area = surf_area(photo)      %Initialize function (input = photo and output = area)
z = 43.0424;                          %Pixel density (pixels/mm²)
B = imread(photo);                    %Insert bitmap-photo as a matrix
A = find(B>100);                      %Find all cells in matrix B with a value above 100
number = length(A);                   %Calculate the found number of cells
area = number/z                       %Convert calculated number of cells to area (mm²)
```

5.1.3 Results and discussion

The comparison between the results based on the different methods of calculating the aperture surface area as described in Section 3.4.1 and the measured aperture surface area during this experiment is represented by a graph in Figure 5-4. The column chart represents the absolute percentage error of the established Equation 3-17, the circular area and the CAD measurements relative to the experimental data. A difference between the experimental data and the established equation and the circular area was expected since there is also a difference with the CAD measurements as depicted on Figure 3-13. The difference between the CAD measurements and the actual measured areas is probably due to a non-perfect CAD measurement and due to slight differences in the curve and/or position of the blades.

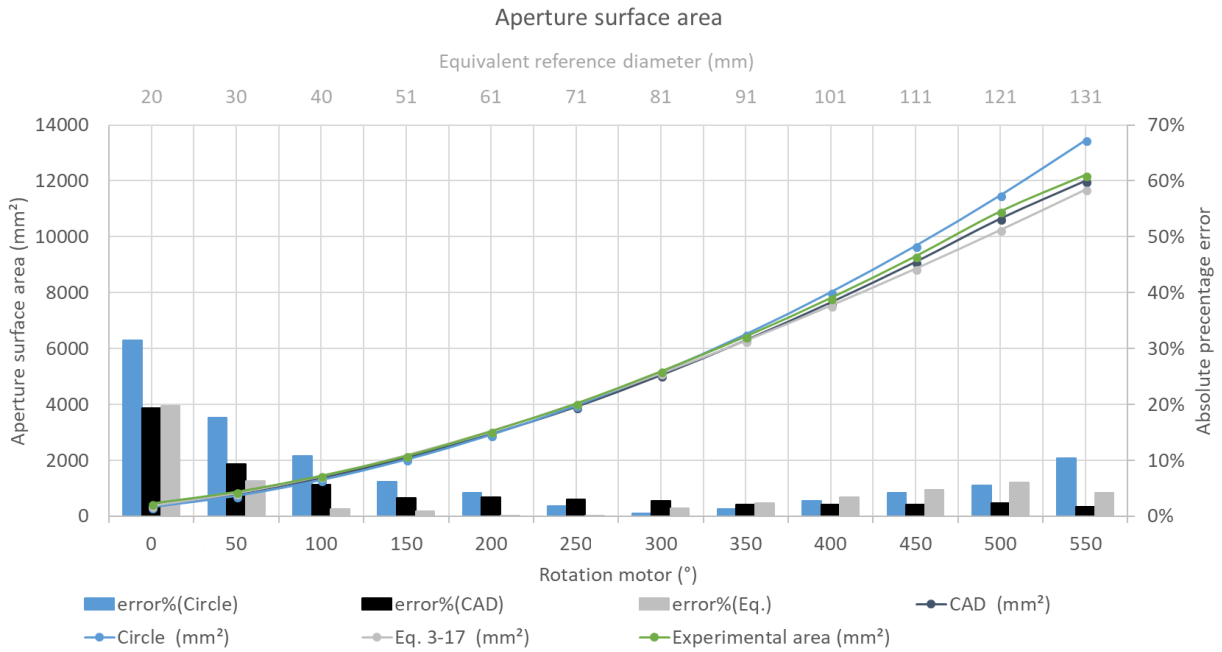

Figure 5-4 Comparison between the different methods of calculating and measuring the aperture surface area

If one wants to regulate the amount of flux going through the aperture, the aperture surface area as function of the rotation of the motor should be known. Equation 5-1 represents this relation as a second order polynomial based on the experimental values. This approximation has a coefficient of determination of 0.9993, so the area can be calculated with a high accuracy.

$$A = 0.0235 * \theta_{motor}^2 + 9.0211 * \theta_{motor} + 354.1 \qquad (5\text{-}1)$$

5.2 Thermal experiments

The second experiment that is executed is a measurement of the in- and outlet temperature of the water. The main purpose of the use of an iris mechanism is to achieve a constant temperature inside the reactor even if incoming radiation variates due to the transient nature of solar radiation. Therefore, the temperature of the gas inside the reactor and the wall temperature of the reactor are also monitored during these experiments. The results gathered with this experiment can also be used to validate the results from the CFD simulations from Section 3.5. As discussed before, water inside the blades should be pressurized to recover energy with the use of a steam turbine. How this pressurized water is established together with all the connections of the necessary measuring devices is discussed in next Section 5.2.1.

5.2.1 Experimental setup

The overall experimental setup is given in Figure 5-5. The setup consists of three main components: (1) the solar simulator, (2) the designed iris mechanism and (3) the solar reactor. The solar simulator has three power levels: (1) early morning with an input current of 115 A, (2) morning at an input current of 135 A and (3) noon with an input current of 155 A. The highest intensity of 155 A is selected for this experiment. The feedstock in the reactor is air with a flow rate of 10 normal L/min. All the measurements are executed when the wall temperature and the temperature of the feedstock inside the gas are at steady state. Steady state is assumed when the percentage temperature difference of the temperature of the wall during a time frame of 15 minutes is less than 1%.

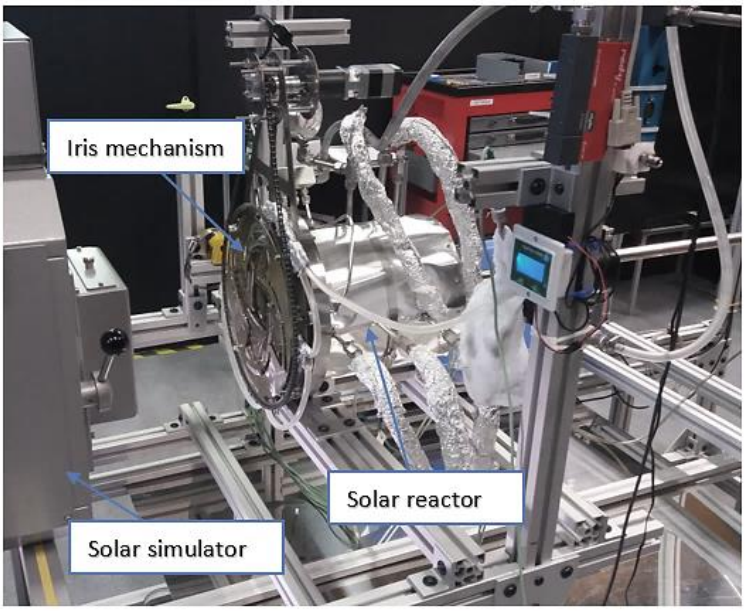

Figure 5-5 Overall experimental setup thermal experiments

The hydraulic setup of the iris mechanism is shown in Figure 5-6. The flow of the water will be measured with a flow meter, DigiFlow 6710M-32TM. A concise datasheet of this flow meter is added in Appendix G. It can be deduced from the CFD-simulations that a low flow rate is necessary to achieve high water temperatures. The selected flow meter can measure the water flow rate down to 0.003 L/s with an accuracy of 5%. A total of two thermocouples is used to measure the in- and outlet temperature of the water. These thermocouples are the ones that are already available in the lab, Omega 12KIN-1/8-U-6-D. The datasheet of this thermocouple is

added in Appendix H. The last measuring device that is used is a manometer to measure the water pressure. The one used in the setup is a manometer from the Mega Group which has a range of 0 to 6 bars with an accuracy of 1.6%.

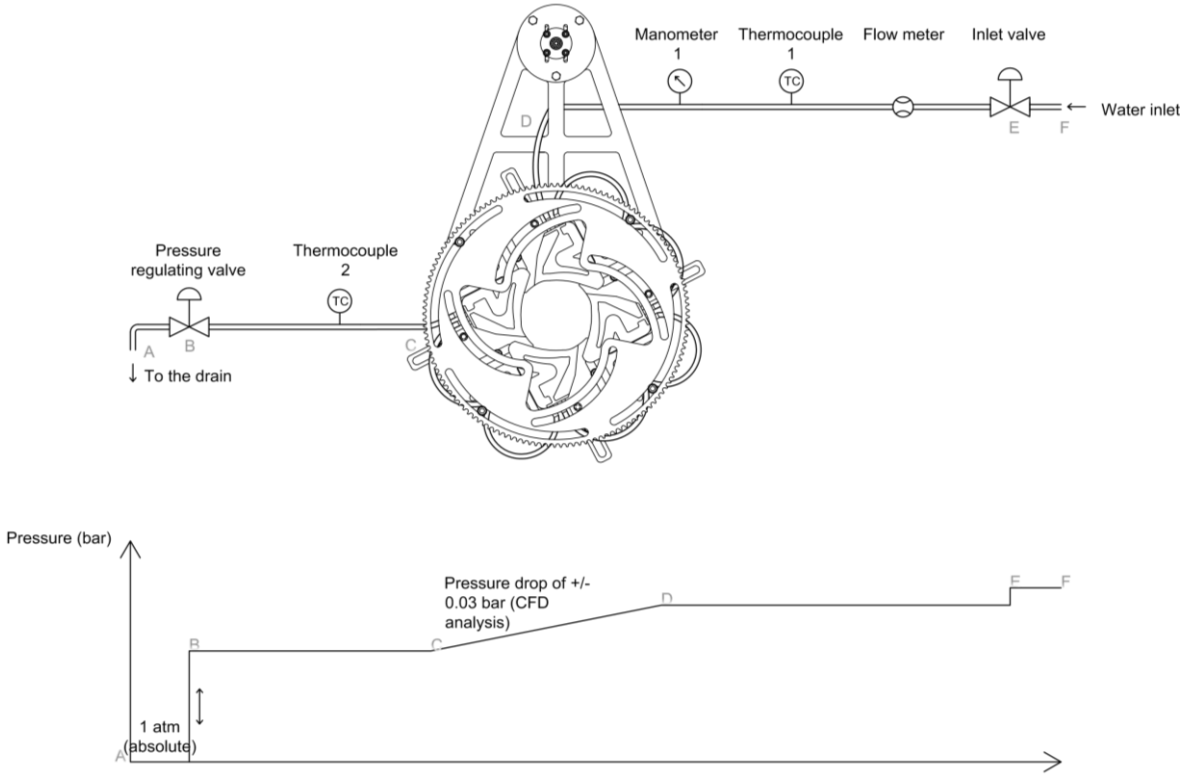

Figure 5-6 Hydraulic setup of the thermal experiments

To achieve the necessary pressurized water, a water pump could be used. Such a pump usually works at higher flow rates and are very expensive. Another rather simple but very effective method is used. A pressure regulating valve is used to control the pressure inside the iris mechanism. At the left side of this valve in Figure 5-6, there will be 1 atmospheric (absolute) pressure and on the right side a maximum pressure which is equal to the maximum pressure inside the water pipes connected to the tap. This maximum pressure is around 2.5 bar and can slightly differ throughout the day, depending on the water usage in the neighbourhood. The pressure variation as function of the position inside the setup is also given in Figure 5-6. From the CFD-analysis a pressure drop of 0.03 bar can be expected inside the iris mechanism.

It was quite a challenge to assemble the connections between the tubes and the blades watertight. Especially since these connections must withstand a pressure of up to 2.5 bar. The connections on the blade were not as circular as expected. These connections had also some sharp membranes, as can be seen in Figure 5-7, which needed to be polished off. After making the connections as circular as possible, Teflon is added to achieve a total watertight connection even under high pressure. Another problem, encountered during the setup, is that in one blade the drilled hole inside the connection for the tubes on the blades was not perfectly centred and the drill itself was not deep enough. This results in a very small gap for the water to pass from the connection to the water channel inside the blade. This has a large pressure drop as consequence and the maximum achieved flow rate significantly decreases.

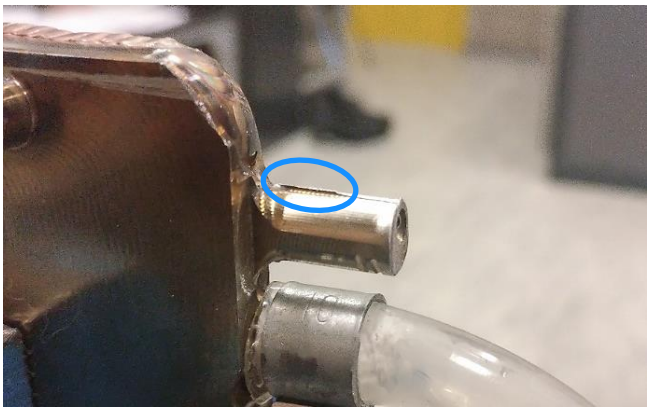

Figure 5-7 Sharp membrane at the connection for the water tubes

The first experiments, described in 5.2.2, are executed with a setup as depicted on Figure 5-5. The used tubes to guide the water have a maximum operating temperature of 175 °C. This is high enough to withstand the high temperature of the water and the incident radiation. Since the mechanism is made as thin as possible, the tubes might touch the backplate, bolts or other metal parts. The temperature of these metal parts can be far above 175 °C, due to the radiation of the simulator and conduction from the reactor. After a continuous runtime of 6h and 50 min, the tubes started leaking at two different position, so the experiment had to be terminated. After a thorough investigation it could be concluded that the tubes showed a small cut at the position where the tubes touched the bolts, which are used to mount the mechanism on the reactor. Due to the problems encountered during manufacturing, the remaining timeframe was rather short. A quick but effective solution had to be found to this problem. Aluminum foil is used to prevent a direct contact from hot metal parts to the tubes. This foil has a high reflectivity of around 0.90 which is preferred since this will result in less temperature increase by radiation [36]. Aluminum has a high conductivity of around 237 W/mK, which is not ideally since the heat from hot metal parts can conduct to the tubes. However, a study done by MIT [37] has shown that the thermal conductivity of Aluminum foil is very low and it depends on the thickness and the way it is used. If a foil of thickness 25.4 µm is crumbled with a total of 5 layers and a total thickness of 2.54 mm, the thermal conductivity is only 0.054 W/mK [37]. If more time was available, a better insulation method and material should have been used. A better suggestion will be discussed in section 6. The position of the iris mechanism is also changed after the encountered problems. The distance from the reactor to the backplate is changed from 2.5 mm to 15 mm by the use of spacers, as can be seen in Figure 5-8. This deteriorates the heat transfer from the reactor to the iris mechanism, but it will also change how the flux incidents on the blades.

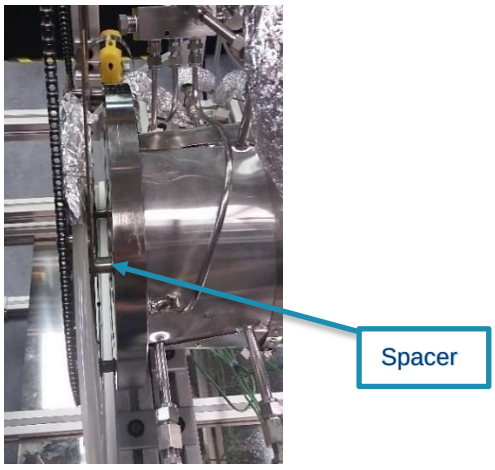

Figure 5-8 Repositioning of the iris mechanism

5.2.2 Influence of the flow rate

The first experiment executed on the solar simulator and solar reactor is to determine the influence of the flow rate of water inside the blades on the amount of power absorbed by the blade. The intention was to do this for at least 4 apertures (20 mm, 40 mm, 80 mm and 120 mm). Due to the leakage in the tubes as described in section 5.2.1 and the time pressure derived from the time delay during the manufacturing, only the experiment for an aperture of 120 mm was executed. Four different flow rates through the blades were set variating between 0.06 L/min and 0.68 L/min. For each flow rate, the ingoing water temperature T_{in}, the outgoing water temperature T_{out} and the ingoing pressure are measured. Using Equation 3-58 ($\dot{Q} = \dot{m} C_p \Delta T$), the power recovered by the water can be calculated as seen in Table 5-1. The density and the heat capacity are considered to be at a constant value of respectively 998.2 kg/m³ and 4187 W/mK, which are the water characteristics at 20 °C and atmospheric pressure. This is a valid approximation since both parameters don't show a significant change at the achieved temperature and pressure during this experiment. All the measurements are executed when the wall temperature and the temperature of the feedstock gas inside the reactor are at steady state. Steady state is assumed when the percentage temperature difference of the temperature of the wall during a time frame of 15 minutes is less than 1%.

Table 5-1 Results experiment influence of the flow rate

Flow rate (L/min)	T_{in} (°C)	T_{out} (°C)	ΔT (°C)	Pressure (bar)	Power recovered (W)
0,07	22,02	48,23	26,21	2,1	121,7
0,15	20,77	35,31	14,54	1,8	151,9
0,21	20,54	31,70	11,16	1,9	160,8
0,34	20,09	26,93	6,84	0,6	162,0
0,68	19,55	22,81	3,26	2,3	154,9

Figure 5-9 depicts a graphical representation of the temperature difference between the in- and outlet of the water flow as function of the flow rate through the blades. The temperature difference increases when the water flow decreases. This is also what is expected since water spent more time in the blades, which functions as a heat exchanger. The thermofluidic analysis, as described in 3.5, has only been executed for an aperture with a diameter of 20 mm. Since the results for this aperture diameter are missing in this experiment, no comparison can be made.

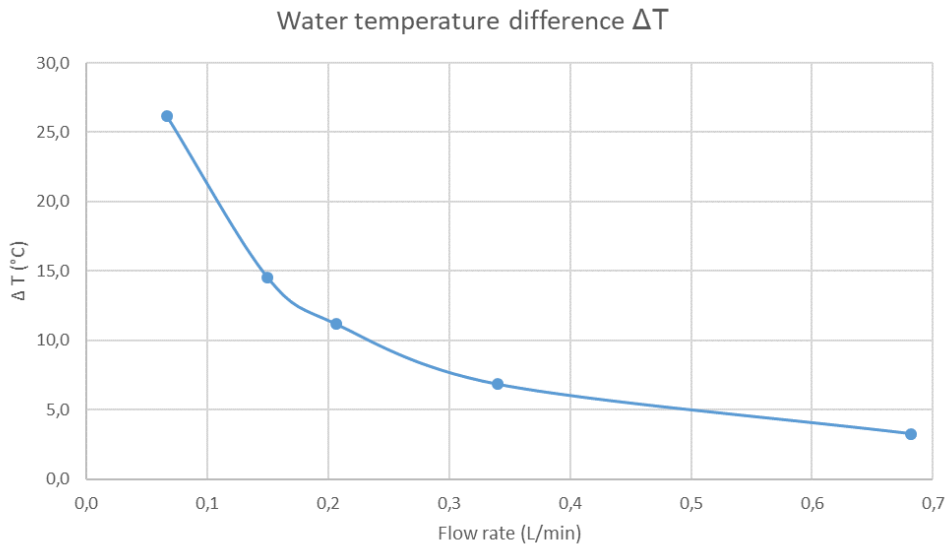

Figure 5-9 Temperature difference between the in- and outlet of the water flow

Figure 5-10 represents the power absorbed by the water going through the water channel of the blades for an aperture with a reference diameter of 120 mm. The results of Section 3.5 are calculated for an aperture of 20 mm so no comparison can be made. If more time would have been available for the experimental testing, this experiment would also have been executed for an aperture of 20 mm. Figure 5-10 clearly shows that an increase in flow rate will lead to more absorbed power by the water. The heat exchanger of the blades works better when higher flow rates are achieved. This was already concluded in section 3.5.2.2, where the Gnielinski equation, given by Equations 3-59 and 3-60, was used to make the same conclusion. A higher flow rate results in a higher Reynolds number which has an increase in convection coefficient as consequence. A higher convection coefficient means a better heat exchange mechanism. A drop in the amount of absorbed power can be noticed when increasing the flow rate above 0.34 L/min. To make a scientific conclusion from this phenomenon, more tests should be executed. This drop could possibly be the result of the transition from laminar to turbulent flow. The power absorbed by the water inside the blades will be compared with the amount of power striking the blades in the next experiment.

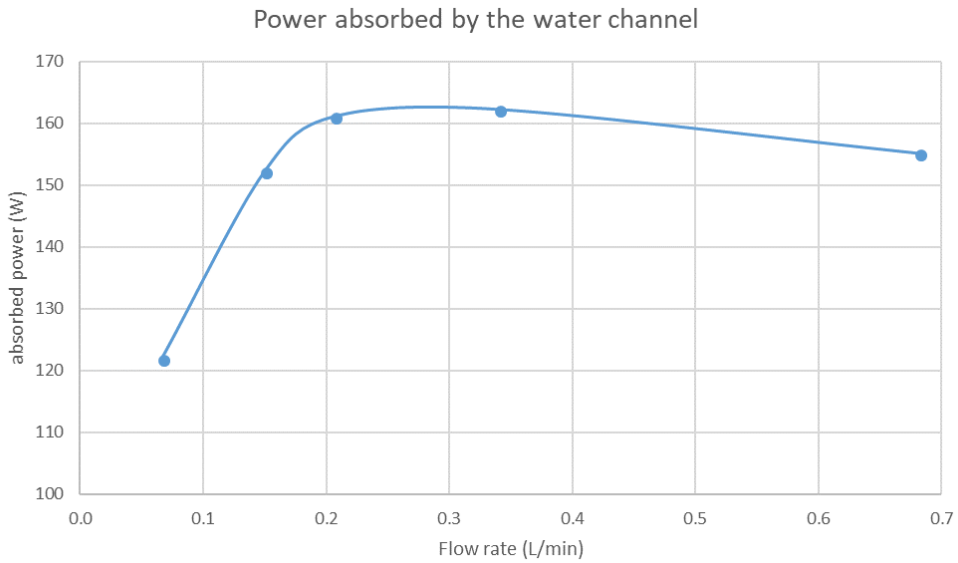

Figure 5-10 Power absorbed by the water channels of the blades

5.2.3 Influence of the aperture

In this experiment, the influence of the aperture on the reactor wall temperature T_{Wall} and gas temperature T_{Gas} inside the reactor are measured for four different apertures (20 mm; 40 mm; 80 mm and 120 mm). Also, the ingoing water temperature T_{in}, the outgoing water temperature T_{out} and the ingoing pressure are monitored for each aperture. A fixed flow rate of around 0.38 L/min is set for water going through the blades. Using Equation 3-46 ($\dot{Q} = \dot{m}C_p\Delta T$), the power recovered by the water can be calculated as seen in Table 5-2. The density and the heat capacity are again considered to be at a constant value of respectively 998.2 kg/m³ and 4187 W/mK, the same conditions as the experiment above. All the parameters of interest are measured three times for each considered aperture. Average values of these experiments are given in Table 5-2. All the measurements are executed when the wall temperature and the temperature of the feedstock gas inside the reactor are at steady state. Steady state is assumed when the percentage temperature difference of the wall temperature during a time frame of 15 minutes is less than 1%.

During this experiment the iris mechanism was placed at a larger distance of 15 mm from the reactor flange. This has already been discussed in detail in Section 5.2.1. This modification has two consequences. On the one hand it deteriorates the heat transfer from the reactor to the iris mechanism and on the other hand it changes the heat flux distribution that strikes the blades.

Table 5-2 Results experiment influence of the aperture

Aperture (mm)	T_{wall} (°C)	T_{gas}(°C)	Flow rate (L/min)	Flow rate V (L/s)	ΔT (°C)	Q (W)
120	439,82	374,15	0,361	0,006	4,48	112,8
80	427,24	362,15	0,377	0,006	6,93	181,7
40	360,68	304,68	0,397	0,007	10,85	299,7
20	248.24	205.26	0,395	0,007	14,94	410,8

Figure 5-11 gives the average temperature of the wall and gas inside the solar reactor as function of the reference diameter of the aperture. This graphical representation again shows that the use of a variable aperture mechanism is very effective in controlling the temperature inside the reactor. The gaussian's distribution of the heat flux makes the reactor temperature more sensitive to aperture changes in the region of small aperture reference diameters. When the iris mechanism's aperture closes, the temperature inside the solar reactor decreases due to the fact that a lower amount of power is going in the reactor. This amount of power is blocked by the blades and in contrast to previous designed mechanism, as discussed in the literature study in Section 2, a certain amount of this blocked radiation can be recovered by heating up the water flow inside the blades. The graph from Figure 5-11 can be used for future research on the solar reactor when using the designed iris mechanism.

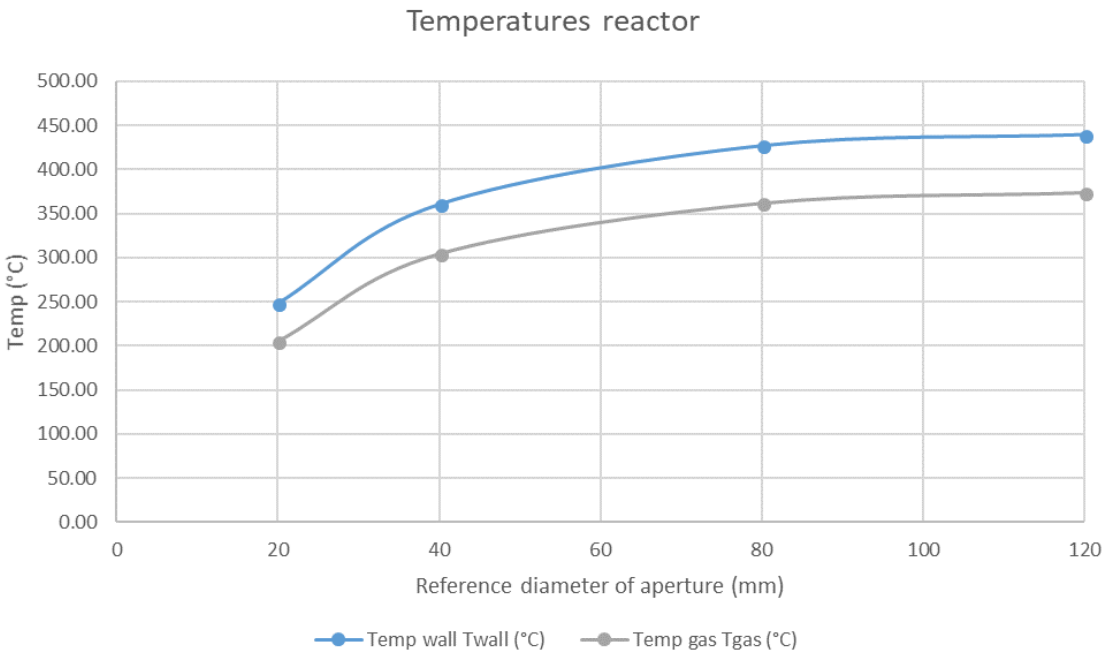

Figure 5-11 Temperatures inside of the reactor for each aperture

Figure 5-12 gives a comparison between the amount of blocked power, power absorbed by blades and power absorbed by water. The blocked power is obtained by the calculations in Section 3.4.4. The amount of power absorbed by the blades is the result of the simulations in TracePro®, which is described in Section 3.4.3 and the power absorbed by water are resulting from the executed experiments.

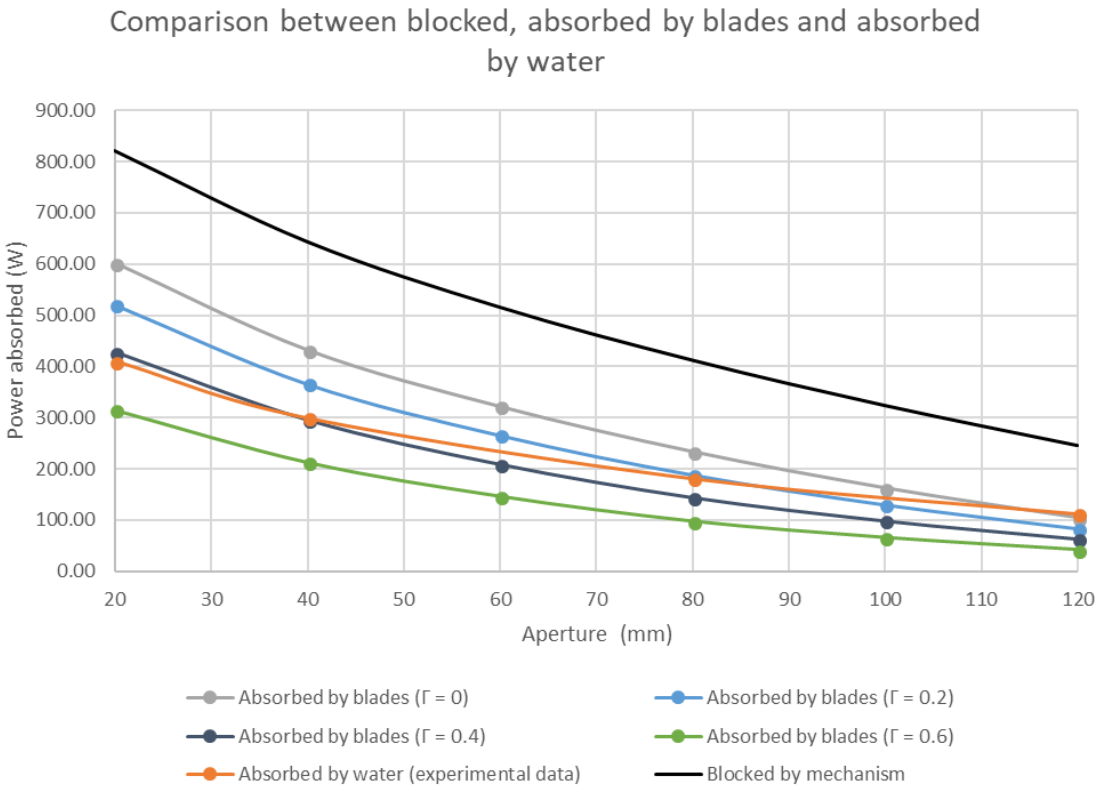

Figure 5-12 Comparison between the blocked power, power absorbed by blades and power absorbed by water

The orange line in Figure 5-12 represents the amount of recovered power by the build-in heat exchanger. It can be concluded from this figure that a great amount of power is recovered by the designed mechanism during this thesis. The amount of power absorbed by water is not parallel to one of the calculated amount of power absorbed by the blades. Moreover, even at an aperture with a reference diameter of 120 mm the amount of recovered power is higher compared to the calculated amount of absorbed power by the blades. This can be explained by two reasons. First, since the iris mechanism had to be repositioned to 15 mm from the reactor flange, the heat flux distribution striking the blades differ from the heat flux distribution used in the optical analysis. Secondly, the build-in heat exchanger can also absorb power by heat conduction from other parts at elevated temperatures like the backplate, actuator, etc. Only the radiation is considered during the optical analysis.

From the thermofluidic analysis a water temperature difference of 19.34 °C is expected with a flow rate of 0.01 L/S and an aperture with a reference diameter of 20 mm. This corresponds to a power of 814.2 W. When comparing this value to the experimental value of 410.8 W, achieved with a flow rate of 0.007 L/s, it can be concluded that the CFD simulations are a very useful tool for an optimization study, but when one wants to identify the amount of recovered power, he should rely on the experimental values. It should also be mentioned that the geometry of the blade has slightly changed compared to the CAD-model used in the CFD simulations. The extra grooves, which would have resulted in a 12% increase in heat transfer surface are not included in the actual blade design. During the simulations, some approximations have been used. For example, the tubes to guide the water from one blade to another are considered to be perfect insulators.

6 CONCLUSION AND FUTURE WORK

This thesis describes the design process, manufacturing and experimental testing of a novel iris mechanism with built-in heat exchanger. The new design needs to meet some predetermined requirements which are seen in Figure 6-1. A force analysis is done to identify the stepper motor. This selection is based on a correlation between the rotation of the motor and the torque delivered by this motor. The force analysis also led to an improved design where less torque is needed to translate the blades and a more stable motion is established. The correlation of the aperture surface area as a function of the rotation of the stepper motor is derived based on a geometric approximation. This relation also shows that the actual aperture is always close to an aperture with a circular shape. The unique feature of this design over previous designs is that with an overall thickness of 25 mm a very thin design with an energy recovery system is made while still achieving a circular aperture.

A set of CFD simulations are executed using the software Siemens NX [23] to optimize the internal structure of the blades. This optimization study led to a better understanding of the influence of certain parameters on the outlet temperature and maximum temperature of the material. Using the results of the heat flux map experiments performed by C. Ophoff, a relation between the amount of blocked energy as a function of the opening of the aperture is drafted.

- ✓ *Cooled blades*
- ✓ *Circular aperture*
- ✓ *Minimum 20 mm opening*
- ✓ *Maximum 120 mm opening*
- ✓ *High temperature resistant material*
- ☑ *Low economic cost*
- ✓ *Manufacturable*
- ✓ *Mountable on the solar reactor*
- ✓ *Driven by a stepper motor*
- ✓ *Precise control of the aperture surface*
- ✓ *Water sealed blades*
- ✓ *Minimum overall size of the mechanism*
- ✓ *Tubing connections should not interfere each other during motion of the blades*
- ✓ *Tubing connections should not be on the pathway of the light beam*
- ✓ *Blades motion should not be lammed, minimal friction between the moving parts*

Figure 6-1 Checklist of design requirements

Making a mechanism meeting all the requirements listed in Figure 6-1 is quite a challenge. However, the mechanism described in this thesis succeeds at doing so. It isn't even that expensive to manufacture such an iris mechanism with build-in heat exchanger, but since the desired dimensions of the raw material were not available, more material had to be ordered than needed. This almost doubled the costs of the ordered material. For the experiments, some accurate measuring devices such as a flow meter and a barometer had to be ordered. These devices are rather expensive but are not a crucial part for the performance of the iris mechanism itself.

Although the mechanism described in this thesis is a new and more energy-efficient variable aperture mechanism, some adjustments can be made to further increase the performance.

A major uncertainty in simulations is the emissivity coefficient of the material of the blades. Since this value has a great influence on the overall heat exchange mechanism, an experimental identification of this value will strongly increase the accuracy of the simulations. It can also be noted that a higher absorbance coefficient results in more energy capture. Therefore, a study examining several coatings and paints would also contribute to achieve higher performance. During this study, it is very important to identify the maximum temperature which these coatings or paints can withstand.

Already a large number of different water channels are examined for the purpose of achieving the highest efficiency concerning the heat transfer. A study focused on the water channel without taking any other constraints into consideration, except for a minimal overall thickness, would be very beneficial for this research topic. For example, the mechanism described in this thesis is subject to some manufacturing constraints of the machine shop at campus De Nayer. It is possible that with a different manufacturing method, another shape can be made which would enhance the performance. The mechanism described in this thesis already indicates that water inside the blades strongly reduces the temperature of the blades and certain amount of the blocked energy can be re-used. This conclusion should not be the end of the research of a variable aperture mechanism. On the contrary, this thesis offers the start of a new research field, which is focused on the recovery of the blocked energy.

When assembling the tubes for the water on to the mechanism, it became clear that the connections designed for the tubes were non- ideal. Due to manufacturing errors, the connections were not perfect circular and not long enough to hold the clamps at their place. It is recommended for further improvements of the mechanism to reconsider the connections of the water channels. When performing the experiments on to the solar reactor, the parts of the water tubes touching the backplate and the bolts, needed to mount the mechanism on the solar reactor, started to melt due to the high temperatures. Metal braided hoses are a solution to this problem. They can withstand higher temperatures and higher water pressures. Also, the usage of clamps and Teflon can be excluded due to the fact that these metal hoses can be welded on to the iris blades. Hoses like the M2B1006 from the company Xtraflex can withstand temperatures up to 550 °C and a working pressure of 154 bar at 20 °C. Since these hoses are also made of 316L, they can easily be welded on the blades.

7 REFERENCES

[1] Eurostat, “Eurostat regional yearbook, 2017 Edition,” *Publications Office of the European Union*. pp. 24–26, 2017.

[2] British Petroleum, “2017 Energy Outlook,” *BP Statistical Review of World Energy*. pp. 9–11, 2017.

[3] M. Engin, “Sizing and simulation of PV-wind hybrid power system,” *Int. J. Photoenergy*, vol. 2013, no. 1, pp. 1–8, 2013.

[4] L. Charpentier, K. Dawi, J. Eck, B. Pierrat, J.-L. Sans, and M. Balat-Pichelin, “Concentrated Solar Energy to Study High Temperature Materials for Space and Energy,” *J. Sol. Energy Eng.*, vol. 133, no. 3, pp. 1–8, 2011.

[5] C. Ophoff, S. Korotunov, and N. Ozalp, “Optimization of Design and Process Parameters for Maximized and Stable Solar Receiver Efficiency,” in *Proceedings of the 2nd Thermal and Fluid Engineering Conference*, 2017, pp. 1–2.

[6] D. M. Rowe, “Thermoelectrics, an environmentally-friendly source of electrical power,” *Renewable Energy*, vol. 16, no. 1–4. pp. 1251–1256, 1999.

[7] C. Ophoff, “Iris Shutter Mechanism,” KU Leuven, 2015.

[8] Y. A. Cengel and M. A. Boles, “Thermodynamics an engineering approach,” *Mc Graw Hill Education*, vol. 1. pp. 1–19, 2002.

[9] C. Ophoff, H. A. Najafabadi, J. Bogaerts, N. Ozalp, and D. Moens, “An overview of variable aperture mechanisms in attempt to control temperature inside solar cavity receivers,” in *Proceedings of the 3rd Thermal and Fluids Engineering Conference (TFEC)*, 2018, pp. 1–12.

[10] N. Ozalp, A. Toyama, J. Devanuri, R. Rowshan, and Y. Al-Hamidi, “Effect of Cameralike Aperture in Quest for Maintaining Quasi-Constant Radiation Inside a Solar Reactor,” *J. Mech. Des.*, vol. 133, no. 2, pp. 1–7, 2011.

[11] Y. Al-Hamidi, S. Abdulla, M. El Zamli, I. Rizk, and N. Ozalp, “Design , Manufacturing and Testing of an Aperture Mechanism for a solar reactor,” in *Proceedings of the ASME 5th International Conference on Energy Sustainability*, 2011, pp. 1–12.

[12] J. Bogaerts, “Design and manufacturing of a smart iris mechanism for a solar reactor,” KU Leuven, 2016.

[13] S. Roth, M. Ignatowitz, P. Müller, W. Mönch, and E. Oesterschulze, “Non-mechanical variable apertures based on poly(3,4-ethylenedioxythiophene) (PEDOT),” *Microelectron. Eng.*, vol. 88, no. 8, pp. 2349–2351, Aug. 2011.

[14] J. Ouyang and Y. Yang, “Conducting polymer as transparent electric glue,” *Adv. Mater.*, vol. 18, pp. 2141–2144, 2006.

[15] S. Abdulla *et al.*, “Design, manufacturing and testing of a camera-like aperture mechanism for a solar reactor,” in *ASME 2011 International Mechanical Engineering Congress & Exposition*, 2011, pp. 1–15.

[16] H. Wittel, D. Muhs, D. Jannasch, and J. Vossbiek, *RoloffMatek*, 5th ed. Amsterdam: Boom uitgevers Amsterdam, 2013.

[17] N. L. Parthasarathi, U. Borah, and S. K. Albert, “Correlation Between Coefficient of Friction and Surface Roughness in Dry Sliding Wear of Aisi 316 L (N) Stainless Steel At Elevated Temperatures,” *Comput. Model. New Technol.*, vol. 17, no. 1, pp. 51–63, 2013.

[18] P. Hanrahan, “Monte Carlo path tracing.” Stanford University, Stanford, CA, pp. 1–19,

2016.

[19] F. E. Nicodemus, J. C. Richmond, J. J. Hsia, I. W. Ginsberg, and T. Limperis, “Geometrical considerations and nomenclature for reflectance,” *U.S. departement of commerce - National bureau of standards*. Washington D.C., pp. 1–52, 1977.

[20] Lambda Research Corporation, “Trace Pro User’s Manual.” Lambda Research Corporation, Littleton, New Hampshire, p. 1.1-1.3, 7.1-7.3, 2017.

[21] D. Jacobsen and M. Gauvin, “TracePro ’ s Monte Carlo Raytracing Methods , reducing statistical noise , memory usage and raytrace times.” Lambda Research Corporation, 2012.

[22] D. B. Kim, K. S. Park, K. Y. Kim, M. K. Seo, and K. H. Lee, “High-dynamic-range camera-based bidirectional reflectance distribution function measurement system for isotropic materials,” *Opt. Eng.*, vol. 48, no. 9, p. 093601, 2009.

[23] Siemens PLM Software, “Siemens NX 11.” Siemens Product Lifecycle Management Software Inc., 2016.

[24] Siemens PLM Software, “Simcenter Flow Solver Reference Manual.” Siemens Product Lifecycle Management Software Inc., 2016.

[25] Siemens PLM Software, “Thermal Analysis User’s Guide.” Siemens Product Lifecycle Management Software Inc., 2014.

[26] P. Arras, “Numerieke Simulatietechnieken.” KU Leuven, Leuven, 2017.

[27] B. R. Munson, D. F. Young, T. H. Okiishi, and W. W. Huebsch, *Fundamentals of fluid mechanics*. West Virginia: John Wiley & Sons Pte Ltd, 2010.

[28] O. C. Zienkiewicz and R. L. Taylor, “The Finite Element Method Volume 1 : The Basis,” *Methods*, vol. 1, pp. 1–708, 2000.

[29] G. Design, “CES EduPack Software.” Granta Design Ltd., Cambridge, 2017.

[30] S. Holmström, R. Pohja, A. Nurmela, P. Moilanen, and P. Auerkari, “Creep and creep-fatigue behaviour of 316 stainless steel,” in *Procedia Engineering*, 2013, vol. 55, pp. 160–164.

[31] Mikron Instrument Company, “Table of Emissivity of Various Surfaces,” pp. 1–13, 2014.

[32] H. J. J. Kals, C. Buiting-Csikos, and C. A. van Luttervelt, *Industriële productie: Het voortbrengen van mechanische producten*. 2012.

[33] The Lincoln Electric Company, “How a plasma cutter works,” 2018. [Online]. Available: https://www.lincolnelectric.com/en-us/equipment/plasma-cutters/process-and-theory/Pages/how-a-plasma-cutter-works.aspx. [Accessed: 20-May-2018].

[34] M. Kaladhar, K. V. Subbaiah, and C. H. S. Rao, “Machining of austenitic stainless steels - a review,” *Int. J. Mach. Mach. Mater.*, vol. 12, no. 1/2, pp. 178–192, 2012.

[35] D. R. Patra and I. S. Rout, “Parametric Optimization of WEDM parameters on EN 31 steel for lower surface roughness using taguchi method,” *IOSR J. Mech. Civ. Eng.*, vol. 13, no. 1, pp. 21–26, 2015.

[36] L. Holland, “The effect of gettering on the reflectivity of aluminium films,” *Br. J. Appl. Phys.*, vol. 9, no. 8, pp. 336–337, 1958.

[37] R. M. Kelly, “Thermal conductivity of aluminium foil,” Massachusetts Institute of Technology, 1931.

Appendices

Appendix A TECHNICAL DRAWINGS

Exploded view

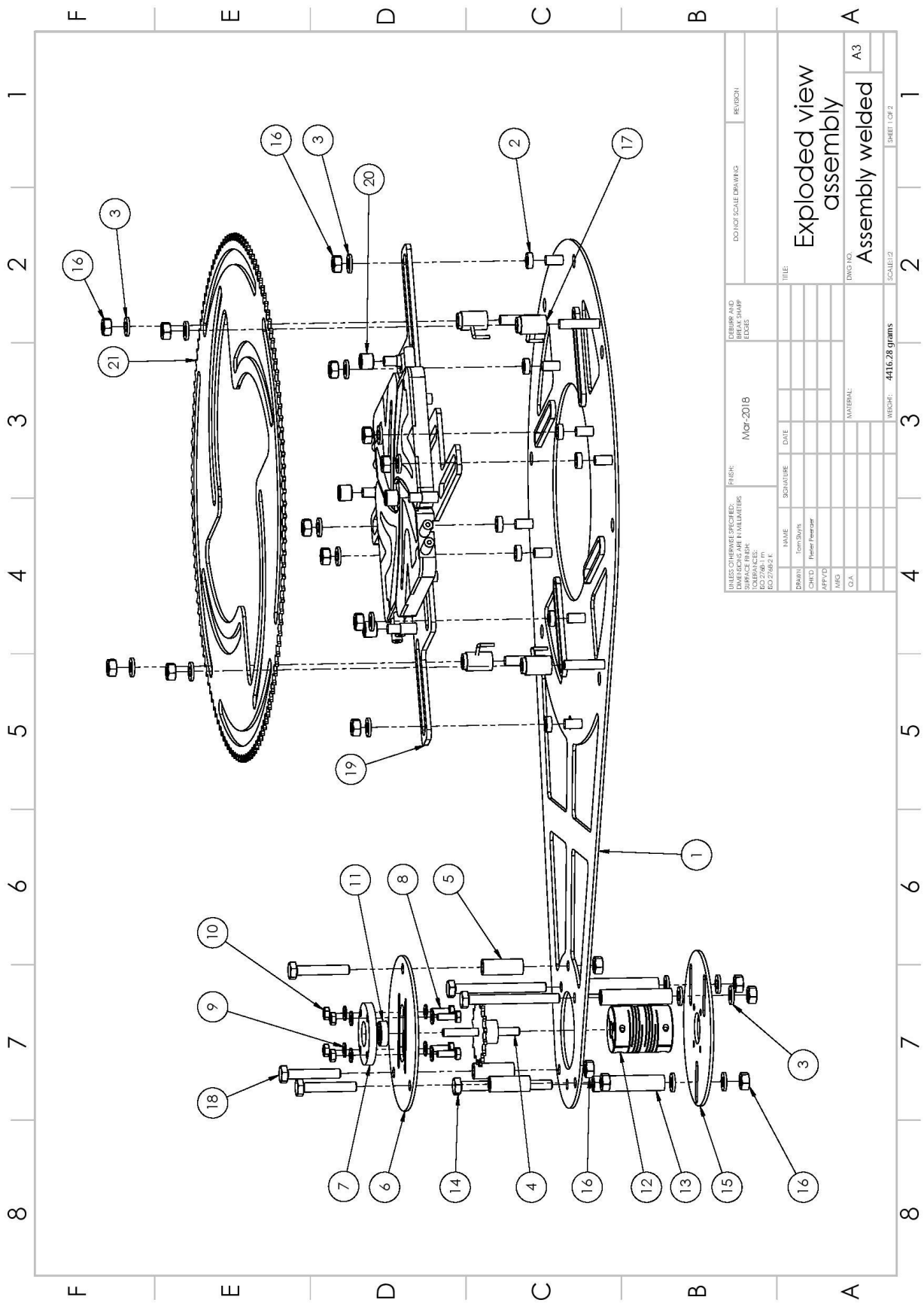

ITEM NO.	PART NUMBER	DESCRIPTION	QTY.
1	Welding backplate	Supporting plate of the mechanism	1
2	Ring blade	Hub pin-slot mechanism blades	8
3	M6 washer	M6 washer	18
4	Welding shaft - small sprocket	Driving shaft of the mechanism	1
5	Ring small sprocket	Spacer ring frontplate small sprocket wheel	3
6	Frontplate smal sprocket	Frontplate small sprocket wheel	1
7	Connection bearing	Supporting bearing holder	1
8	M4x12 bolt	Hexagonal bolt M4 x 12 mm	4
9	M4 washer	Washer M4	8
10	M4 nut	Hexagonal nut M4	4
11	625	Deep groove ball bearing SKF 625	1
12	mwc30-10mm-3_8_-a	MULTI 6-BEAM Coupling Aluminium L168 alloy Size 25	1
13	Ring connection motor	Spacer connection motor	3
14	M6x60 bolt	Hexagonal bolt M6 x 60 mm	3
15	Connection motor	Connection for stepper motor	1
16	M6 nut	Hexagonal nut M6	18
17	Welding ring actuator + clip hose	Hub pin-slot mechanism actuator + clip hose	4
18	M6 x 35mm bolt	Hexagonal bolt M6 x 35mm	3
19	Welding blades	Blades of the iris mechanism	4
20	inafag_hk0608_91sgn3jur15eudo6i0layu6nj	Needle roller bearing HK0608	4
21	Sprocket wheel(new)	Actuator translation blades	1

UNLESS OTHERWISE SPECIFIED:
DIMENSIONS ARE IN MILLIMETERS
SURFACE FINISH:
TOLERANCES:
ISO 2768-1 m
ISO 2768-2 K

FINISH: Mar-2018

DEBURR AND BREAK SHARP EDGES

DO NOT SCALE DRAWING | REVISION

	NAME	SIGNATURE	DATE
DRAWN	Tom Sluyts		
CHK'D	Pieter Peeraer		
APPV'D			
MFG			
Q.A			

TITLE: Exploded view assembly

MATERIAL: Assembly welded

DWG NO. A4

WEIGHT: 4416.28 grams

SCALE:1:2

SHEET 2 OF 2

Backplate

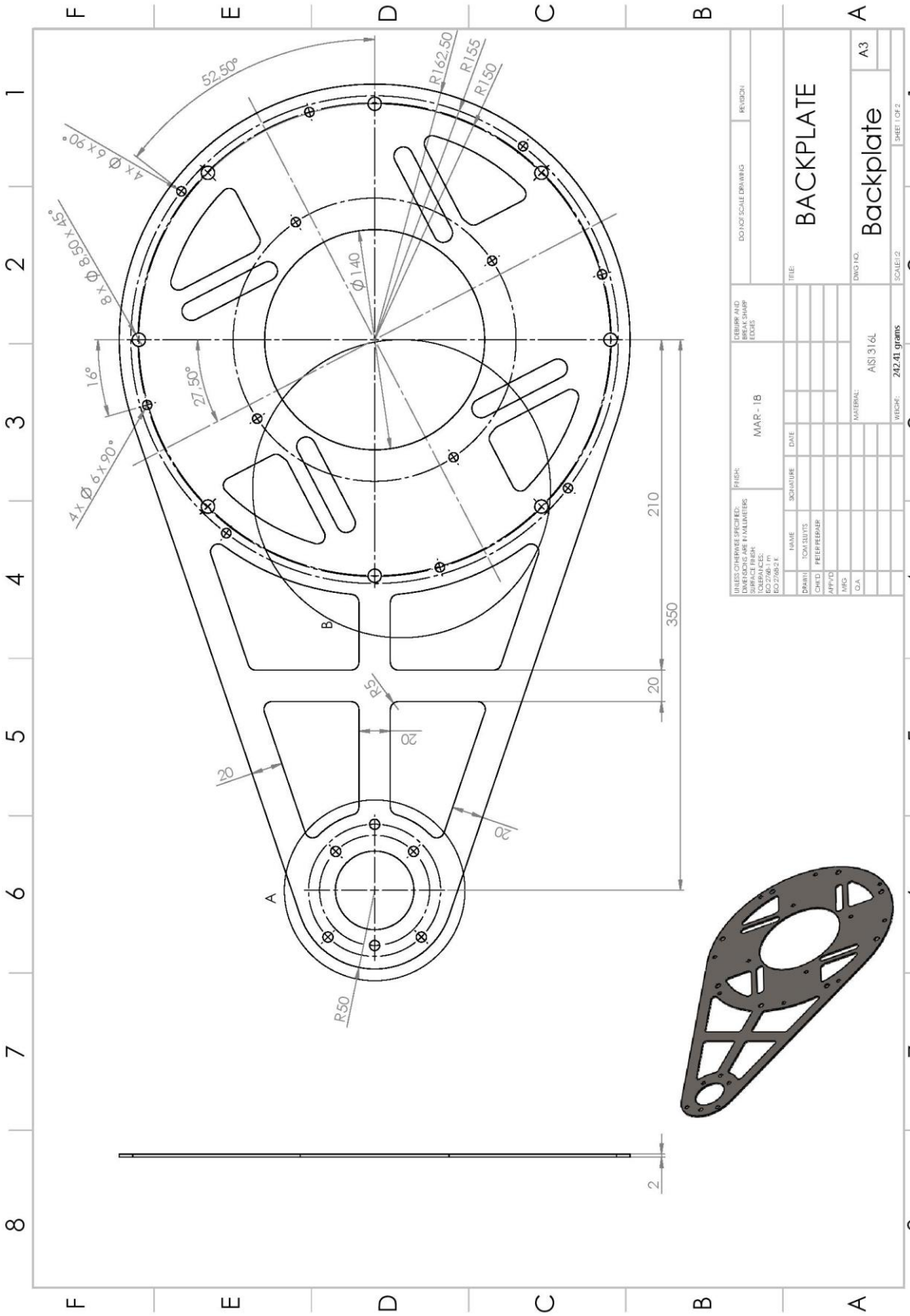
BACKPLATE
Backplate
A3
MAR - 18
AISI 316L
242.41 grams
DO NOT SCALE DRAWING
DEBURR AND BREAK SHARP EDGES
UNLESS OTHERWISE SPECIFIED:
DIMENSIONS ARE IN MILLIMETERS
SURFACE FINISH:
TOM SELLITS
PETER PEEPHAR
52.50°
R162.50
R155
R150
4x Ø 6x 90°
8x Ø 8 Ø 15x 45°
Ø 140
16°
27.50°
210
350
20
R50
2

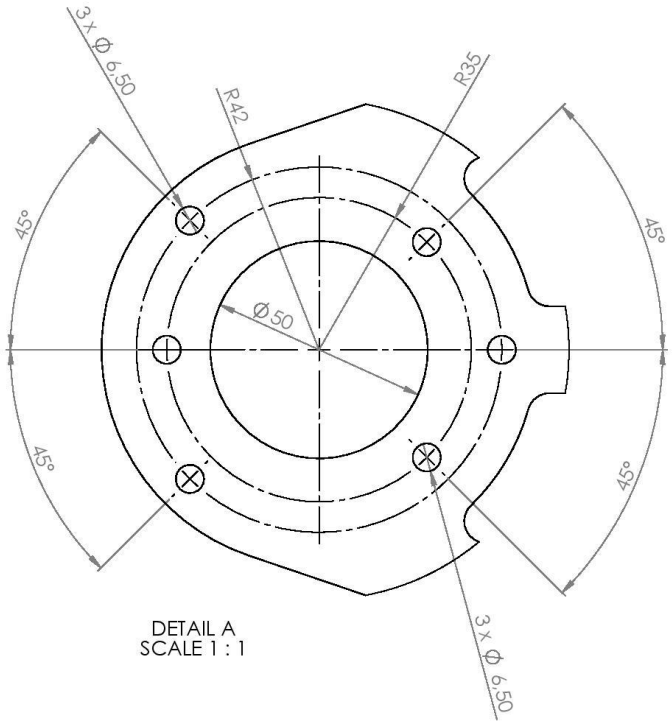

DETAIL A
SCALE 1 : 1

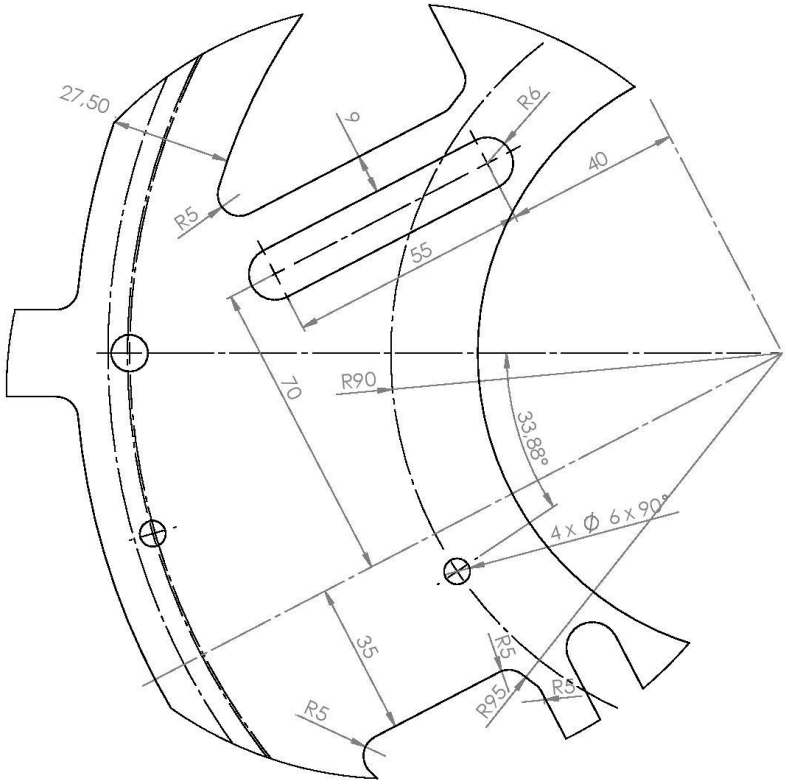

DETAIL B
SCALE 1 : 1

UNLESS OTHERWISE SPECIFIED: DIMENSIONS ARE IN MILLIMETERS SURFACE FINISH: TOLERANCES: ISO 2768-1 m ISO 2768-2 K			FINISH: MAR - 18			DEBURR AND BREAK SHARP EDGES	DO NOT SCALE DRAWING / REVISION
	NAME	SIGNATURE	DATE				TITLE: BACKPLATE
DRAWN	TOM SILLYTS						
CHK'D	PIETER PEERAER						
APPV'D							
MFG							
Q.A.				MATERIAL: AISI 316L			DWG NO. Backplate / A3
				WEIGHT: 242.41 grams			SCALE:1:2 / SHEET 2 OF 2

Slot

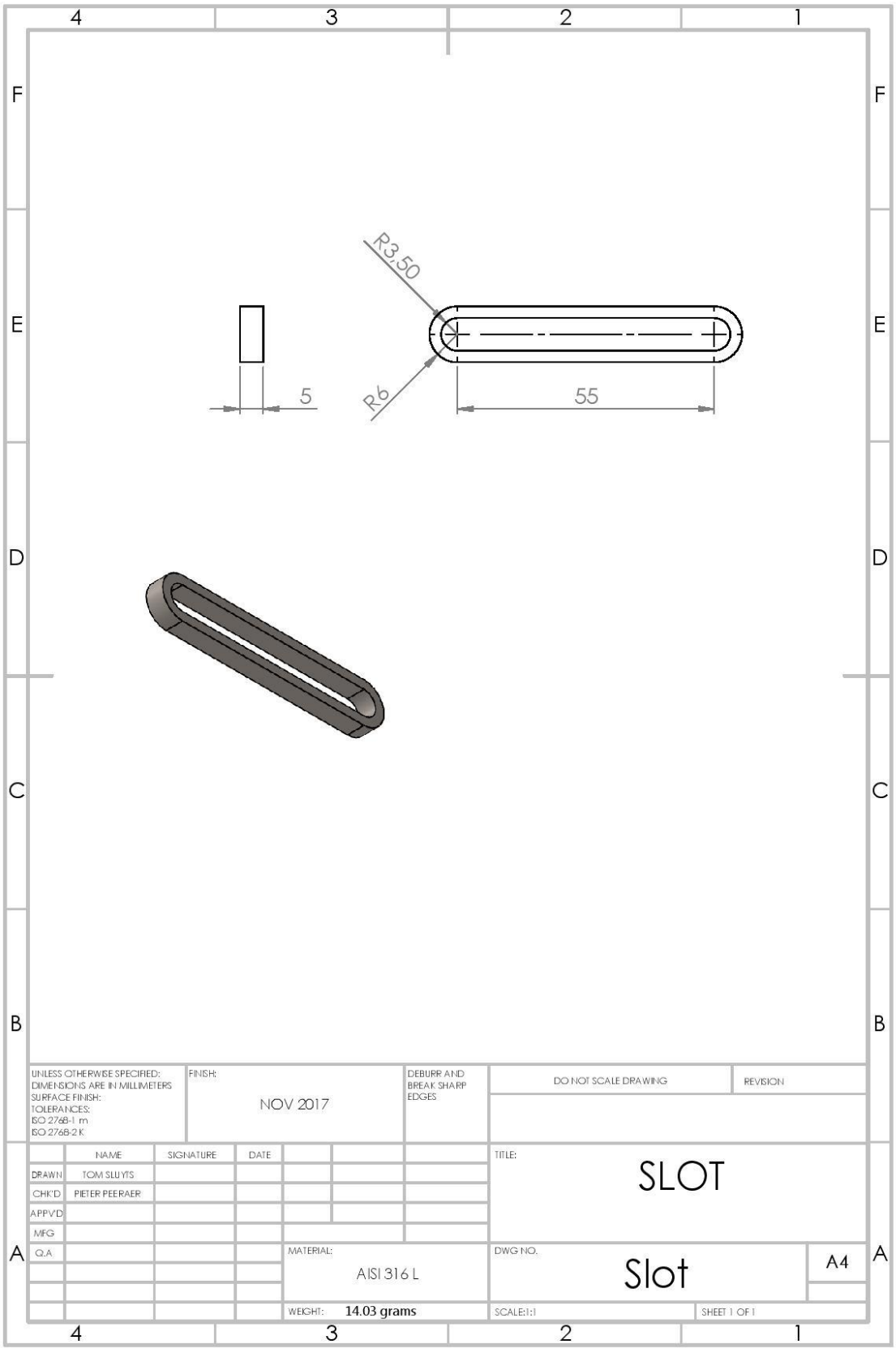
4
3
2
1
F
E
D
C
B
A
R3.50
5
R6
55
UNLESS OTHERWISE SPECIFIED:
DIMENSIONS ARE IN MILLIMETERS
SURFACE FINISH:
TOLERANCES:
ISO 2768-1 m
ISO 2768-2 K
FINISH:
NOV 2017
DEBURR AND
BREAK SHARP
EDGES
DO NOT SCALE DRAWING
REVISION
NAME
SIGNATURE
DATE
DRAWN
TOM SLUYTS
CHK'D
PIETER PEERAER
APPV'D
MFG
Q.A
MATERIAL:
AISI 316 L
WEIGHT:
14.03 grams
TITLE:
SLOT
DWG NO.
Slot
A4
SCALE:1:1
SHEET 1 OF 1

Welding backplate

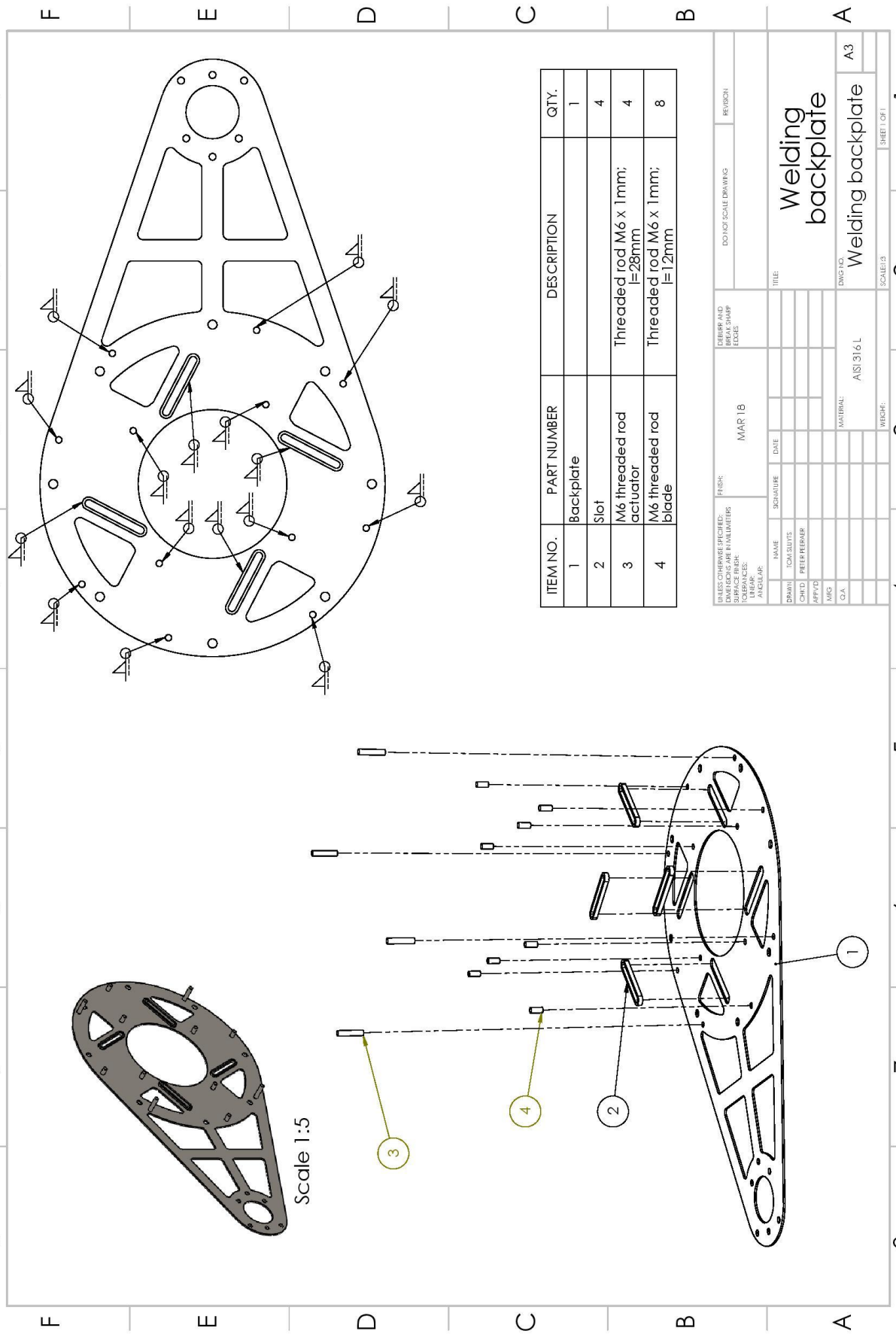

Blade

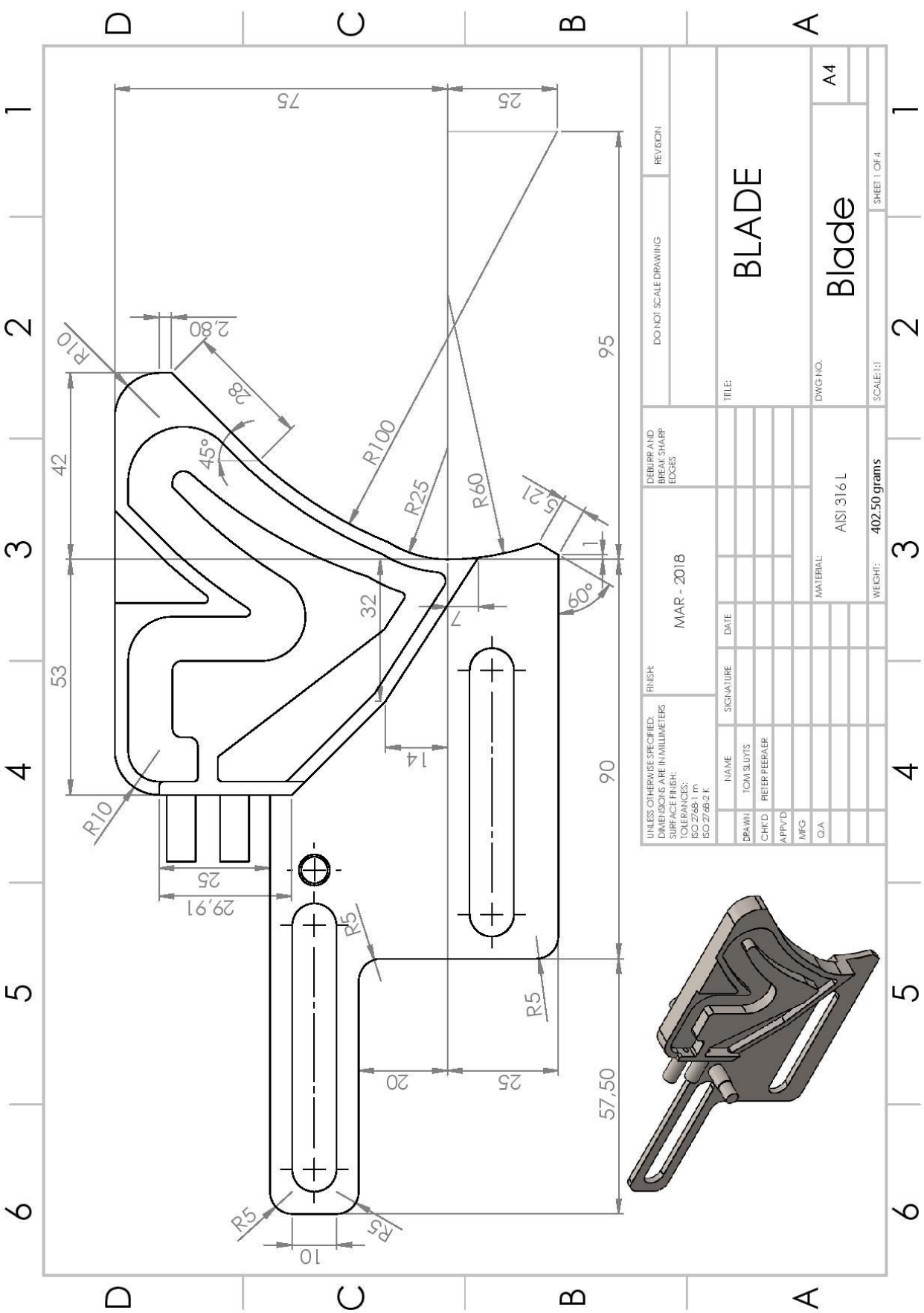
BLADE
Blade
A4
AISI 316 L
402.50 grams
MAR - 2018
DEBURR AND BREAK SHARP EDGES
DO NOT SCALE DRAWING
TOM SLUYS
PIETER PEEPAER
75
25
95
90
57,50
42
53
32
14
7
2,80
38
45°
R10
R100
R25
R60
R5
R2
60°
1
2
29,91
20
10

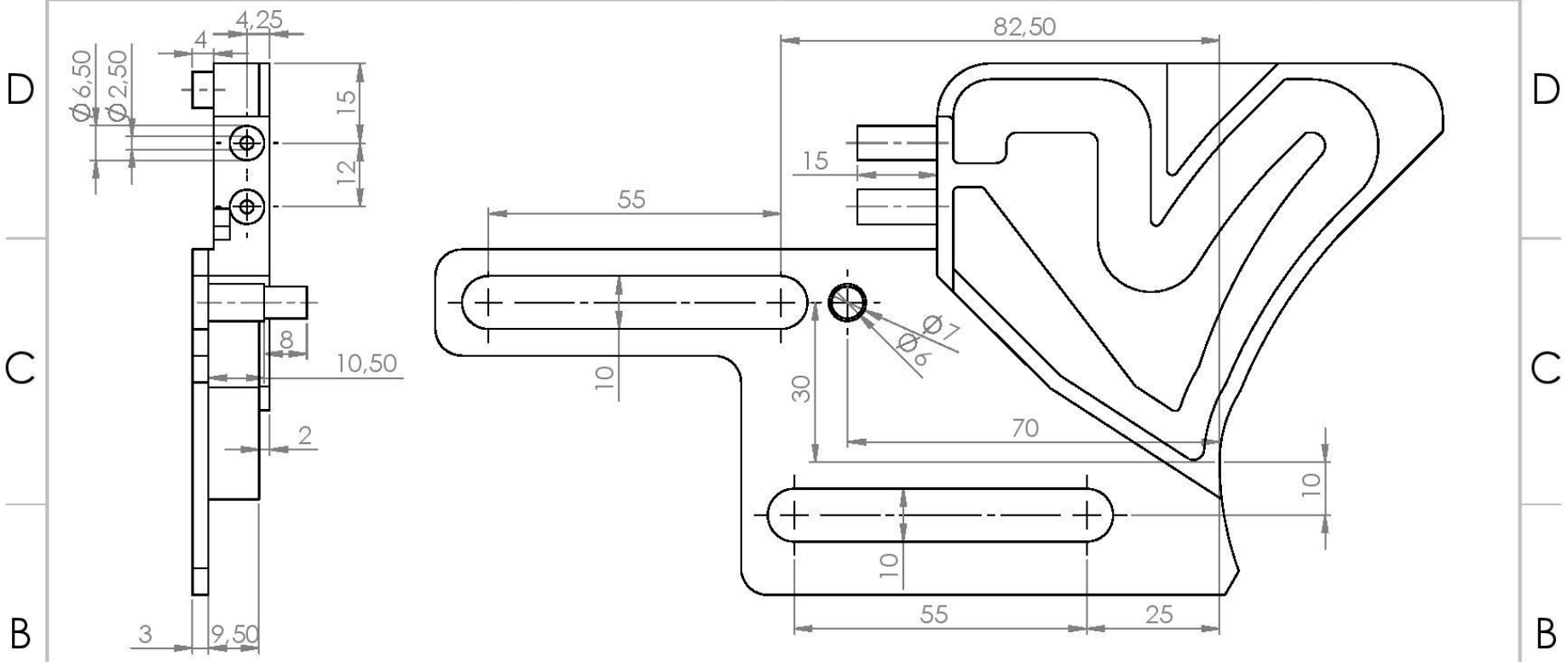

UNLESS OTHERWISE SPECIFIED: DIMENSIONS ARE IN MILLIMETERS SURFACE FINISH: TOLERANCES: ISO 2768-1 m ISO 2768-2 K		FINISH: MAR - 2018			DEBURR AND BREAK SHARP EDGES	DO NOT SCALE DRAWING	REVISION
	NAME	SIGNATURE	DATE			TITLE: BLADE	
DRAWN	TOM SLUYTS						
CHK'D	PIETER PEERAER						
APPV'D							
MFG							
Q.A				MATERIAL: AISI 316 L		DWG NO. Blade	A4
				WEIGHT: 402.50 grams		SCALE: 1:1	SHEET 2 OF 4

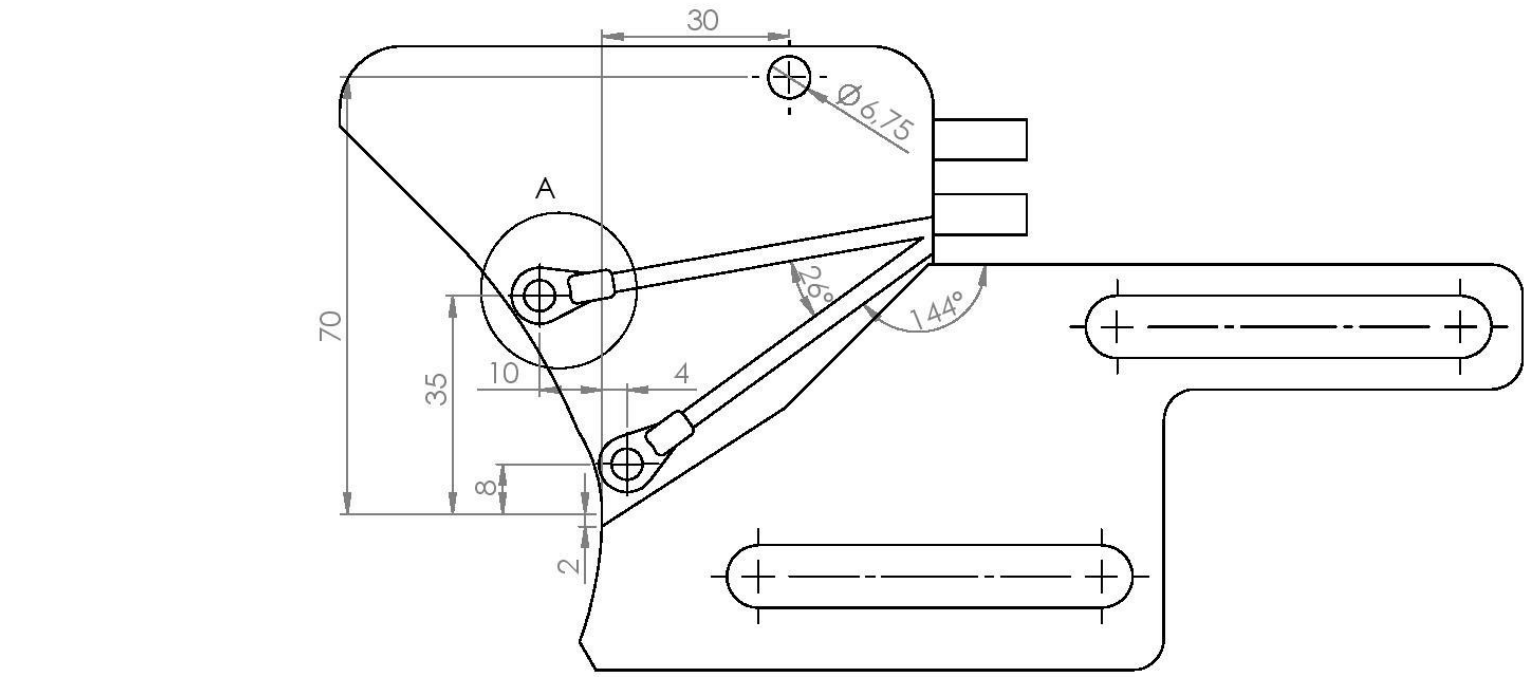

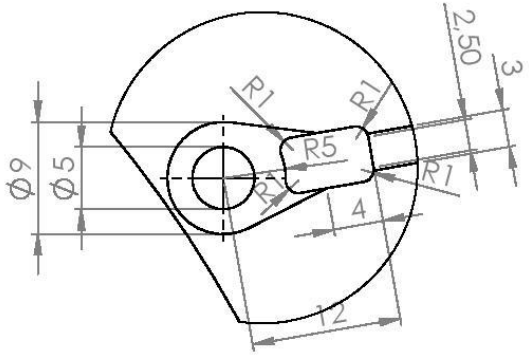

DETAIL A
SCALE 2 : 1

UNLESS OTHERWISE SPECIFIED: DIMENSIONS ARE IN MILLIMETERS SURFACE FINISH: TOLERANCES: ISO 2768-1 m ISO 2768-2 K			FINISH: MAR - 2018			DEBURR AND BREAK SHARP EDGES	DO NOT SCALE DRAWING	REVISION
	NAME	SIGNATURE	DATE				TITLE: BLADE	
DRAWN	TOM SLUYTS							
CHK'D	PIETER PEERAER							
APPV'D								
MFG								
Q.A				MATERIAL: AISI 316 L			DWG NO. Blade	A4
				WEIGHT: 402.50 grams			SCALE: 1:1	SHEET 3 OF 4

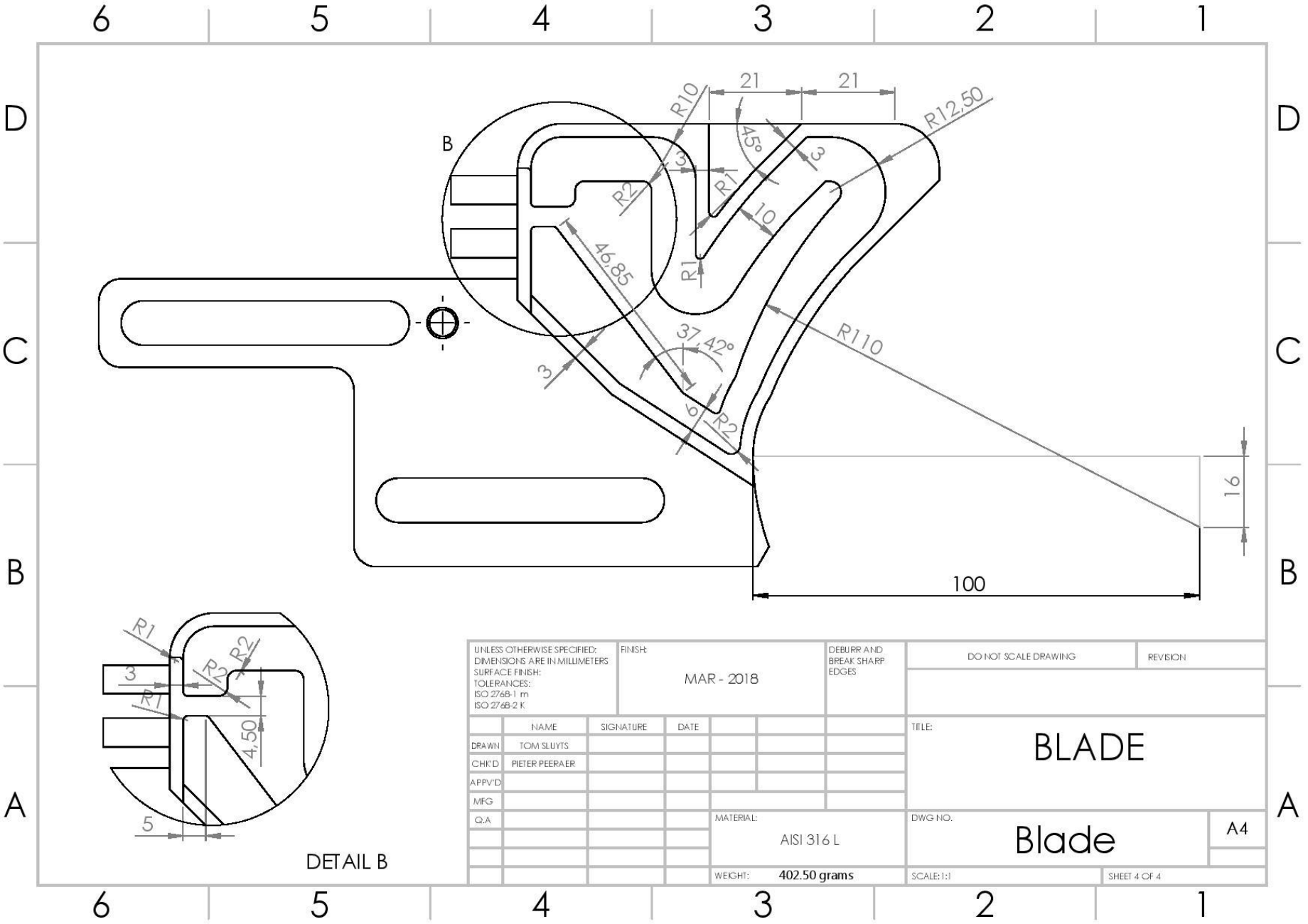
6
5
4
3
2
1
D
C
B
A
R10
21
21
R12,50
45°
3
3
R2
R1
10
R1
46,85
37,42°
3
R110
6
R2
16
100
B
R1
R2
R2
3
R1
4,50
5
DETAIL B
UNLESS OTHERWISE SPECIFIED:
DIMENSIONS ARE IN MILLIMETERS
SURFACE FINISH:
TOLERANCES:
ISO 2768-1 m
ISO 2768-2 K
FINISH:
MAR - 2018
DEBURR AND BREAK SHARP EDGES
DO NOT SCALE DRAWING
REVISION
NAME
SIGNATURE
DATE
DRAWN
TOM SLUYTS
CHK'D
PIETER PEERAER
APPV'D
MFG
Q.A
TITLE:
BLADE
MATERIAL:
AISI 316 L
DWG NO.
Blade
A4
WEIGHT:
402.50 grams
SCALE: 1:1
SHEET 4 OF 4

Cover

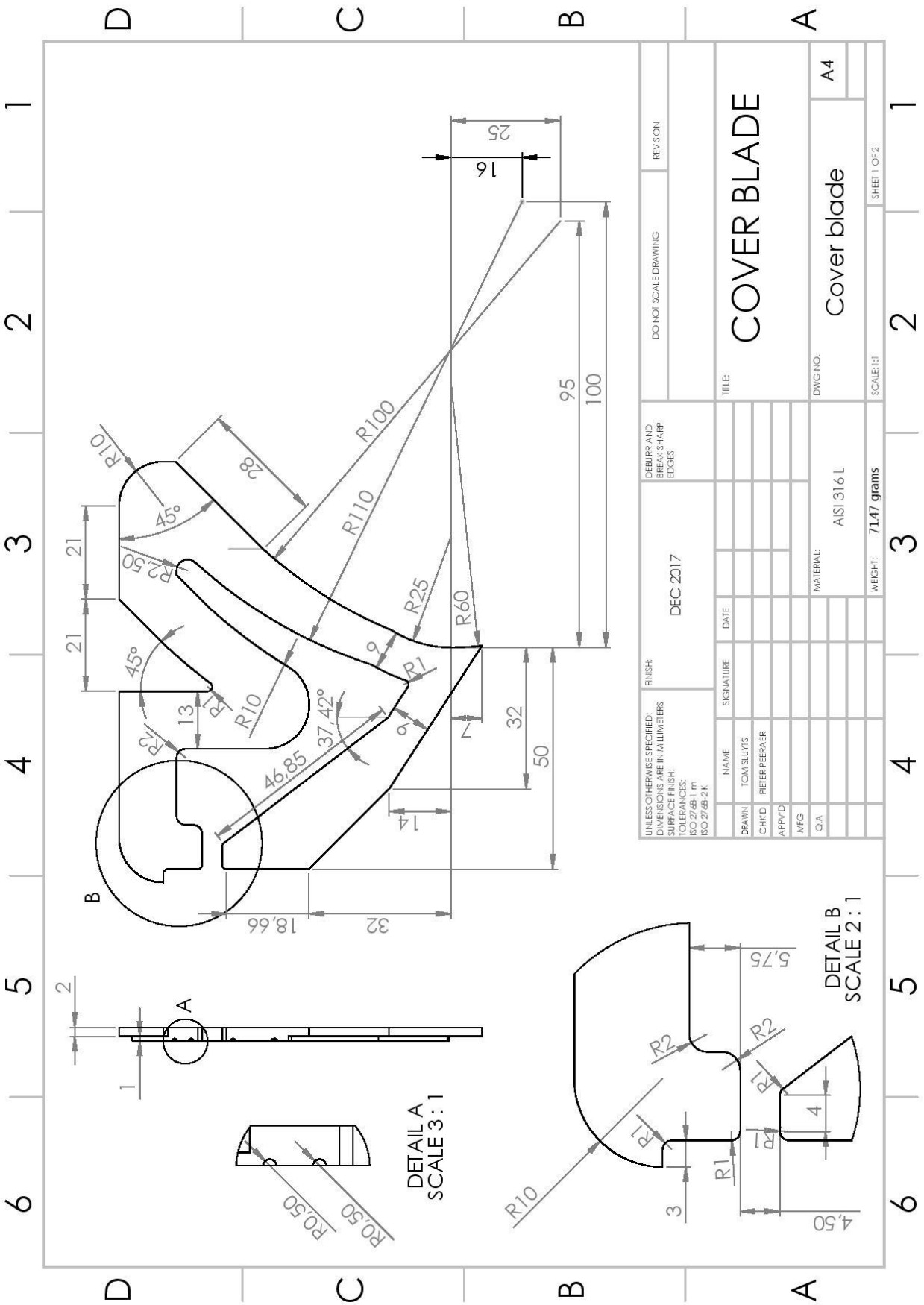
COVER BLADE
Cover blade
A4
DWG NO.
TITLE:
DO NOT SCALE DRAWING
REVISION
DEBURR AND BREAK SHARP EDGES
FINISH:
DEC 2017
UNLESS OTHERWISE SPECIFIED:
DIMENSIONS ARE IN MILLIMETERS
SURFACE FINISH:
TOLERANCES:
ISO 2768 - m
ISO 2768 - K
NAME
SIGNATURE
DATE
DRAWN
TOM SLUYS
CHK'D
PIETER PEERAER
APPV'D
MFG
Q.A
MATERIAL:
AISI 316 L
WEIGHT:
71.47 grams
SCALE:1:1
SHEET 1 OF 2
DETAIL A
SCALE 3 : 1
DETAIL B
SCALE 2 : 1
R100
R110
R25
R60
R10
R7
R2.50
R2
R1
45°
37.42°
46,85
18,66
32
95
100
50
25
16
28
21
13
14
7
6
4
3
2
1
5,75
4,50
R0.50

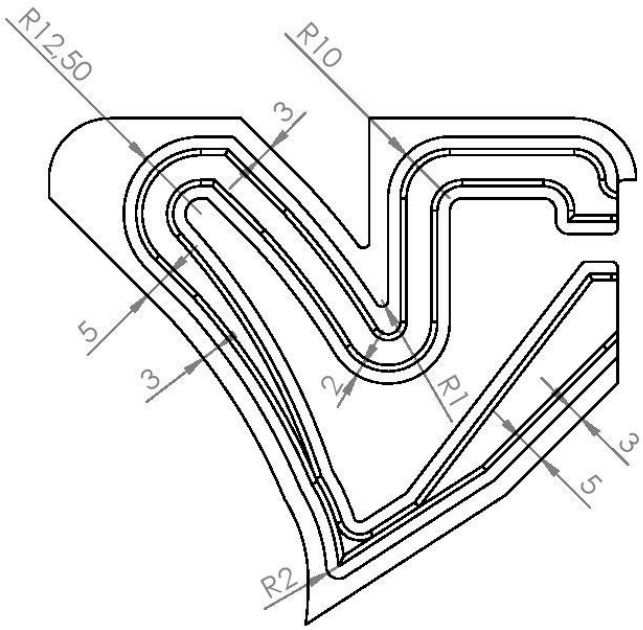

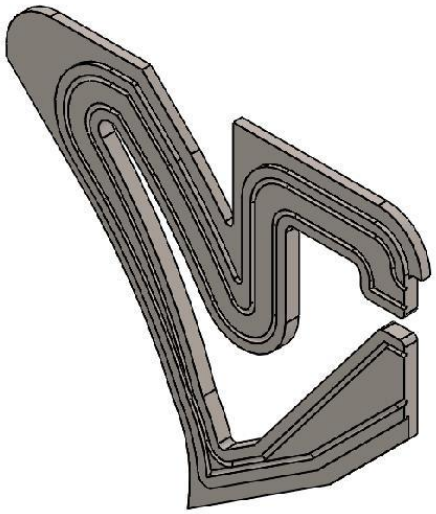

UNLESS OTHERWISE SPECIFIED: DIMENSIONS ARE IN MILLIMETERS SURFACE FINISH: TOLERANCES: ISO 2768-1 m ISO 2768-2 K		FINISH: DEC 2017		DEBURR AND BREAK SHARP EDGES		DO NOT SCALE DRAWING	REVISION
	NAME	SIGNATURE	DATE			TITLE: COVER BLADE	
DRAWN	TOM SLUYTS						
CHK'D	PIETER PEERAER						
APPV'D							
MFG							
Q.A				MATERIAL: AISI 316 L		DWG NO. Cover blade	A4
				WEIGHT: 71.47 grams		SCALE:1:1	SHEET 2 OF 2

Welding blade

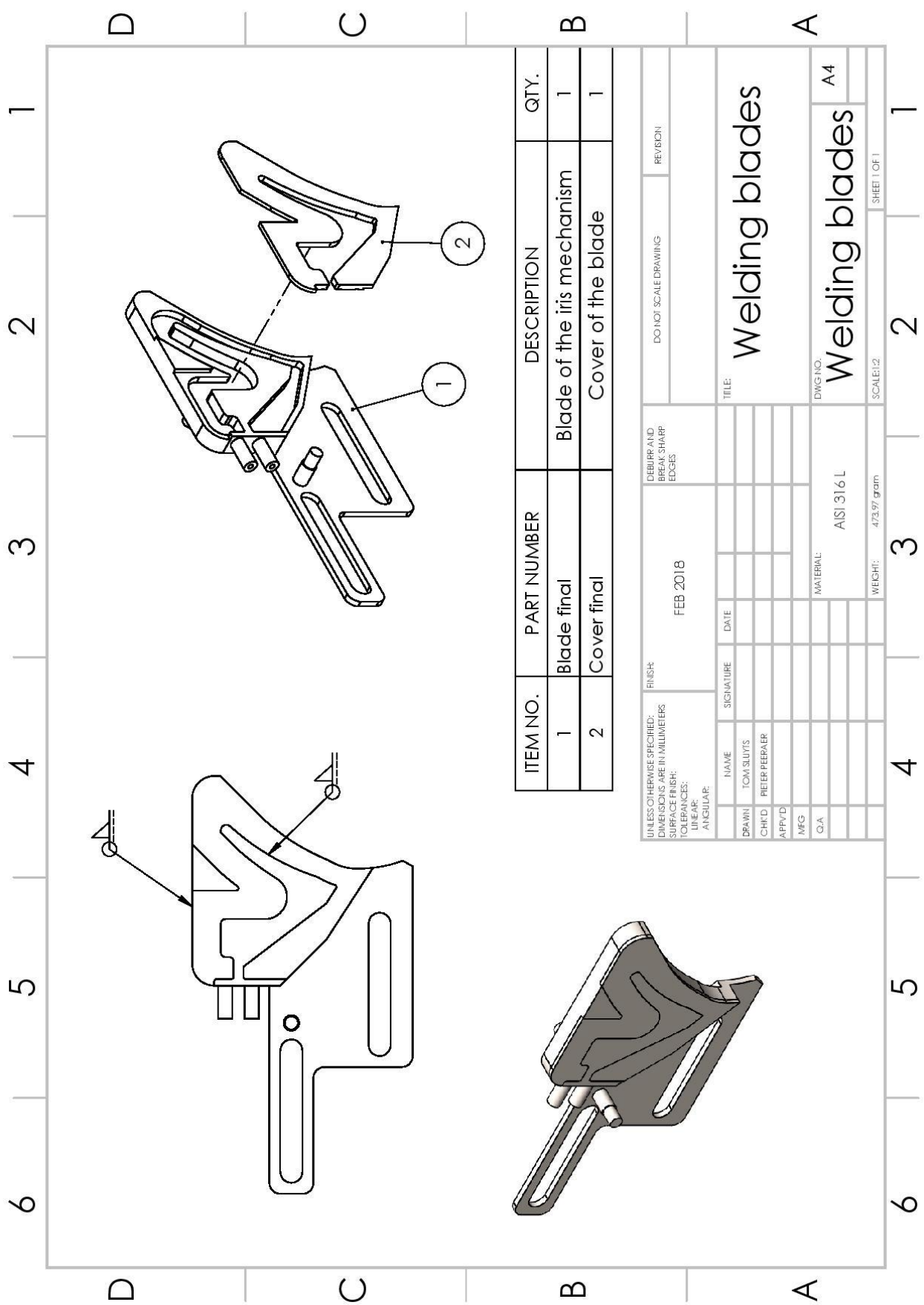

Actuator

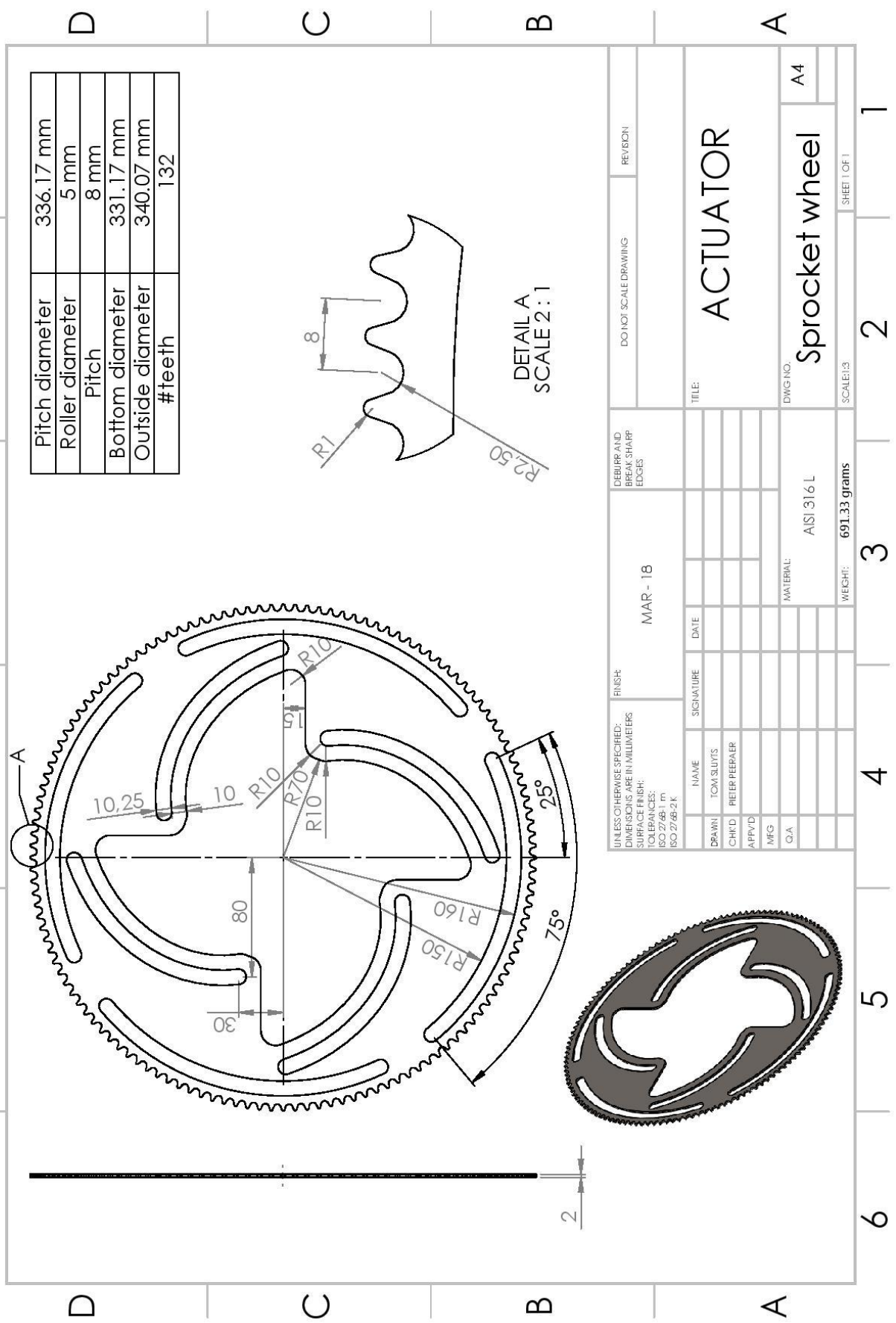
Pitch diameter 336.17 mm
Roller diameter 5 mm
Pitch 8 mm
Bottom diameter 331.17 mm
Outside diameter 340.07 mm
#teeth 132
DETAIL A
SCALE 2 : 1
R1
R2.50
8
ACTUATOR
Sprocket wheel
A4
MAR - 18
AISI 316 L
691.33 grams
DO NOT SCALE DRAWING
DEBURR AND BREAK SHARP EDGES
UNLESS OTHERWISE SPECIFIED:
DIMENSIONS ARE IN MILLIMETERS
SURFACE FINISH:
TOLERANCES:
ISO 2768-1 m
ISO 2768-2 K
NAME
SIGNATURE
DATE
DRAWN TOM SLUYTS
CHK'D PIETER PEERAER
APPV'D
MFG
Q.A
MATERIAL:
WEIGHT:
SCALE:1:3
SHEET 1 OF 1
REVISION
TITLE:
DWG NO.
10,25
10
R10
R70
R10
15
25°
75°
R160
R150
80
30
2

Driving sprocket wheel

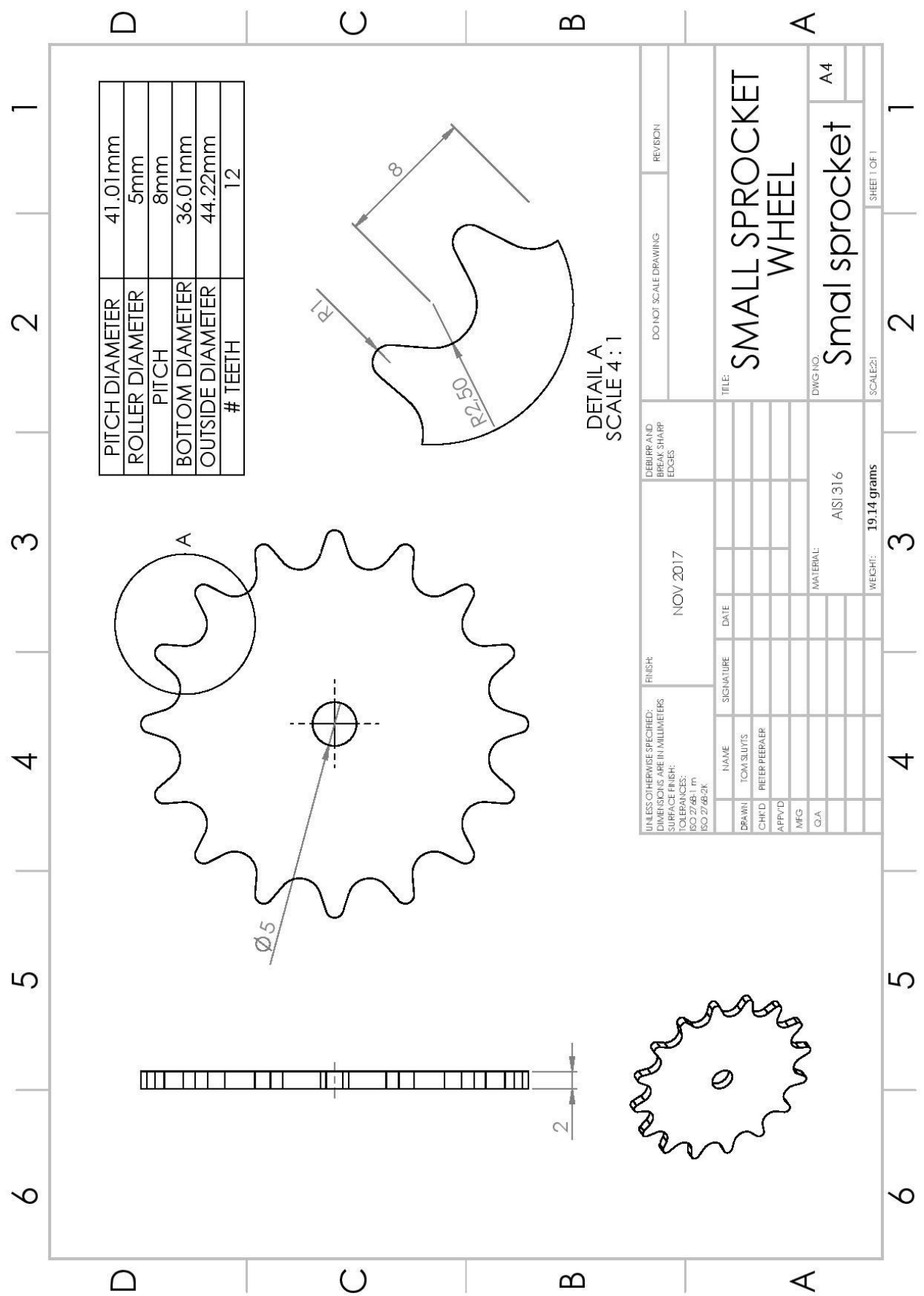

Shaft

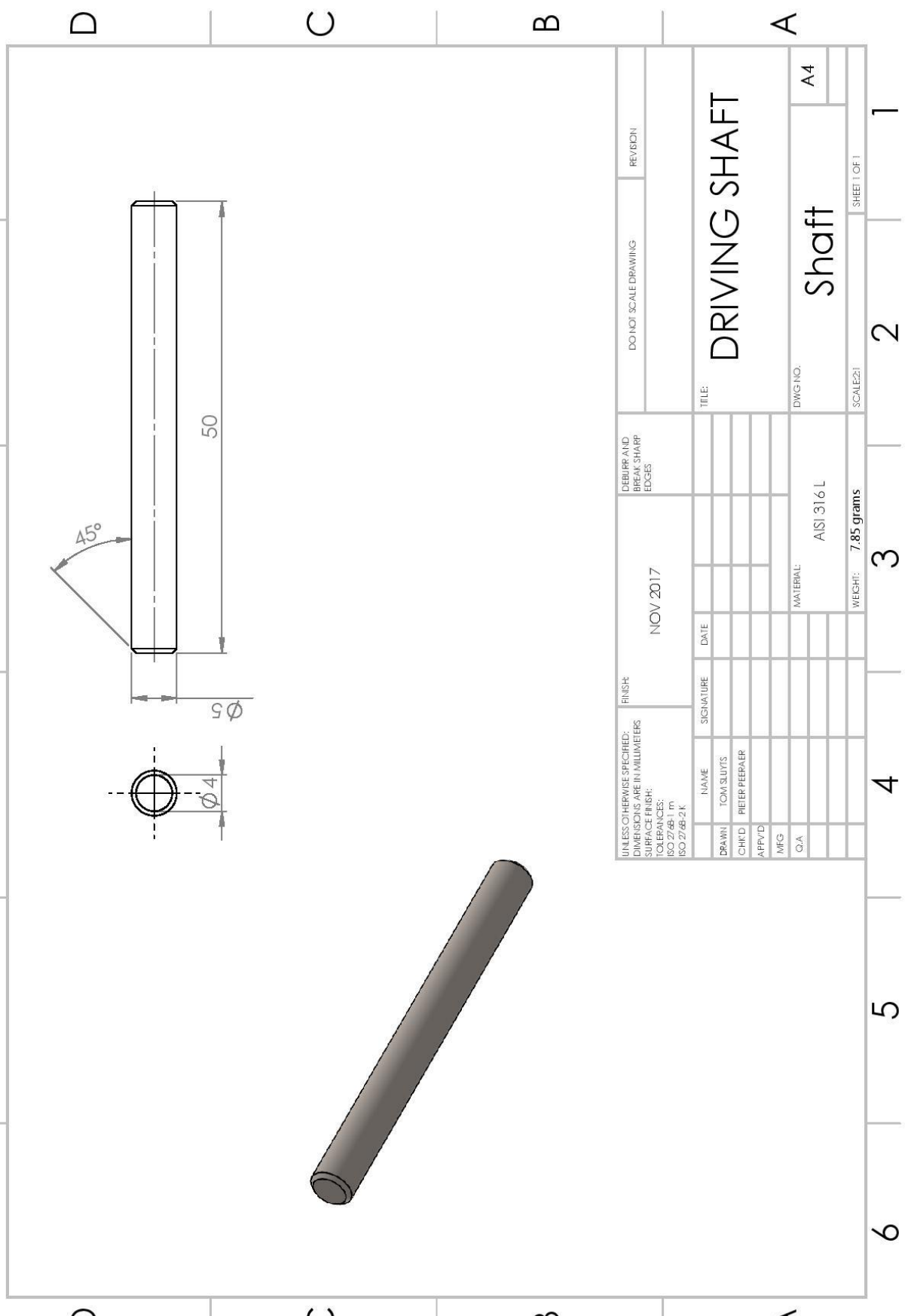
D
C
B
A
1
2
3
4
5
6
50
45°
5 Ø
Ø 4
UNLESS OTHERWISE SPECIFIED:
DIMENSIONS ARE IN MILLIMETERS
SURFACE FINISH:
TOLERANCES:
ISO 2768-1 m
ISO 2768-2 K
FINISH:
DEBURR AND BREAK SHARP EDGES
NAME
SIGNATURE
DATE
DRAWN
TOM SLUYTS
NOV 2017
CHK'D
PIETER PEERAER
APPV'D
MFG
Q.A
MATERIAL:
AISI 316 L
WEIGHT:
7.85 grams
DO NOT SCALE DRAWING
REVISION
TITLE:
DRIVING SHAFT
DWG NO.
Shaft
A4
SCALE:2:1
SHEET 1 OF 1

Hub small sprocket wheel

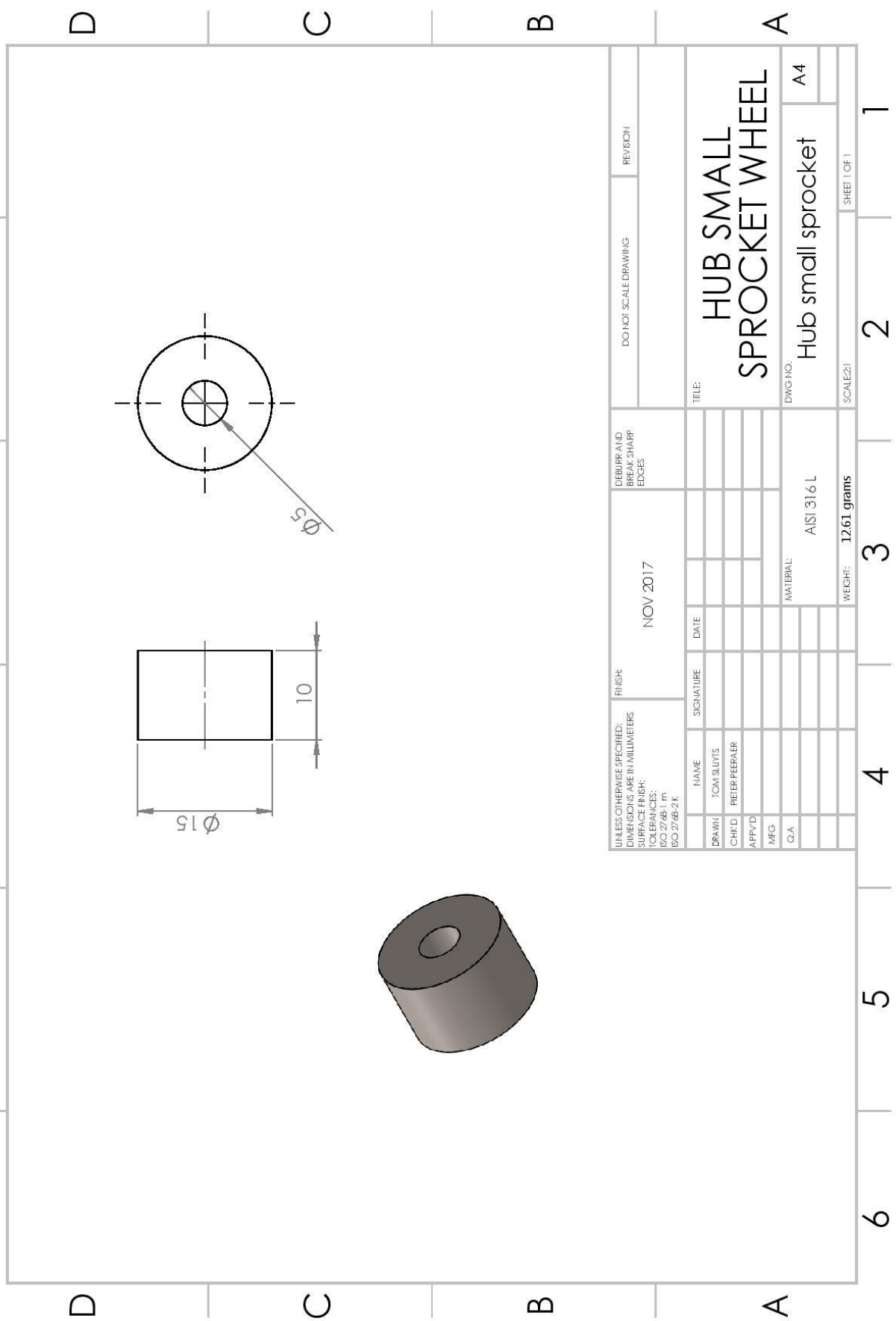

ITEM NO.	PART NUMBER	DESCRIPTION	QTY.
1	Smal sprocket	Driving sprocket wheel	1
2	Hub small sprocket	Supporting hub sprocket wheel	1
3	Shaft 5mm	Shaft d = 5mm; l = 50mm	1

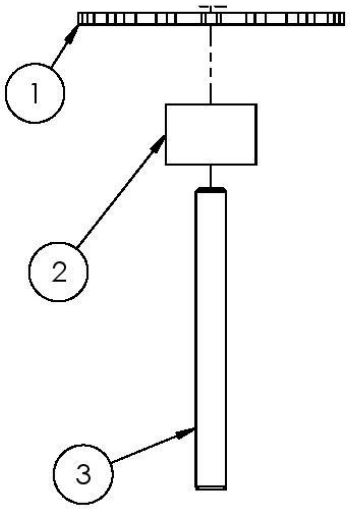

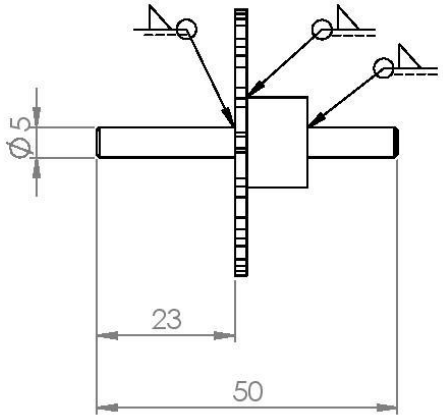

UNLESS OTHERWISE SPECIFIED: DIMENSIONS ARE IN MILLIMETERS SURFACE FINISH: TOLERANCES: LINEAR: ANGULAR:		FINISH: NOV 2017		DEBURR AND BREAK SHARP EDGES		DO NOT SCALE DRAWING	REVISION
	NAME	SIGNATURE	DATE			TITLE: Welding shaft on small sprocket wheel	
DRAWN	TOM SLUYTS						
CHK'D	PIETER PEERAER						
APPV'D							
MFG							
Q.A				MATERIAL:		DWG NO. Welding shaft - small sprocket	A4
				WEIGHT:		SCALE: 1:1	SHEET 1 OF 1

Bearing holder

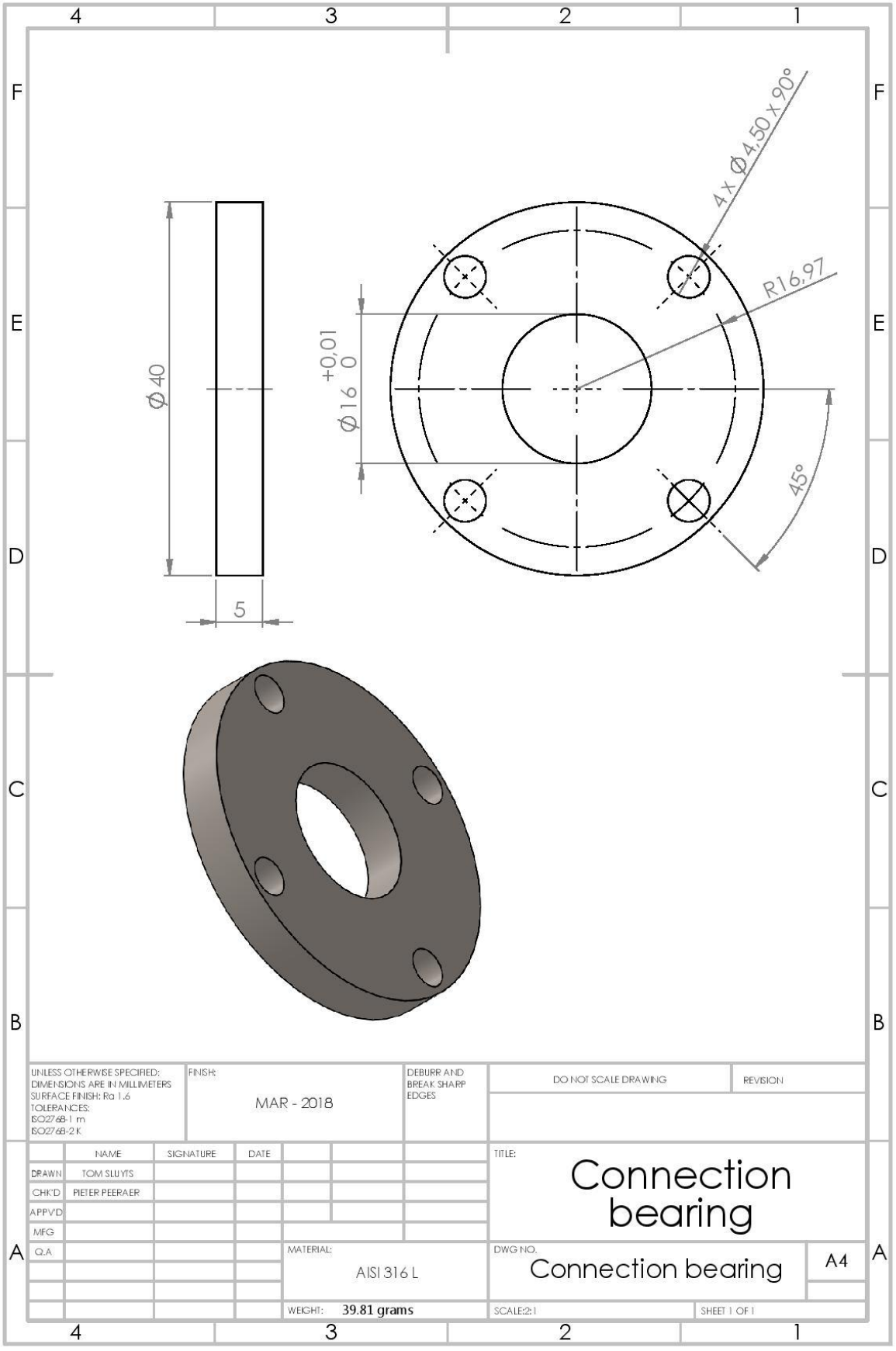

Connection motor

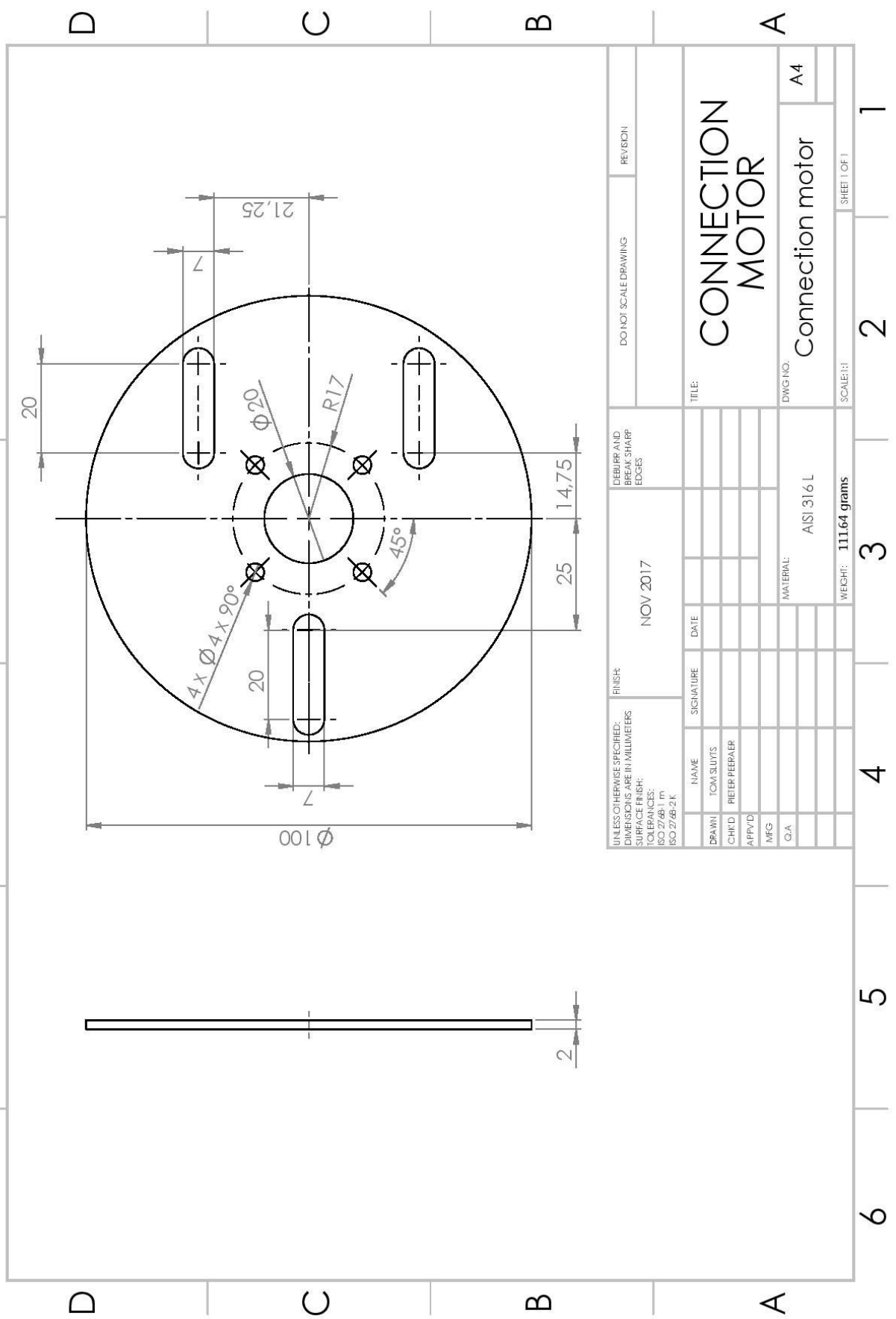

Frontplate small sprocket wheel

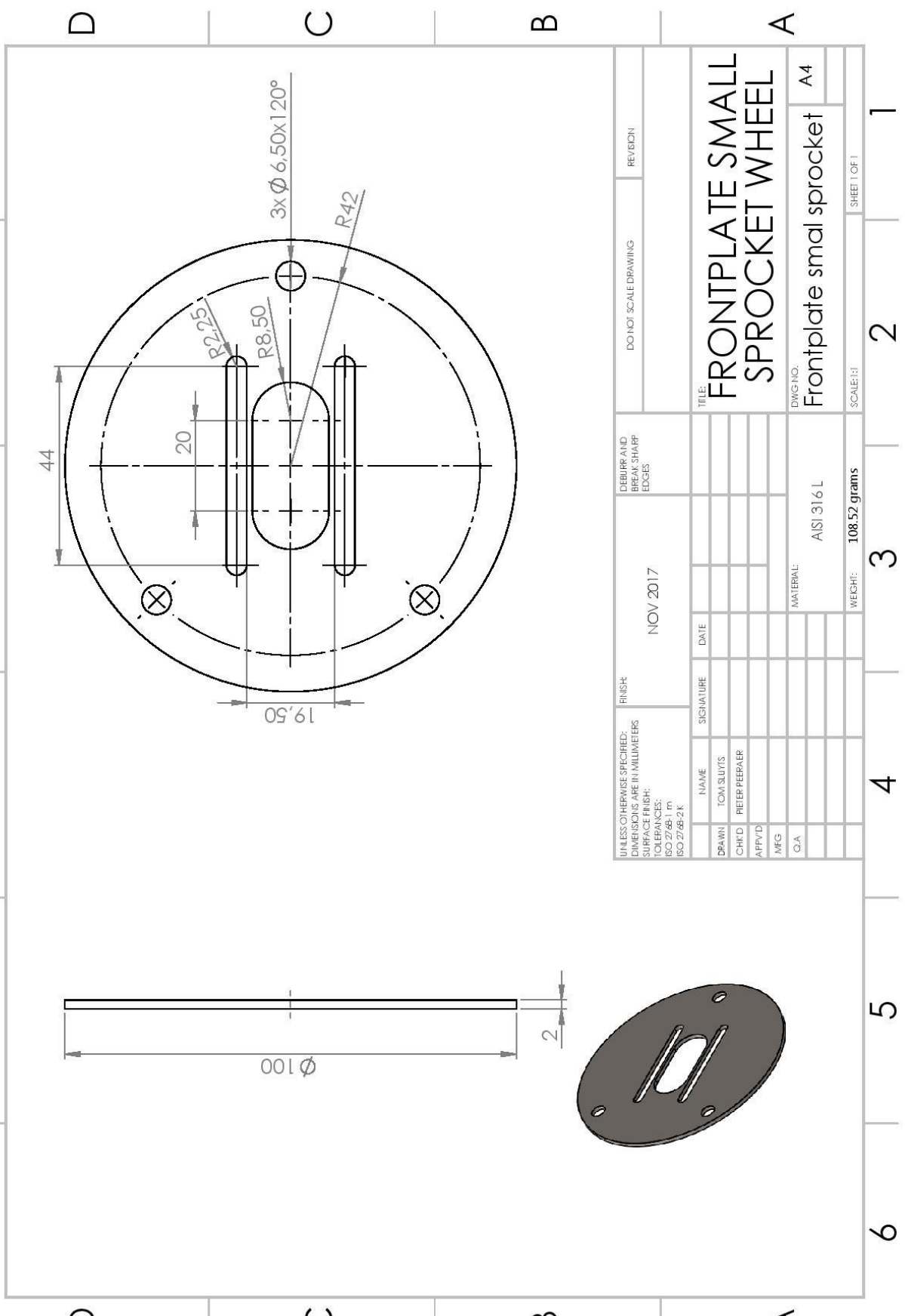

Ring blade

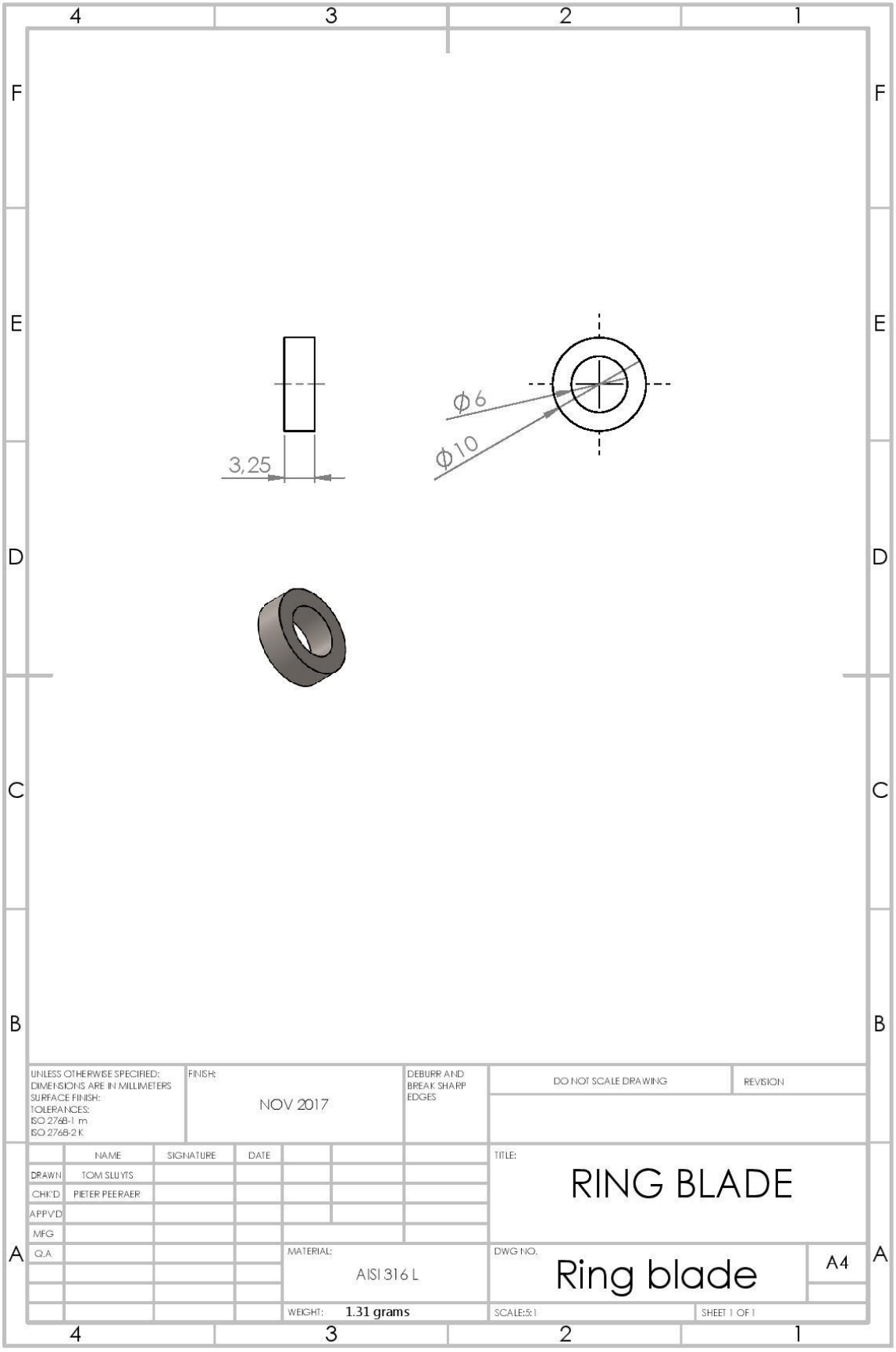
4
3
2
1
F
E
D
C
B
A
3,25
ϕ6
ϕ10
UNLESS OTHERWISE SPECIFIED:
DIMENSIONS ARE IN MILLIMETERS
SURFACE FINISH:
TOLERANCES:
ISO 2768-1 m
ISO 2768-2 K
FINISH:
NOV 2017
DEBURR AND BREAK SHARP EDGES
DO NOT SCALE DRAWING
REVISION
NAME
SIGNATURE
DATE
DRAWN
TOM SLUYTS
CHK'D
PIETER PEERAER
APPV'D
MFG
Q.A
MATERIAL:
AISI 316 L
WEIGHT:
1.31 grams
TITLE:
RING BLADE
DWG NO.
Ring blade
A4
SCALE:5:1
SHEET 1 OF 1

Ring actuator

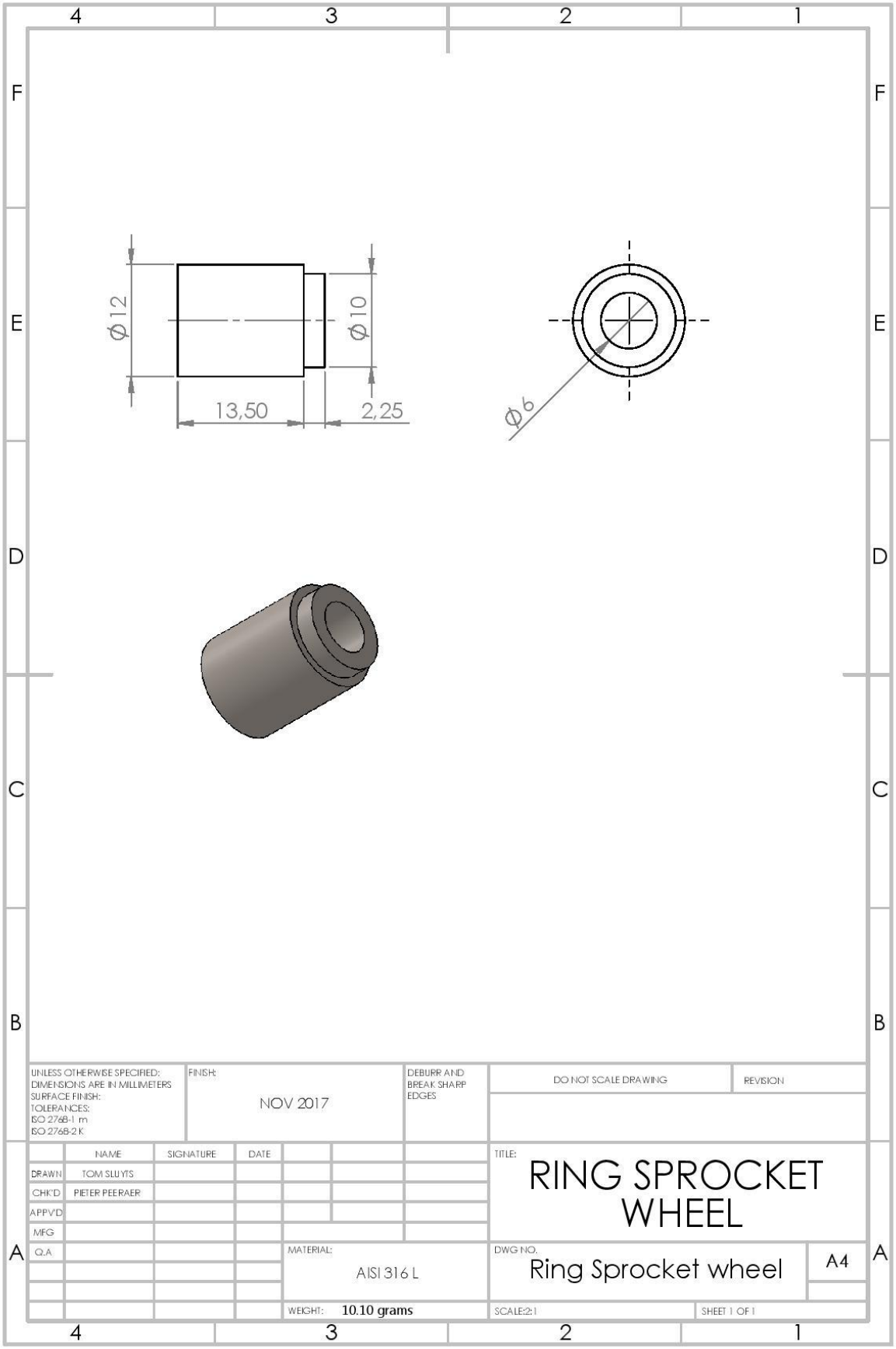

Ring connection motor

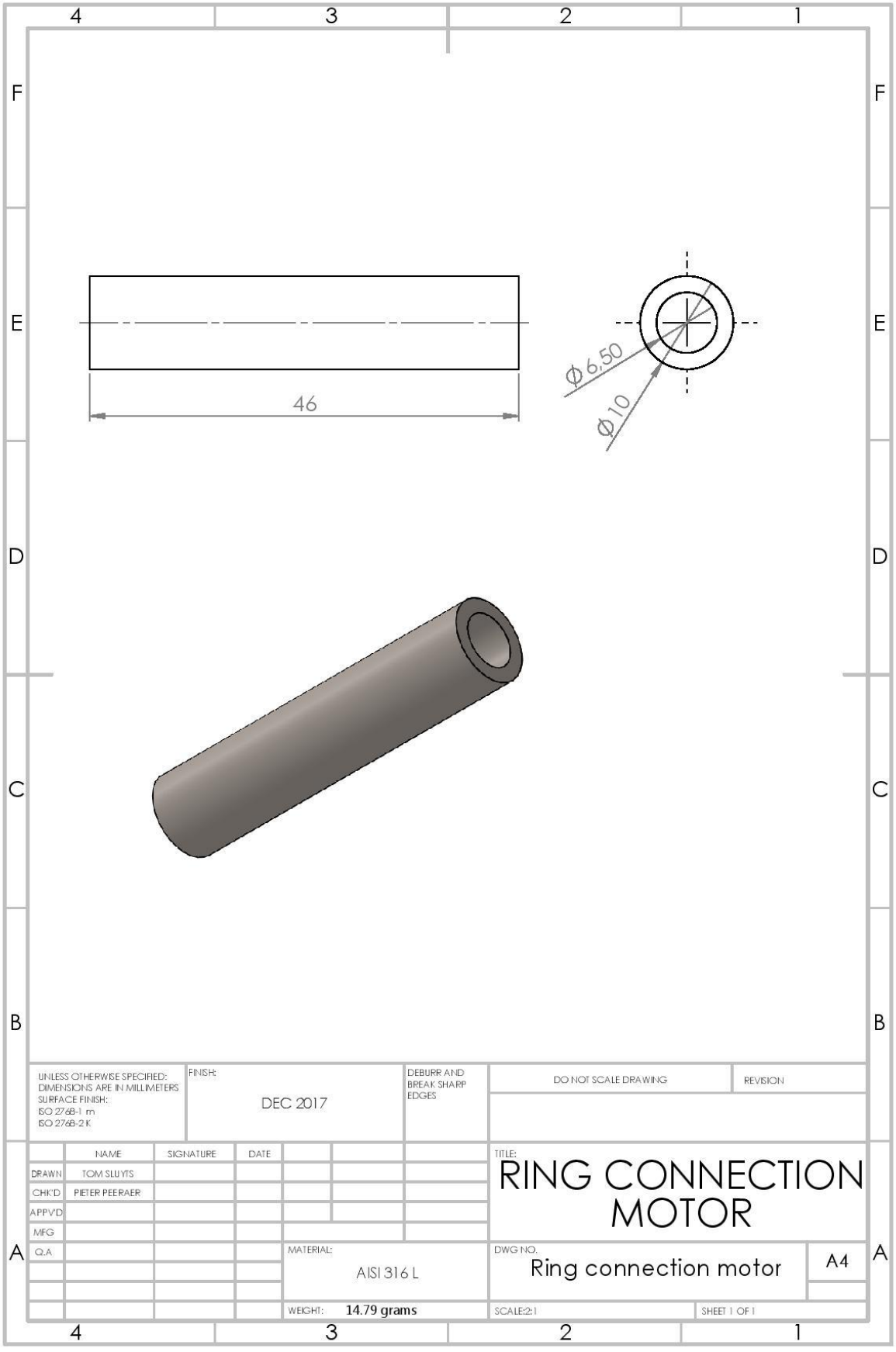

Ring small sprocket wheel

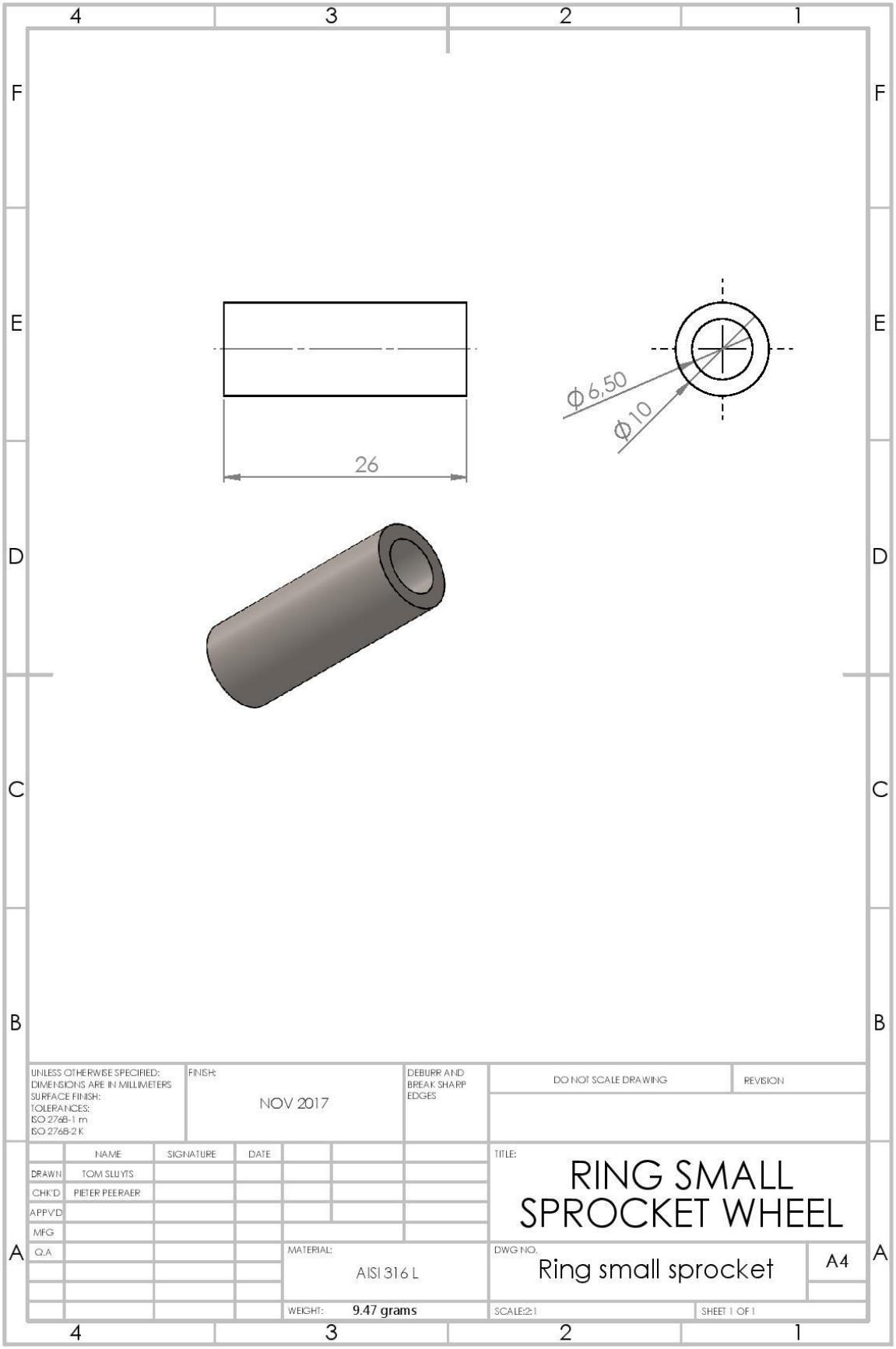

Appendix B BILL OF MATERIAL

PART	VOLUME [mm³]	MASS [g]	QUANTITY	TOTAL MASS [g]
Backplate	167878.78	1347.56	1	1347.56
Ring Blade	163.36	1.31	8	10.48
M6 washer	135.72	0.14	18	2.52
Driving shaft	4933.84	39.6	1	39.6
Ring small sprocket wheel	1179.28	9.47	3	28.41
Frontplate small sprocket wheel	13519.29	108.52	1	108.52
Connection bearing	4959.79	39.81	1	39.81
Hexagonal bolt M4 x 12 mm	265.58	0.27	4	1.08
Washer M4	40.84	0.04	8	0.32
Hexagonal nut M4	106.43	0.11	4	0.44
Deepe grouve ball bearing SKF® 625	629.54	0.63	1	0.63
Coupling	20381.26	20.38	1	20.38
Ring connection motor	4086.41	16.75	3	50.25
Hexagonal bolt M6 x 60 mm	2032.99	2.03	3	6.09
Connection motor	13908.21	111.64	1	111.64
Hexagonal nut M6	331.04	0.33	18	5.94
Ring actuator	1574.16	12.64	4	50.56
Hexagonal bolt M6 x 35mm	1326.13	1.33	3	3.99
Blade	59042.97	473.94	4	1895.76
Needle roller bearing HK0608	270.52	0.27	4	1.08
Actuator	86125.52	691.33	1	691.33
			TOTAL [g]	4416.39

Appendix C 316/316L DATA BULLETIN

AK Steel

316/316L STAINLESS STEEL

PRODUCT DESCRIPTION

Type 316L is an extra-low carbon variation of Type 316 that eliminates harmful carbide precipitation due to welding.

COMPOSITION	TYPE 316 (wt %)	TYPE 316L (wt %)
Carbon	0.08 max.	0.03 max
Manganese	2.00 max.	2.00 max.
Phosphorus	0.045 max.	0.045 max.
Sulfur	0.030 max.	0.03 max.
Silicon	0.75 max.	0.75 max.
Chromium	16.00 – 18.00	16.00 – 18.00
Nickel	10.00 – 14.00	10.00 – 14.00
Molybdenum	2.00 – 3.00	2.00 – 3.00
Nitrogen	0.10 max.	0.10 max.
Iron	Balance	Balance

AVAILABLE FORMS

AK Steel produces Types 316 and 316L Stainless Steels in thicknesses from 0.01 to 0.25 in. (0.25 to 6.35 mm) and widths up to 48 in. (1219 mm). For other thicknesses and widths, inquire.

Values shown in this bulletin were established in U.S. customary units. The metric equivalents of the U.S. customary units shown may be approximate.

MECHANICAL PROPERTIES

TABLE 1 – TYPICAL ROOM TEMPERATURE MECHANICAL PROPERTIES

Condition	UTS ksi. (MPa)	0.2% YS ksi. (MPa)	Elongation % in 2" (50.8 mm)	Rockwell Hardness
Annealed	91 (627)	42 (290)	55	B79

TABLE 2 – ELEVATED TEMPERATURE MECHANICAL PROPERTIES

Temperature °F (°C)	UTS ksi. (MPa)	0.2% YS ksi. (MPa)	Elongation % in 2" (50.8 mm)
400 (204)	81 (558)	35 (241)	51
600 (316)	78 (538)	31 (214)	48
800 (427)	76 (524)	28 (190)	47
1000 (538)	70 (483)	24 (165)	44
1200 (649)	57 (393)	21 (145)	40
1400 (760)	35 (241)	18 (124)	37
1600 (871)	24 (165)	16 (110)	44

TABLE 3 – STRESS RUPTURE PROPERTIES

Test Temperature °F (°C)	Stress, ksi. (MPa), for rupture in:		
	1,000 hours	10,000 hours	100,000 hours
1100 (593)	36.0 (248)	28.0 (193)	25.0 (172)
1200 (649)	24.0 (165)	16.5 (114)	13.5 (94)
1300 (704)	15.5 (106)	10.0 (69)	7.0 (48)
1400 (760)	10.0 (69)	6.0 (41)	3.5 (24)
1500 (816)	6.0 (41)	3.5 (24)	2.0 (14)
1600 (871)	3.5 (24)		

MECHANICAL PROPERTIES

FIGURE 1 – EFFECT OF COLD WORK ON TENSILE PROPERTIES

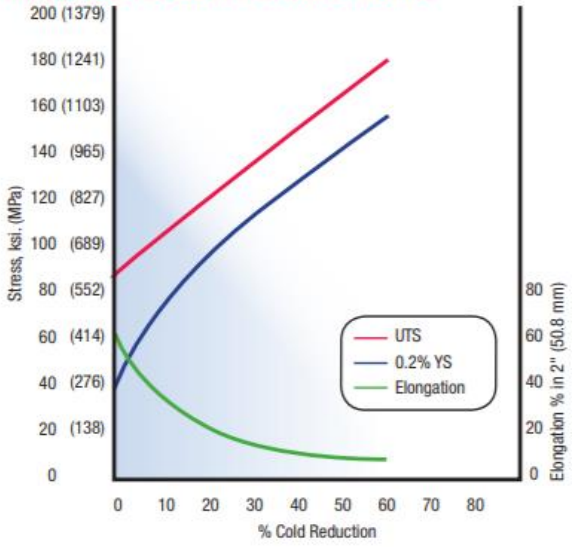

PROPERTIES

PHYSICAL PROPERTIES

Density, lbs./in.^{3} (g/cm^3)	0.29 (7.99)
Electrical Resistivity, μΩ•in. (μΩ•cm) 68 °F (20 °C)	29.4 (74)
Thermal Conductivity, BTU/hr./ft./°F (W/m/K)	
212 °F (100 °C)	9.4 (16.2)
932 °F (500 °C)	12.4 (21.4)
Mean Coefficient of Thermal Expansion, in./in./°F (μm/m/K)	
32 – 212 °F (0 – 100 °C)	8.9 x 10^{-6} (16.0)
32 – 600 °F (0 – 315 °C)	9.0 x 10^{-6} (16.2)
32 – 1000 °F (0 – 538 °C)	9.7 x 10^{-6} (17.5)
32 – 1200 °F (0 – 649 °C)	10.3 x 10^{-6} (18.5)
Modulus of Elasticity, ksi. (MPa)	
in tension	28.0 x 10^3 (193 x 10^3)
in torsion	11.2 x 10^3 (77 x 10^3)
Magnetic Permeability Annealed, (H/m at 200 Oersteds)	1.02 max.
Specific Heat, BTU/lbs./°F (kJ/kg/K) 32 – 212 °F (0 – 100 °C)	0.12 (0.50)
Melting Range, °F (°C)	2500 – 2550 (1371 – 1399)

CORROSION RESISTANCE

Types 316 and 316L stainless steels exhibit improved chloride corrosion resistance when compared to Type 304 due to the molybdenum addition to the steel. This allows for acceptable corrosion protection to marine atmospheres when pitting corrosion is concern. They also provide good chemical resistance to most agents used in the paper, petroleum, food and dairy industries. They are useful in sulfuric acid environments up to 150 °F (60 °C) when concentrations are below 5%. They show excellent corrosion resistance to acetic, formic, phosphoric, and tartaric acids as well as some concentrations and temperatures of bromide and iodide solutions. When welding operations are used, the lower carbon Type 316L allows for reduced risk of intergranular corrosion caused by chromium carbide precipitation.

HEAT TREATMENT

Annealing: Heat to 1900 – 2100 °F (1038 – 1149 °C), then rapidly quench.

COLD WORKING

Due to the higher nickel content, these grades work harden at a lower rate than Type 304. In the annealed condition, they exhibit excellent ductility and may be readily roll formed, deep drawn, and bent. Annealing is essential to restore ductility and to lower hardness for subsequent forming operations. Severely formed parts should be annealed to remove stresses.

FORMABILITY

Types 316 and 316L can be readily formed and drawn using the same methods as used with Type 301 and Type 304. Although the forming capability is very similar to Type 301, temperature variation will have less influence on material behavior. This product may become slightly magnetic when highly cold worked.

WELDABILITY

The austenitic class of stainless steels is generally considered to be weldable by the common fusion and resistance techniques. Special consideration is required to avoid weld "hot cracking" by assuring formation of ferrite in the weld deposit. These particular alloys are generally considered to have poorer weldability than Types 304 and 304L. A major difference is the higher nickel content for these alloys which requires slower arc welding speed and more care to avoid hot cracking. When a weld filler is needed, AWS E/ER 316L and 16-8-2 are most often specified. Type 316 and its low-carbon "L" version are well known in reference literature and more information can be obtained in the following references:

1. ANSI/AWS A5.9, A5.22 and A5.4 (Stainless Steel Welding Electrode Specifications).
2. "Welding of Stainless Steels and Other Joining Methods," SSINA, (www.ssina.com).
3. ANSI/AWS B2.1.009:2002 (GTAW 300's @ 0.50 – 0.14 in.).
4. ANSI/AWS B2.1-8-024:2001 (GTAW 300's @ 0.0625 – 1.5 in.).
5. ANSI/AWS B2.1-8-013:2002 (SMAW 300's @ 0.050 – 0.14 in.).
6. ANSI/AWS B2.1-8-023:94 (SMAW 300's @ 0.125 – 1.5 in.).
7. ANSI/AWS B2.1.005:2002 (GMAW 300's @ 0.050 – 0.14 in.).
8. ANSI/AWS D1.6/D1.6M:2007 (Structural Welding Code – Stainless Steel).

SPECIFICATIONS

Types 316 and 316L Stainless Steel sheet and strip are covered by the following specifications:

Type 316	Type 316L
AMS 5524 ASTM A240	AMS 5507 ASTM A240

Appendix D THERMOCOUPLES WATLOW - 70XKSGC048A

General Applications Tube and Wire

Ring Terminal
Style 70

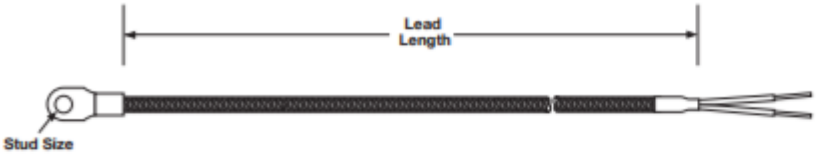

The nickel terminal can be placed beneath existing screws or bolts to permit surface temperature measurement.

Note: Grounded junction shown.

Ordering Information

Part Number

① ② Const. Style	③ Diameter	④ Calibration	⑤ Lead Protection	⑥ Junction	⑦ Stud Size Hole Diameter	⑧ ⑨ ⑩ Lead Length	⑪ Term./ Options
70	X						

① ②	Construction Style
70 =	Ring terminal thermocouple

③	Diameter
X =	Not applicable

④	Calibration
J =	Type J
K =	Type K
T =	Type T
E =	Type E

⑤	Lead Protection
F =	Fiberglass (24 gauge stranded)
S =	Fiberglass with stainless steel overbraid (24 gauge stranded)
P =	Fiberglass (20 gauge stranded)
B =	Fiberglass with stainless steel overbraid (20 gauge stranded)
T =	PFA (24 gauge stranded)
U =	PFA with stainless steel overbraid (24 gauge stranded)
V =	PFA (20 gauge stranded)
W =	PFA with stainless steel overbraid (20 gauge stranded)

⑥	Junction
G =	Grounded
U* =	Ungrounded
*Only available with 24 gauge wire.	

⑦	Stud Size - Hole Diameter (in.)
A* =	No. 6
B* =	No. 8
C* =	No. 10
D =	1/4
E =	3/8
*Only available with 24 gauge wire.	

⑧ ⑨ ⑩	Lead Length (in.)
Available lengths: 006 to 360 in., over 360 in. contact factory	

⑪	Termination/Options
A =	Standard, 2 1/2 in. split leads
B =	2 1/2 in. split leads with #6 spade lugs
C =	2 1/2 in. split leads with #6 spade lugs and BX connector
D =	Standard male plug, quick disconnect
E =	Standard female jack, quick disconnect
F =	Miniature male plug, quick disconnect
G =	Miniature female jack, quick disconnect
H =	1/4 in. push-on connector

Appendix E **ARM46AK-T10 DATASHEET**

Orientalmotor

ORIENTAL MOTOR U.S.A. Corp.
570 Alaska Avenue
Torrance, CA 90503
1-800-GO-VEXTA (468-3982)

Item # ARM46AK-T10, 1.65 in. (42 mm) Closed Loop Stepper Motor

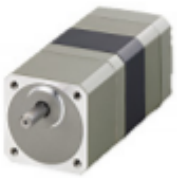

The AR Series adopts our AlphaStep technology closed loop control so the motor does not lose synchronism even when subjected to abrupt load fluctuation or acceleration. Requires AR Series (DC Input) Driver.

- Driver sold separately
- Designed for continuous operation
- Lower heat generation
- Low vibration
- High response
- No hunting
- No gain tuning

Web Price

$256.00

*Connection Cables required (sold separately)

CE

Specifications | General Specifications | Dimensions | Speed-Torque | Connection | System

Specifications

Product Line	Oriental Motor ®
Motor Type	Closed Loop
Frame Size	1.65 in
Motor Length	3.9 in.
Driver Voltage Input Power	DC
Speed-Torque Characteristics	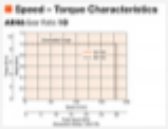 Speed - Torque Characteristics
Holding Torque	141 oz-in
Shaft/Gear Type	Taper Hobbed Gear
Gear Ratio (X:1)	10 :1
Backlash	25 arc min (0.417°)

Shaft	Single
Electromagnetic Brake	Not Equipped
Resolution (Resolution Setting: 1000 P/R)	0.036 °/Pulse
Permissible Speed Range (r/min)	0 ~ 180
Rotor Inertia	0.32 oz-in²
RoHS Compliant	These products do not contain substances that exceed the regulation values in the RoHS Directive.
Safety Standards	CE
CE Marking	EMC Directives
Permissible Overhung Load	0 in. from Shaft End = 2.2 lb 0.2 in. from Shaft End = 3.1 lb 0.39 in. from Shaft End = 4.5 lb 0.59 in. from Shaft End = 6.7 lb
Permissible Thrust Load	3.3 lb

General Specifications

Insulation Class	Class B [130°C (266°F)]
Insulation Resistance	100 MΩ or more when 500 VDC megger is applied between the following places: Case - Motor and sensor windings
Dielectric Strength	Sufficient to withstand the following for 1 minute: Case - Motor and sensor windings 1.0 kVAC 50 Hz or 60 Hz
Ambient Temperature	-10 ~ 50°C (14 ~ 122°F) (non-freezing) (when a heat sink of a capacity at least equivalent to an aluminum plate with a size of 3.94 x 3.94 in., 0.24 in. thick is installed.)
Ambient Humidity	85% or less (non-condensing)
Operating Atmosphere	No corrosive gases, dust water or oil
Degree of Protection	IP65 (excluding the mounting surface and connector)
Stop Position Accuracy	±4 arc minutes (±0.067°)
Shaft Runout	0.05 mm (0.002 in.) T.I.R.
Concentricity	0.075 mm (0.003 in.) T.I.R.
Perpendicularity	0.075 mm (0.003 in.) T.I.R.

Dimensions

Dimensions Unit = mm (inch)

● Motor

◇ **TH** Geared Type

☐ 42 mm (☐ 1.65 in.)

Model	Motor Model	Gear Ratio	Mass kg (lb.)
AR46AK-TH-3	ARM46AK-TH	**3.6, 7.2, 10, 20, 30**	0.62 (1.36)

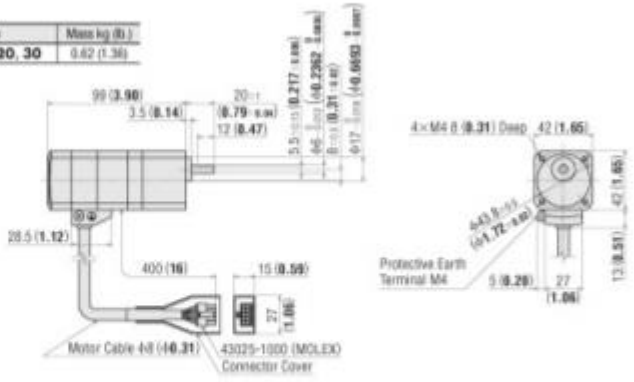

Appendix F CMOS-CAMERA: BC-X104FG-1211

mvBlueCOUGAR-X / -POE-I

Technical Details

Sensors

mvBlueCOUGAR-X		POE-I	Resolution (H x V pixels)	Sensor size (optical)	Pixel size (µm)	Frame rate	Model	Readout type	ADC resolution / output in bits	Sensor
-120a	G/C		640 x 480	1/3"	7.4 x 7.4	105	CCD	Global	14 → 14/12/8	Sony ICX424
-120b[3]	G/C		640 x 480	1/2"	9.9 x 9.9	105	CCD	Global	14 → 14/12/8	Sony ICX414
-100w[1]	G/C		752 x 480	1/3"	6 x 6	117	CMOS	Global	10 → 12/10/8	Aptina MT9V
-100f	G/C		728 x 544	1/2.9"	6.9 x 6.9	299.8	CMOS	Global	12 → 16/12/8	Sony IMX287
-120d	G/C	✓	776 x 580	1/2"	8.3 x 8.3	87	CCD	Global	14 → 14/12/8	Sony ICX415
-122[3]	G/C	✓	1280 x 960	1/3"	3.75 x 3.75	31	CCD	Global	14 → 14/12/8	Sony ICX445
-102b	G/C	✓	1280 x 960	1/3"	3.75 x 3.75	45.7	CMOS	Global	10 → 12/10/8	Aptina MT9M
-102e[2,3]	G/C	✓	1280 x 1024	1/1.8"	5.3 x 5.3	60.9	CMOS	Global	10 → 10/8	E2V EV76C560
-123	G/C	✓	1360 x 1024	1/2"	4.65 x 4.65	30	CCD	Global	14 → 14/12/8	Sony ICX267
-102f	G/C		1456 x 1088	1/2.9"	3.45 x 3.45	75	CMOS	Global	12 → 16/12/8	Sony IMX273
-104	G/C	✓	2048 x 1088	2/3"	5.5 x 5.5	34.8	CMOS	Global	10 → 10/8	CMOSIS CMV2000
-104b	G/C		2048 x 2048	1"	5.5 x 5.5	18.5	CMOS	Global	10 → 10/8	CMOSIS CMV4000
-104bUV	G		2048 x 2048	1"	5.5 x 5.5	18.5	CMOS	Global	10 → 10/8	CMOSIS CMV4000
-104e[3]	G/C	✓	1600 x 1200	1/1.8"	4.5 x 4.5	52.2	CMOS	Global	10 → 10/8	E2V EV76C570
-104f	G/C	✓	1936 x 1216	1/1.2"	5.86 x 5.86	46.9	CMOS	Global	12 → 16/12/8	Sony IMX249
-104i[4]	G/C	✓	2064 x 1544	1/1.8"	3.45 x 3.45	37	CMOS	Global	12 → 16/12/8	Sony IMX265
-124[3]	G/C		1600 x 1200	1/1.8"	4.4 x 4.4	28	CCD	Global	14 → 14/12/8	Sony ICX274
-125a[3]	G/C	✓	2448 x 2050	2/3"	3.45 x 3.45	10	CCD	Global	14 → 14/12/8	Sony ICX655
-225[3]	G/C	✓	2448 x 2050	2/3"	3.45 x 3.45	16	CCD	Global	14 → 14/12/8	Sony ICX625
-105	G/C	✓	2592 x 1944	1/2.5"	2.2 x 2.2	14.4	CMOS	Global Reset	12 → 12/10/8	Aptina MT9P
-105b[4]	G/C	✓	2464 x 2056	2/3"	3.45 x 3.45	23.5	CMOS	Global	12 → 16/12/8	Sony IMX264
-109b[4]	G/C	✓	4112 x 2176	1"	3.45 x 3.45	13.2	CMOS	Global	12 → 16/12/8	Sony IMX267
-1010	G/C		3856 x 2764	1/2.3"	1.67 x 1.67	8.7	CMOS	Global Reset	12 → 12/10/8	Aptina MT9J
-1012b[4]	G/C	✓	4112 x 3008	1.1"	3.45 x 3.45	9.6	CMOS	Global	12 → 16/12/8	Sony IMX304

[1] High Dynamic Range (HDR) mode supported
[2] Infrared enhanced model - 102eGE also available
[3] Extended temperature range from -40°C up to max. 65°C
[4] Announcement

Hardware Features

Protocol		Compliant to GigE Vision
Interface		Gigabit Ethernet (1000 Mbit/s with 100 Mbit/s compatibility)
Image formats		Mono8, Mono12, Mono14, Mono16, Mono12Packed BayerGR8, BayerGR10, BayerGR12, BayerGR16, BayerGR12Packed (GR, RG, GB, BG depends on camera type) RGB8Packed, BGR8Packed, BGRA8Packed, BGR10V2Packed, YUV422Packed, YUV422_YUYVPacked, YUV444Packed
Triggers		External, software based or free run
Size of body (W x H x L) | Weight w/o lens	Standard POE-I	39.8 x 39.8 x Y + 5 mm | approx. 110 g 39.8 x 39.8 x Y + 5 mm | approx. 127 g
Permissible ambient temperature	Operation Storage	0 .. 45 °C (-40 .. 65 °C as an option) / 30 to 80 % RH -20 .. 60 °C / 20 to 90 % RH
Lens mounts		Back focus adjustable C/CS-mount lens holder / C-mount, CS-mount or optional S-mount
Digital I/Os	Standard POE POE-I	2 opto-isolated inputs / 4 high-side outputs 2 opto-isolated inputs / 2 opto-isolated outputs 4 opto-isolated inputs / 4 high-side outputs
Connectors	POE-I	2x M12 industrial connectors: I/O and power supply | Gigabit Ethernet connector (x-coded)
Conformity		CE, FCC, RoHS, IP40, IP67
Driver		mvIMPACT Acquire SDK or any GigE Vision compliant interface
Operating systems		Windows®, Linux® - 32 bit and 64 bit
Special features		Frame average, enhanced color and I/O functionality, PoE, automatic gain / exposure control, binning, PLC inputs, pre-trigger recording, internal temperature sensors, FFC, screw lock connectors, video iris

mvBlueCOUGAR-X / -POE-I

Technical Details

GiGE VISION

GEN<i>CAM

Dimensions Standard Version (in mm)

front view	side view	back view
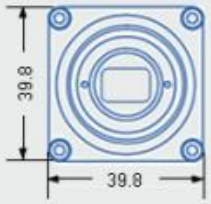	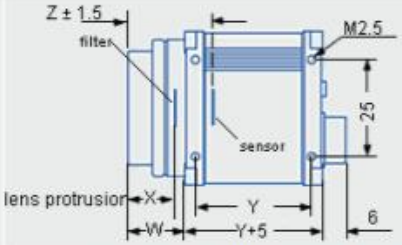	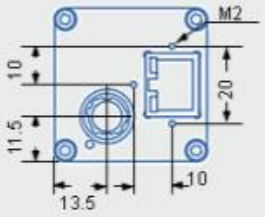

W = approx. 15 | 10 Y = 32 (CMOSIS), 30
X = 6 .. 8 Z = 12.5 | 17.526

Dimensions POE-I Version (in mm)

front view	side view	back view
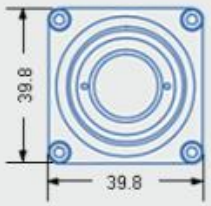	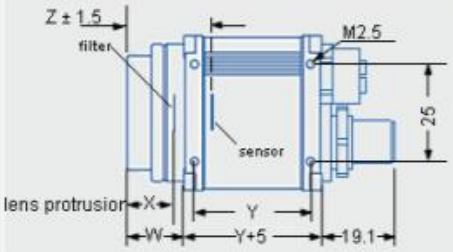	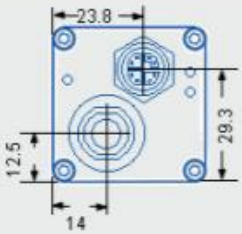

W = approx. 15 | 10 Y = 5 .. 11
X = 6 .. 8 Z = 12.5 | 17.526

Protection class IP67 (POE-IP67, POE-IP67AL)

Based on the industrial connector concept we offer a IP67 stainless steel or black anodized aluminium housing.

Appendix G FLOW METER: DIGIFLOW 6710M-32TM

Savant DigiFlow 6710M-32TM, Mini Flow Totalizer and Flow Rate Meter

Features :

- □ Flow totalizing up to 99999 liters
- □ Flow rate display from 0.2 to 5 liter/min.
- □ Low battery power alert
- □ Automatic data memorized

Application :

- ✓ Water cooler
- ✓ Water dispenser
- ✓ Cooling system for machinery

1.0 Electrical :

Operating Voltage : 3 DC Volts

Operating Current : 3.5 mA (work), 0.015 mA (sleep)

2.0 Mechanic :

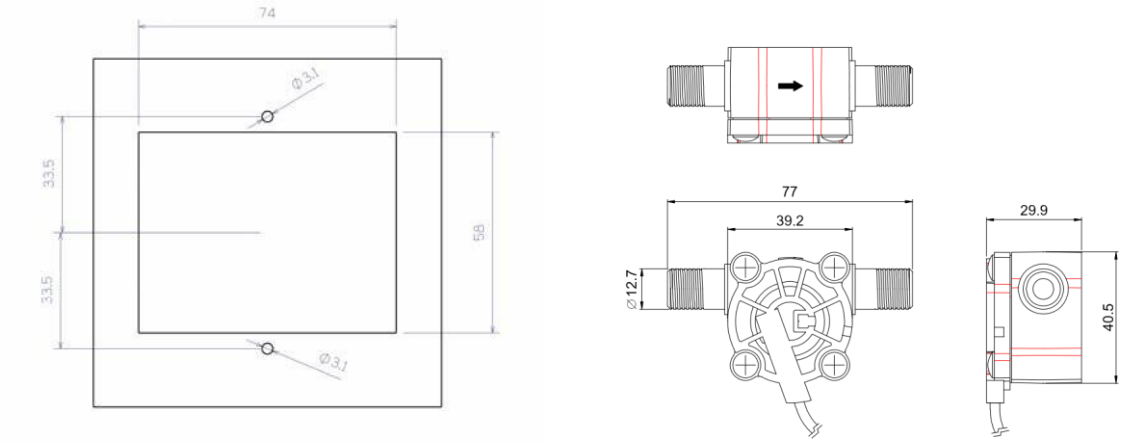

3.0 Application :

Installation Method : **Horizontal installation ONLY**

Flow Direction : One way

Flow Rate : 0.2 – 5 liter/min

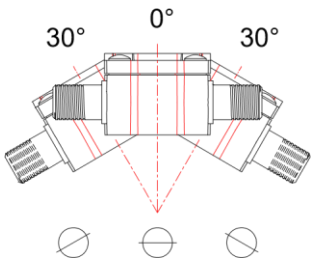

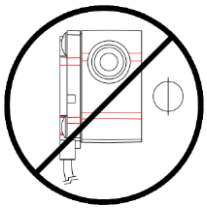

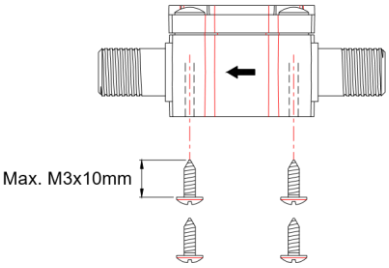

4.0 General :

Temperature : 0 to 80℃ (32 to 170 ℉)

Pressure : Max. 8 bar (113 psi)

Weight : 140 g (5.38 oz)

Accuracy : +/- 5 %

Connection : 1/4” BSP male

Materials : Sensor Body : PA66 with 50% glass fiber, Grivory GV-5H

Paddle : Acetal Copolymer, TICONA M90

Stick of Turbine : #304 Stainless Steel

O-Ring : EPDM Rubber

Housing : ABS resin

Appendix H THERMOCOUPLE: OMEGA M12KIN-1/8-U-6-D

Standard Sizes

M12 Series

RoHS

- Type J and K Thermocouple Calibrations
- Single and Dual Element Configurations
- Ungrounded Junctions
- -50 to 85°C (-58 to 185°F) Connector Temperature Range
- 304 Stainless Steel Probe (Type J) and Inconel 600 Probe (Type K)
- Available in⅛ or ¼"
- Many Standard Lengths Available
- Stainless Steel Transition with M12 Connector
- Vibration Tested at 3g's Between 5 and 500 Hz for 3 Hours in the Axial and Transverse Axes (6" Long or Shorter)

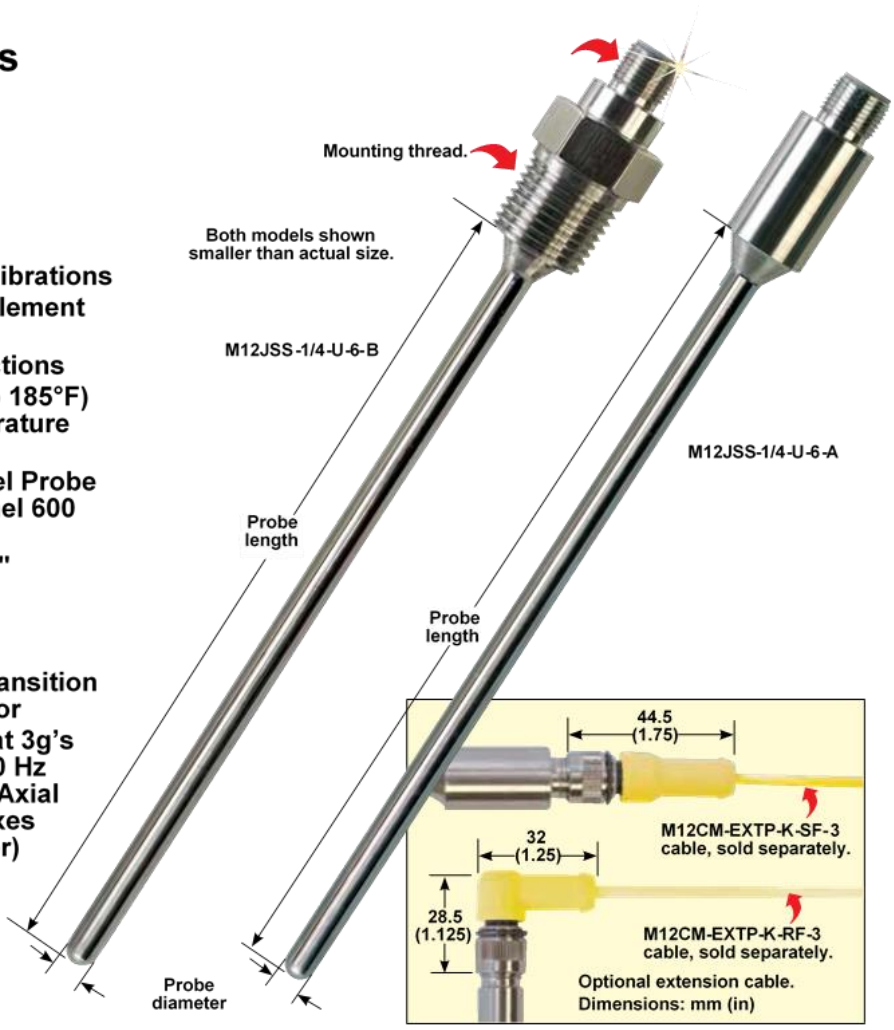

To Order

Model Number	Probe Length	Thermocouple Calibration	Sheath Material	Mounting Thread
M12JSS-(*)-U-6-A	6"	J	304 SST	None
M12JSS-(*)-U-6-B	6"	J	304 SST	½ NPT
M12JSS-(*)-U-6-C	6"	J	304 SST	⅜ NPT
M12JSS-(*)-U-6-D	6"	J	304 SST	¼ NPT
M12KIN-(*)-U-6-A	6"	K	Inconel 600	None
M12KIN-(*)-U-6-B	6"	K	Inconel 600	½ NPT
M12KIN-(*)-U-6-C	6"	K	Inconel 600	⅜ NPT
M12KIN-(*)-U-6-D	6"	K	Inconel 600	¼ NPT

FACULTEIT INDUSTRIËLE INGENIEURSWETENSCHAPPEN
CAMPUS DE NAYER SINT-KATELIJNE-WAVER
J. De Nayerlaan 5
2860 SINT-KATELIJNE-WAVER, België
tel. + 32 15 31 69 44
iiw.denayer@kuleuven.be
www.iiw.kuleuven.be